671 | November 2013

SCHRIFTENREIHE SCHIFFBAU

Christian Ulrich

Smoothed-Particle-Hydrodynamics Simulation of Port Hydrodynamic Problems

TUHH
Technische Universität Hamburg-Harburg

Smoothed-Particle-Hydrodynamics Simulation of Port Hydrodynamic Problems

Vom Promotionsausschuss der
Technischen Universität Hamburg-Harburg
zur Erlangung des akademischen Grades

Doktor-Ingenieur (Dr.-Ing.)

genehmigte Dissertation

von

Christian Ulrich

aus Recklinghausen

2013

Vorsitzender des Prüfungsausschusses
Prof. Dr.-Ing. Alexander Düster

Gutachter
1. Gutachter: Prof. Dr.-Ing. Thomas Rung
2. Gutachter: Prof. Ing. Stefano Sibilla

Zusätzliche Gutachter
Prof. Dr.-Ing. Alexander Düster
Prof. Dr.-Ing. Stefan Heinrich

Tag der mündlichen Prüfung
26. September 2013

Technischen Universität Hamburg-Harburg
Schwarzenbergstraße 95c
D-21073 Hamburg
http://www.tuhh.de/vss

Bericht Nr. 671
ISBN 978-3-89220-671-2

Abstract

The thesis reports on the development of a numerical procedure based on the Lagrangian Smoothed-Particle-Hydrodynamics (SPH) method for the simulation of hydrodynamic problems in harbours. The target applications focus on ship induced scouring of the harbour bottom. Respective erosions represent unpleasant phenomena, especially if they occur close to quay walls. They can significantly weaken the structural support and cause cost intensive counter measures. These measures are usually based on a rather weak background knowledge, thus simulations might help to analyse the erosional processes without the need for model- or full-scale experiments. Contrary to common state-of-the-art simulation tools, the present work pursues a monolithic approach to capture the complex overall problem. This requires an SPH procedure that is able to cope with water/soil interaction, floating self-propelled ships as well as large computational domains. Within the present SPH-framework, water is modelled as a Newtonian fluid and the soil is treated by a combined solid/fluid-approach based on the Mohr-Coulomb yield criterion. The technique captures small deformations of the soil by an elastic model whereas a transition to a rate dependent non-Newtonian fluid behaviour is initiated for higher strain rates. The interaction between water and soil is realised by a three-layer suspension model which is needed for an accurate prediction of erosional phenomena. Partly saturated porous media can also play an important role in soil failure processes. They are taken into account by a saturation dependent variable cohesion with the seepage flow through the soil skeleton being evaluated from a simple Darcy approach. A body-force propulsor model based on open water characteristics is used to represent ship propellers and thrusters. Vessel motions are captured by a 6DOF motion solver. To enhance the code's applicability to large domains, a variable particle resolution strategy based on changeable particle masses is applied. This allows for a fine resolution of local details whereas the far field can be modelled by a coarse particle distribution in order to reduce the overall number of particles.

Gegenstand der vorliegenden Dissertation ist die Entwicklung eines numerischen Verfahrens auf Basis der Lagrangen Smoothed-Particle-Hydrodynamics (SPH) Methode zur Simulation hydrodynamischer Problemstellungen in Häfen. Im Anwendungsfokus liegen schiffsinduzierte Erosionen der Hafensohle. Insbesondere die auf Propeller- und Querstrahlruderwirkung zurückzuführende Kolkbildung nahe der Kaimauer kann eine erhebliche Schwächung der Bauwerksstruktur hervorrufen und führt zu kostenintensiven Gegenmaßnahmen. Der Kolkbildungsprozess ist nicht hinlänglich erforscht. Simulationen können dazu beitragen, die beteiligten Erosionsmechanismen besser zu verstehen, ohne auf Modell- bzw. Naturversuche angewiesen zu sein. Im Gegensatz zu derzeit verbreiteten Simulationswerkzeugen wird in dieser Arbeit ein monolithischer Ansatz zur Abbildung der Wasser/Boden-Wechselwirkung verfolgt. Hierzu wird ein SPH Verfahren benötigt, das in der Lage ist, Wasser/Boden-Interaktion und schwimmende, selbstangetriebene Schiffe abzubilden sowie große Rechengebiete zu verarbeiten. Im vorliegenden SPH-Löser wird Wasser als Newtonsches Fluid modelliert. Für den Boden wird ein kombinierter Festkörper/Fluid-Ansatz auf Basis des Mohr-Coulomb Fließkriteriums verwendet, das kleine Verformungen über ein elastisches Modell abbildet. Ein scherratenabhängiger Übergang zu einem nicht-Newtonschen Fluid wird für große Verformungen eingeführt. Die Interaktion zwischen Wasser und Boden wird durch ein dreischichtiges Suspensionsmodell realisiert, das maßgeblich zu einer genauen Vorhersage der Erosionswirkung beiträgt. Weitere Versagensmechanismen von Böden sind häufig auf teilgesättigte poröse Medien zurückzuführen. Sie werden über eine veränderliche effektive Kohäsion berücksichtigt wobei Sickerströmungen des Porenwassers über einen einfachen Darcy Ansatz abgebildet werden. Ein auf Freifahrtkurven basierendes Volumenkraftmodell repräsentiert die Wirkung von Schiffspropellern und -querstrahlern. Schiffsbewegungen werden über einen 6DOF Bewegungslöser berechnet. Um die Anwendbarkeit des Verfahrens für große Rechengebiete zu verbessern werden variable Partikelauflösungen auf Basis veränderlicher Partikelmassen verwendet. Bereiche von besonderem Interesse können dabei fein aufgelöst werden, wohingegen das Fernfeld mit groben Partikelverteilungen abgebildet werden kann um eine Reduzierung der Gesamtpartikelzahl zu erreichen.

Acknowledgments

I would like to thank the German Research Foundation (Deutsche Forschungsgemeinschaft, DFG) for supporting the project. The present work forms part of the Research Training Group Ports for Container Ships of Future Generations: Interaction of Ship, Fluid, Structure and Soil (GRK 1096) at the Hamburg University of Technology.

I would like to express my gratitude to my supervisor Prof. Dr.-Ing. Thomas Rung for his support, encouragement and many fruitful ideas and discussions throughout all stages of this research. Additional thanks go to Prof. Ing. Stefano Sibilla and Prof. Dr.-Ing. Alexander Düster for their work related to the examination process.

Special thanks are directed to my colleagues from the Institute for Fluid Dynamics and Ship Theory as well as the DFG Research Training Group. It was a pleasure and a valuable experience working in both inspiring teams.

Furthermore, the helpful contributions within student research projects of Nils Koliha, Claus Stigler, Sven Bednarek, and Torben Mühlbach related to various parts of this thesis are highly appreciated.

Finally, I thank my parents and Inken for their continuous support.

Contents

List of Figures

List of Tables

x

Nomenclature

The following list of symbols is not exhaustive. Any other notation introduced will be defined when required. Vectors and tensors are defined by reference to cartesian coordinates. Greek superscripts are used to mark cartesian tensor coordinates. Einstein's summation is employed over repeated Greek superscripts. In symbolic notation, the degree of tensorial symbols corresponds to the amount of underlines. Time derivatives are marked by a dot, e.g. $\dot{f}$.

Latin

A_{ac}	integration constant, Couette test-case
a^{α}	particle acceleration vector
a	water column base length, Martin and Moyce test-case
A_t	cross-sectional area of transverse thruster
b^{α}	body force vector
b_{sx}	axial propeller induced body force on single ship hull particles
b_{sy}	thruster induced body force on single ship hull particles
b_x	axial propeller induced body force on single fluid particles
b_y	thruster induced body force on single fluid particles
b_{ϕ}	tangential propeller induced body force on single fluid particles
B	reference pressure in Tait's equation
B_{ac}	integration constant, Couette test-case
B_W	width of wedge
B_S	ship's breadth
B_Q	ship's distance to quay wall
c	sound speed

c_d	damping coefficient
c_{T1}, c_{T2}	propeller parameters related to open water characteristics
c_{Q1}, c_{Q2}	propeller parameters related to open water characteristics
$\tilde{c}_{\mathbf{s}}$	volumetric soil concentration
C	cohesion
C'	maximum cohesion
C_{dry}	cohesion, dry soil
C_f	Chézy friction coefficient
C_{sat}	cohesion, completely saturated soil
C_S	Smagorinsky constant
Co	Courant number
CP	pressure coefficient
d	diffusion coefficient
D	damping term
D_p	propeller diameter
D_T	thruster diameter
E	Young's modulus
$f()$	arbitrary function
f^{α}	volumetric force vector
f_{bd}	boundary force
f^{α}_{FB}	vector of the integral force acting on floating bodies
g	gravity
h	smoothing length
h_w	height of water column for hydrostatic pressure initialization
h_s	height of soil below water column for hydrostatic pressure initialization
h	smoothing length
H	reference fluid column height
H	nomalised height, Martin and Moyce test-case
H_s	height of soil column
H_w	height of water column
J	propeller advance coefficient
J_2	second invariant

$\mathcal{J}$	Jaumann stress rate
K	permeability
K_T	propeller thrust coefficient
K_Q	propeller torque coefficient
L_B	bottom length of embankment
L_s	length of soil column
L_S	length of ship
L_T	top length of embankment
L_w	length of water column
m	mass
M	Mach number
$n_{_{FB}}$	floating body's rotation axis
n_p	propeller rotation rate
N	number of particles
N_{FB}	number of floating body particles
N_{pp}	number of particles inside the propeller actuator disc
N_{sp}	number of ship hull particles
N_{st}	number of ship hull particles in the vicinity of transverse thrusters
p	pressure
P	power of transverse thruster
Q_p	propeller torque
r	particle distance
r'	relative radial coordinate in propeller actuator disc
r_D	radial coordinate in propeller actuator disc
r_h	radius of propeller hub
r_n	normalised radius, Couette test-case
r_p	propeller radius
R	relative particle distance
R_1	radius of inner cylinder, Couette test-case
R_2	radius of outer cylinder, Couette test-case
R_{ac}	radial coordinate, Couette test-case
R_g	gas constant

R_{vm}	scaling ratio derived from von Mises criterion
Re	Reynolds number
s_m	source term in continuity equation
s_v	variable resolution source term in momentum equation
s_ρ	variable resolution source term in continuity equation
S	surface fraction
S^*	strain rate invariant
S_u^*	upper strain rate limit, combined fluid/solid soil model
t	time
t_{FB}^α	vector of the integral torque acting on floating bodies
T	temperature
T	normalised time, Martin and Moyce test-case
T_p	propeller thrust
T_S	draft of ship
T_t	transverse thruster thrust
Ta	Taylor number
v	velocity
v_a	propeller advance velocity
v_{max}	maximum flow velocity
v_{sig}	signal velocity
v_t	thruster jet velocity
v_W	wedge velocity, wedge impact test-case
v_φ	radial velocity, Couette test-case
V	volume
W	smoothing kernel function
W^*	corrected smoothing kernel function
x^α	position vector
x_{FB}^α	centre of gravity of floating bodies
$\hat{x}_i^\alpha$	particle location relative to floating body's centre of gravity
z	position of surge, Martin and Moyce test-case
Z	normalised position of surge, Martin and Moyce test-case

Greek

α_{cap}	exponent controlling the strength of capillary potential
α_d	dimension depending normalisation parameter of kernel function
$\tilde{\alpha}_{hd}$	dimension depending normalisation parameter, kernel derivatives by r
$\tilde{\alpha}_{rd}$	dimension depending normalisation parameter, kernel derivatives by h
α_w	kernel correction factor
βp	exponent controlling diffusion strength of pore water flow
γ_g	isentropic expansion factor
γ_T	exponent in Tait's equation
$\delta()$	Dirac delta function
$\delta^{\alpha\beta}$	unity tensor
Δ	filter length in Smagorinsky model
Δ_p	particle spacing
Δt	time step
Δx_p	axial extend of propeller actuator disc
Δy	extension of transverse thruster actuator disc
ϵ	strain
$\epsilon^{\alpha\beta\gamma}$	permutation tensor
$\dot{\epsilon}$	strain rate
$\tilde{\epsilon}_p$	smoothing factor, pressure field
$\tilde{\epsilon}_v$	smoothing factor, velocity field
ζ	blending function
η	height of water column, Martin and Moyce test-case
κ	scaling parameter for kernel range
μ	dynamic viscosity
μ_c	Chézy viscosity
μ_{max}	threshold viscosity
μ_{susp}	suspension viscosity
μ^*_{susp}	suspension viscosity, confined by threshold viscosity
μ_t	turbulent Boussinesq-viscosity
ν	Poisson ratio
ρ	density

ρ_s	soil density
ρ_w	water density
σ	surface stress
σ_m	mean principle stress
τ	deviatoric stress
τ	normalised time, Martin and Moyce test-case
τ_c^*	magnitude of suspension shear-stress
τ_{yield}	yield stress
τ_{m1}	cohesion depending part of yield stress
τ_{m2}	mean principle stress depending part of yield stress
φ	porosity
φ_{FB}	angle of rotation axis
ϕ	internal angle of friction
Ψ	saturation
Ψ'	intermediate saturation
ω_1, ω_2	cylinder angular velocities, Couette test-case
$\dot{\omega}$	rotation rate
Ω	volumetric fraction

Indices

$^{\alpha}$, $^{\beta}$, $^{\gamma}$	spatial directions of vectors and tensors
^{d}	dimension of spatial domain
$_{c}$	Chézy property
$_{cap}$	capillary property
$_{\mathbf{f}}$	water phase
$_{FB}$	floating body property
$_{i}$	focal particle
$_{j}$	neighbouring particle
$_{p}$	propeller property
$_{\mathbf{p}}$	pore water property
$_{\mathbf{s}}$	soil phase

se	soil phase, elastic model
ses	soil phase, elastic model, scaled
sf	soil phase, fluid model

Abbreviations and acronyms

6DOF	Six Degrees of Freedom
BEM	Boundary Element Method
BH	Barnes and Hut
CFD	Computational Fluid Dynamics
CFL	Courant–Friedrichs–Lewy
CPU	Central Processing Unit
DFG	Deutsche Forschungsgemeinschaft
LES	Large Eddy Simulation
LHS	Left Hand Side
FE	Finite-Element
FEM	Finite-Element-Method
FV	Finite-Volume
GPGPU	General Purpose Computation on Graphics Processing Unit
ISPH	Incompressible Smoothed-Particle-Hydrodynamics
MPI	Message Passing Interface
KCS	KRISO Container Ship
KRISO	Korea Research Institute of Ships and Ocean Engineering
RANS	Reynolds-Averaged-Navier-Stokes
RHS	Right Hand Side
SPH	Smoothed-Particle-Hydrodynamics
SPMD	Single-Program Multiple-Data
TEU	Twenty-foot Equivalent Unit
VoF	Volume Of Fluid
WCSPH	Weakly Compressible Smoothed-Particle-Hydrodynamics
XSPH	extended SPH

1 Introduction

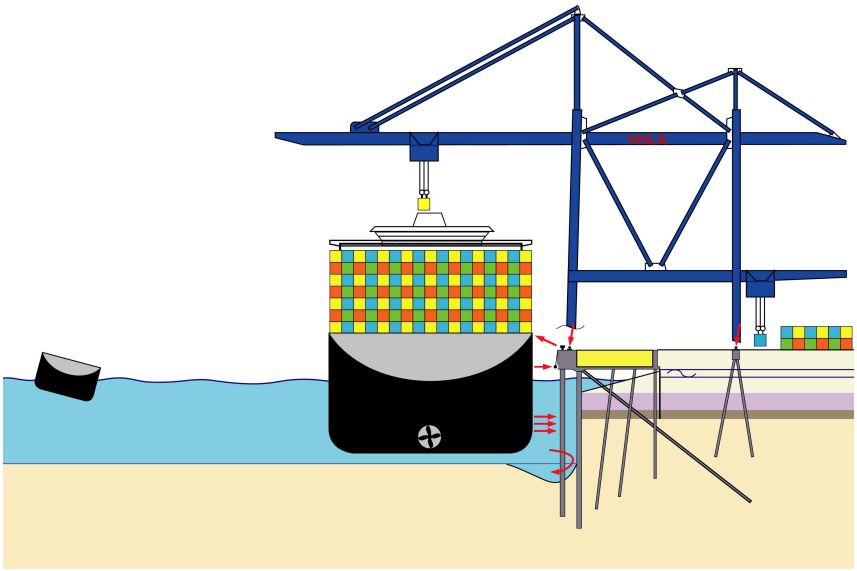

Figure 1.1: Sketch of a typical port facility with interactions between ship, water, soil, quay wall and crane.

1.1 Background and motivation

In 2011, Maersk Line ordered twenty “Triple-E” container vessels, each with a maximum container capacity of 18 000 TEU. They will be the longest vessels in existence when they come into service in 2013 [72]. The “Triple-E” ships represent the present peak of the continuous growth in maximum container ship sizes that takes place since the introduction of seaborne container trade in the 1960’s (cf. Fig. 1.2). Still, the capacity limit is probably not yet reached, as ships for 22 000 TEU have already been announced [72]. Evidently, the increased capacities yield larger ship dimensions as summarised in Tab. 1.1. Even more important than the increasing maximum ship sizes, the average vessel capacity as well is subject to a significant growth. Within the last twenty years, the mean capacity

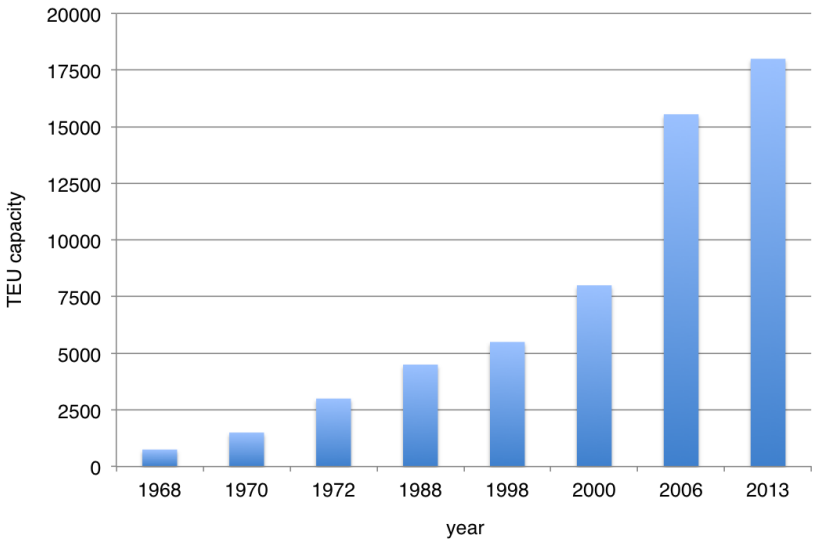

Figure 1.2: Development of maximum container ship capacities [42, 72, 62, 71].

Table 1.1: Typical container vessel main dimensions [71, 72].

TEU	4500	7500	9500	14500	18000
Length	283.0 m	304.0 m	321.0 m	395.0 m	400 m
Breadth	32.3 m	42.8 m	45.5 m	57.0 m	59.0 m
Draught	13.5 m	14.5 m	15.0 m	15.0 m	14.5 m

more than doubled from 1 250 TEU in 1990 to 2 875 TEU in the beginning of 2011 [36].

As illustrated in Fig. 1.1 typical port facilities are exposed to complex interactions between container cranes, ships, quay wall, water and soil. The rising ship dimensions pose challenges to various aspects of harbour construction. Container ships of future generations might require larger container cranes and faster container handling facilities which induce higher loads into the quay construction. The manoeuvrability of large vessels under low speed shallow water conditions becomes rather difficult and the probability of collisions as well as groundings increases. Furthermore, strong ship induced swell can damage embankments and waterfronts. Due to necessarily increased powers of main propulsion and manoeuvring devices, erosions and scours of the harbour bottom are likely to occur more frequently and more pronounced. Fundamental research into the interaction of ship, fluid, structure and soil is needed to meet such challenges. The present work forms part of the German Research Foundation (Deutsche Forschungsgemeinschaft, DFG) Research

Figure 1.3: Scouring of the waterway bottom induced by an inland vessel during a full-scale experiment by Felkel and Steinweller [24].

Training Group “Ports for Container Ships of Future Generations” (GRK 1096) and aims for the development of adequate engineering methods to analyse ship induced scouring of harbour bottoms.

Flow-induced erosion problems are not limited to port hydrodynamics. The interaction of water and soil in the vicinity of floating or bottom-founded structures poses challenges to marine, hydraulic and environmental engineering. Flow-induced sediment scours are frequently observed undesirable water/soil interaction processes. In the area of ocean engineering such scours often occur around platform legs or sub-sea pipelines due to locally increased flow velocities. In the context of port engineering, scours are typically observed next to quay walls, where they are induced by the operation of transverse thrusters and propellers or the flow around the shoulders of manoeuvring ships. Similar damages appear at inland waterway bottoms (cf. Fig. 1.3). A comprehensive overview of marine scour is given in the book by Sumer and Fredsøe [98]. Scours can be several meters deep and significantly weaken the structural support. Further relevant water/soil interaction problems are found in geotechnical and environmental engineering, e.g. when investigating embankment failures, where seepage induced soil erosion is a matter of serious concern.

This research’s aim is therefore the development of a general numerical procedure that can cope with full scale simulations of ship manoeuvres in confined waters above loose soil and the corresponding multi-physics phenomena. Still, it should also be applicable to a wide range of ocean and hydraulic engineering problems. The accurate prediction of the

flow-induced soil erosion requires appropriate water/soil interaction models as well as the ability to mimic the associated large soil deformation. Most of the present simulation tools solve the flow field typically using e.g. the Finite Volume (FV) method in conjunction with semi-empirical transport equations for the sediment, cf. the comprehensive review by Papanicolaou et al. [78]. Such methods provide a reasonable accuracy for applications which solely focus on bottom topography changes. However, they do not resolve the soil. The latter represents an essential feature if combined loads from the fluid and soil phase on constructions are to be evaluated. When attention is given to computational soil mechanics, simulations are commonly based upon Finite-Element-Methods (FEM). The limitations of mesh-based FE/FV-methods occur in conjunction with large soil deformations and large relative motions which evidently occur during the formation of soil scours. Mesh-free simulation approaches like Smoothed-Particle-Hydrodynamics (SPH) can be of advantage when aiming at large deformations. The simulation of large relative motion is a principal asset of the SPH approach. It also represents a promising numerical technique for monolithic calculations of multiple continua (water, soil, water/soil-suspensions). Therefore, SPH provides the methodological basis for this thesis.

1.2 Ship induced scours in harbours

Erosions generated by ships occur due to the restricted flow around hulls under shallow water conditions and the impact of propulsion and manoeuvring devices. In the following, the two latter cases are outlined in detail.

Generally, it can be distinguished between scours close to quay walls being created by deflected propeller or transverse thruster jets and those generated by propellers without the presence of lateral structures [98]. The first cases represent typical problems in ports. As investigated by Felkel and Steinweller [24], the second type of erosions also occur in rivers and channels caused by inland water vessels.

Figures 1.4 - 1.7 illustrate the typical scouring mechanisms. Transverse thrusters (as shown in Fig. 1.4) are used by most modern ships for harbour manoeuvres. Especially when leaving a berth, deflected thruster jets can cause severe damages of the harbour

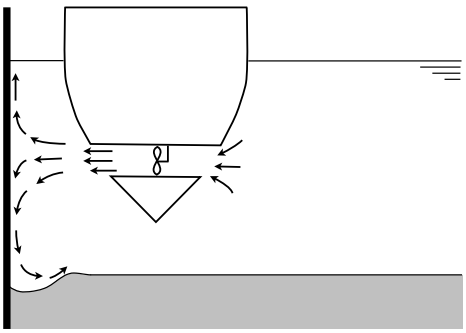

Figure 1.4: Scour due to a deflected transverse thruster jet.

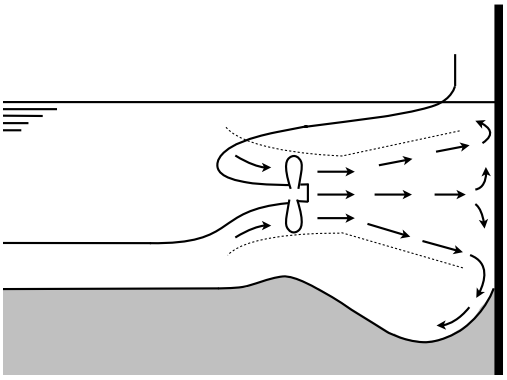

Figure 1.5: Scour due to a deflected propeller jet.

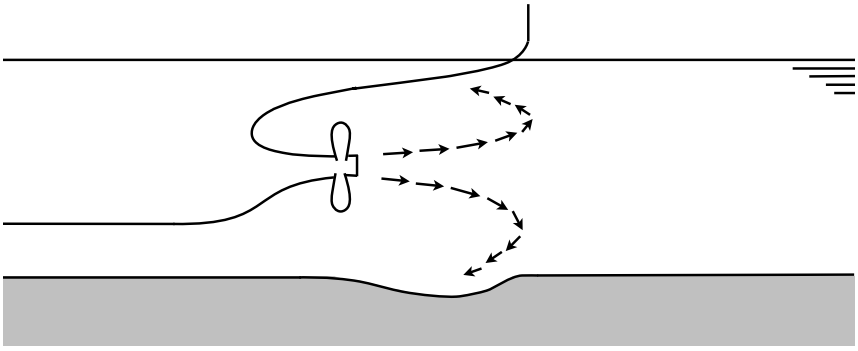

Figure 1.6: Erosion induced by vortical flow from a starting propeller.

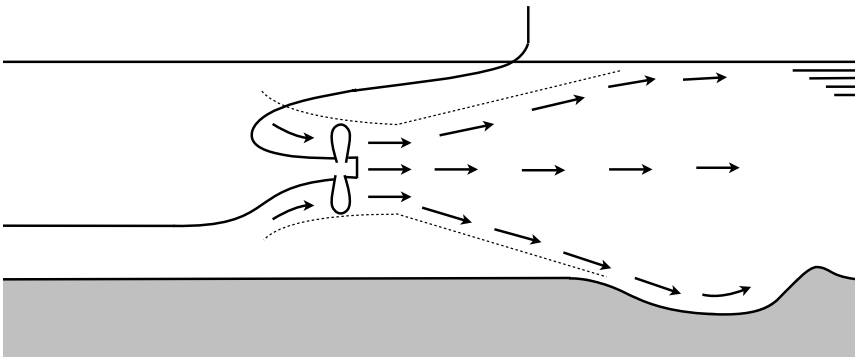

Figure 1.7: Scour induced by the expanding jet of a ship propeller.

bottom in the vicinity of quay walls. The resulting scours can significantly weaken the structure's bearing capacity. A similar scenario is depicted in Fig. 1.5. In this case, the ship's propeller jet is deflected by a wall. Such problems can typically be found at ferry terminals where RoRo ships are loaded and unloaded via stern ramps. Figures 1.6 and 1.7

refer to propeller induced erosions that are not caused by deflected jets but reverse flow regimes and swirl from starting propellers (Fig. 1.6) as well as the impact of expanding jets at a certain distance behind the ship (Fig. 1.7).

Ship induced scouring and its consequences for quay constructions causes serious problems as illustrated for instance by an entire PIANC bulletin [81] and a comprehensive summary by Hamill et al. [33]. Impressive statistics which indicate the need for countermeasures in a large number of harbours have been published by Bergh and Magnussson [6], Longe et al. [50] and Qurrain [84]. Remedial actions against scours are rather expensive as pointed out by Miller and Dücker [63]. Costs for typical constructional measures, including e.g. rip-raps, geotextile protection mats or additions to the penetration depth of sheet pilings, lie in the range of 1 - 5 Mio. € per berth.

Research towards the predictability of propeller induced scouring has been ongoing for the last decades. Experimental investigations have e.g. been reported by Felkel and Steinweller [24] who carried out full-scale and model tests dealing with the action of inland vessel propulsors on the waterway bottom. Their tests highlight the significant erosional potential of propeller wash and show the basic reproducibility of the full-scale experiments during laboratory model tests. Blaauw and van de Kaa [7] presented further ship model tests measuring both the velocity distribution behind the propeller and the bottom erosion. Attention was also paid to variable clearances between propeller and ground. An outcome of the work is a basic framework of equations for the dimensioning of bottom protection materials. More general research about the erosions caused by plane jets is reported by Rajaratnam [85]. Rajaratnam's work shows that the erosion profiles assume an asymptotic state after a certain impact time. Chin et al. [16] further investigated the erosional mechanisms of jets around piles which has been extended to pile groups by Yüksel et al. [114]. Such tests show that, in addition to jet expansion, pile obstruction effects can play an important role in the overall scouring. Schmidt [90] detailedly studied the flow induced by different propulsion and manoeuvring devices including deflected jets from walls and the corresponding flow topologies. Recent scouring model test by Geisenhainer and Aberle [26] refer to the time evolution of ship induced scours due to different propulsion systems.

Extensive practical and theoretical work has been published by Hamill et al. [32, 33, 87] focussing on the scouring processes in harbours. Semi-empirical equations to estimate

the expected scour depths have been derived from the experiments of Hamill. Following Hamill [33], the evolution of the maximum scour depth ϵ_m caused by an unobstructed propeller wash can be written as a logarithmic function of the time t and several parameters:

$$\epsilon_m = \Omega_H \left[ln(t)\right]^{\Gamma_H} \ , \tag{1.1}$$

with

$$\Omega_H = 6.9 \cdot 10^{-4} \left(\frac{C_p}{d_{50}}\right)^{-4.63} \left(\frac{D_p}{d_{50}}\right)^{3.58} F_0^{4.535} \ ,$$

$$\Gamma_H = 4.113 \left(\frac{C_p}{d_{50}}\right)^{0.742} \left(\frac{D_p}{d_{50}}\right)^{-0.522} F_0^{-0.682} \ ;$$

and

$$F_0 = \frac{V_0}{\sqrt{g d_{50} \frac{\Delta\rho}{\rho_w}}} \ ,$$

where V_0 denotes the efflux velocity in millimeters per second, d_{50} is the median sediment grain size in meters, D_p represents the propeller diametre in meters, C_p is the clearance distance between the propeller tip and the seabed in meters, ρ_w denotes the water density, $\Delta\rho$ describes the difference between water and soil density, and g is the acceleration due to gravity. The factors Ω_H, Γ_H, and F_0 are dimensionless numbers and the time t is taken in seconds, while the resulting scour depth ϵ_m is measured in millimeters. Thus, Eq. (1.1) should be interpreted as a best fit to field measurements without a straight connection to the involved continuum mechanics. Such estimations are useful to get a rough impression of the erosion's magnitude but do not account for problem specific geometries, material properties and complex flow topologies.

Literature references to numerical simulations of propeller scours that solve the flow field and the evolution of the waterway bottom are rare. Perez and Caliendo [80] presented a work applying a FV solver in conjunction with a sediment transport equation to the propeller wash. Their applied simulation framework does not solve the overall problem in a monolithic way and does not allow for any evaluation of the stress within the soil phase.

Accordingly, this work presents an approach based on the mesh-free SPH method that can cope with the relevant physics and might be able to overcome the limitations of other state of the art tools.

1.3 Smoothed-Particle-Hydrodynamics

The majority of state-of-the-art simulation tools for continuum mechanics relate to mesh-based Finite-Volume (FV) or Finite-Element (FE) solvers. Such traditional grid-based numerical methods provide a good predictive accuracy and can be applied to a wide range of engineering problems. However, these approaches have limitations, especially if it comes to applications that involve: large relative motions, multiple interacting rigid structures, multiple phases and continua, complex free surface flows, large deformations, and fragmentation of solids.

Contrary to this, mesh-free methods solve the governing equations without a rigid alignment to grid structures or discrete topologies. That way, many of the above mentioned drawbacks of mesh-based procedures can easily be overcome. Several mesh-free techniques have been developed in the last decades; good summaries are given e.g. in a review paper of Belytschko et al. [5], the PhD thesis of Chaniotis [15] and the book of Liu [48]. Some of the formulations still incorporate grids as necessary ingredients of the numerical method. On the contrary, Smoothed-Particle-Hydrodynamics (SPH) can be considered a truly mesh-free approach. In SPH, the continuum is descritised by set of finite particles that can arbitrarily move. By using an interpolation technique known as reproducing kernel approximation, field values can be approximated at a certain point as a weighted average over a set of nearby particles.

Comprehensive introductions into SPH can be found in the books by Liu and Liu [49] and Violeau [108]. The method was originally developed in 1977 independently by Lucy [51] and Gingold and Monaghan [27] to study cosmological problems. Since then, it has considerably matured [66, 49, 86] and was successfully used to study problems from a large variety of disciplines. Its highly diverse range of applications has recently been extended to marine, hydraulic, geoenvironmental and geotechnical engineering problems. Published examples include, but are not limited to, general free-surface flows [65], ship dynamics [58], landslide simulations [82, 79], reservoir flushing [55], flood simulations [103] or embankment failures [13, 14]. State-of-the-art models cover only partial aspects of the flow phenomena related to port hydrodynamics. The present work aims at filling the respective gaps between existing strategies and new approaches are introduced where required.

1.4 Aim and starting point of the thesis

The overall goal of this thesis can be summarised as the development of a numerical procedure based on SPH for the simulation of ship induced erosions of harbour grounds. The massively parallel open source cosmological TreeSPH-Code GADGET-2 developed by Springel [95] was chosen to form the basis for the procedure. The code offers an efficient MPI-based parallelisation and a well structured and easy to adapt implementation. In its original version, GADGET-2 comprises a Tree algorithm for N-body simulations accounting for gravitational interactions between particles and a SPH part to simulate gas dynamics.

In order to reach the goal, the following key issues need to be addressed:

- reliable models for incompressible, viscous fluids and wall-bounded turbulent flows
- development and implementation of a water/soil interaction approach based upon models for soil and water/soil suspensions
- computational modelling of body motions for rigid, floating bodies coupled to SPH
- modelling of propulsion and thruster units
- efficiency enhancements to support the feasibility of full-scale simulations of ships in harbours using variable resolution particles

The accordingly modified code version will be referred to as GADGET-$^{\mathrm{H}}2^{\mathrm{O}}$. GADGET-$^{\mathrm{H}}2^{\mathrm{O}}$ preserves the parallel efficiency of the original code showing a linear speed-up up for several hundred CPU-cores when applied to hydrodynamic problems with several millions of particle [100, 101].

1.5 Present contributions

The specific contributions to the field of multi-physics Smoothed-Particle-Hydrodynamics simulations in a marine engineering context can be summerised as follows:

- Constitutive models to capture water flows, motion of fully and partly saturated soil, and water/soil-interaction are implemented into the GADGET-$^{\mathrm{H}}2^{\mathrm{O}}$ procedure. Water is represented by state-of-the-art SPH models for Newtonian fluids and turbulent

flows. Viable SPH approaches to mimic soil and water/soil interaction are derived, implemented and validated. The latter includes

  - a soil model that bridges between a quasi-static solid state and a strain-rate driven fluid state. The approach handles small deformations by the linear elastic approach supplemented by a yield model to capture plasticity. Dynamic soil motions with large deformations and high strain rates are considered by describing the material as a non-Newtownian fluid. A blending function is applied to switch between the two states avoiding a superposition of stresses from the two model branches and potential numerical problems in cases of zero strain.
  - a simple Eulerian model for seepage flow through porous media. The approach solely uses soil particles to represent partly saturated soil. The soil particles' effective cohesion is changed according to the saturation level. Flow through the soil skeleton is modelled by a Darcy equation.
  - a suspension model for the treatment of water/soil-interfaces and water/soil-mixtures. The approach is based on an empirical Chézy-Ansatz casted into a variable viscosity formulation. It depends on the local flow velocity, a friction coefficient and the local strain rate and bridges between the pure water and pure soil regimes. The technique represents a key feature for the simulation of erosional processes.

- Ships are represented as floating rigid bodies that receive forces from propulsion and manoeuvring devices. This is realised by

  - a six degree of freedom motion solver based on quaternions. This allows for simulations of arbitrary body motions without the limitations of a gimbal lock.
  - body-force propulsor models. A simple jet model is used for the representation of transverse thrusters. Propellers are modelled by a more complex approach taking into account a radial lift distribution over the propeller radius as well as rotational flow components. Both propulsion devices are not geometrically resolved but included by spatially prescribed actuator discs. The corresponding thrust is handed to the motion solver.

- A variable particle resolution strategy is introduced that is based on changing the particle mass and kernel length depending on its position. The approach features

a constant number of particles, which is beneficial for maintaining load balancing of parallel processes, and conserves density and momentum by adding appropriate source terms to the governing equations. Changes of the particle properties are analytically prescribed. Thus, the approach does not causes a computational surplus.

- Numerical schemes to enhance the accuracy of field values are outlined. Special attention is paid to the pressure evaluation at the water/soil interphase by introducing a density blending approach and the development of invariant weighting factors associated to an additional smoothing of the velocity and pressure field.

All models are scrutinised by a variety of verification and validation cases including pure water flows, pure soil motions, suspension flows, seepage induced failures, pressure evaluation, variable particle resolutions, and floating body motion. GADGET-$^{H}2^{O}$ is applied to complex simulations of hydrodynamic problems. Two examples presented in this thesis refer to the scouring close to a quay wall by a transverse thruster and the waterway bottom erosion by a starting propeller of a container vessel. Supplementary ocean engineering application cases refer to foundation installation and jacket launching processes.

1.6 Layout of the thesis

The remainder of the thesis is divided into the following chapters:

Chapter 2 – Governing Equations describes the basic equations which are used to calculate the material behaviour.

Chapter 3 – Fundamentals of Smoothed-Particle-Hydrodynamics outlines the basic formulations of the Smoothed-Particle-Hydrodynamics method. SPH approximations of the governing equations are derived. Furthermore, the difference between truly incompressible and weakly compressible SPH is briefly discussed followed by an outline of typical state equations for pressure evaluations. Finally, different concepts for rigid boundaries are described. The formulations subsequently used by GADGET-$^{H}2^{O}$ are indicated.

In **Chapter 4 – Constitutive Models**, the constitutive models for viscous, turbulent fluids, soil and water/soil-suspensions are derived. Together with the following chapter, this part

of the thesis detailedly describes the physical models which are applied in this work to cope with complex harbour hydrodynamic problems.

The physical modelling of self propelled ships is subject of **Chapter 5 – Self Propelled Ships**. The 6DOF motion solver as well as body force models for propellers and thrusters are introduced.

Chapter 6 – Variable Particle Resolution provides a brief summary of state-of-the-art variable resolution techniques in SPH prior to a detailed description of the new variable mass approach.

Chapter 7 – Numerical Model deals with the actual implementation of the different physical models into the GADGET-$^{H}2^{O}$ framework. Computational details like correction and stabilization schemes, boundary conditions, neighbour search, parallelisation and time integration are outlined.

Various verification and validation test-cases are presented in **Chapter 8 – Validation and Verification**.

Chapter 9 – Applications is devoted to full scale applications investigating ship induced scours in harbours. In addition, two alternative application examples from the field of offshore engineering are presented.

Finally, **Chapter 10 – Summary and Perspectives** presents a summary, conclusions and an outlook to possible future work.

2 Governing Equations

The present work pursues a monolithic formulation for the interaction between fluids, granular materials, suspensions and structures. All involved phases are captured by an identical framework of conservation laws and adjustments – being applied to single phase regimes as well as mixtures – are confined to material specific closure conditions and constitutive models.

In the following, vectors and tensors are defined by reference to cartesian coordinates. Greek superscripts (α, β, γ) refer to the different coordinate axes. Einstein's summation is employed over repeated Greek superscripts.

2.1 Continuity equation

The continuity equation describes the conservation of mass. In a Lagrangian framework this reads

$$\frac{D\rho}{Dt} + \rho \, \nabla^\alpha v^\alpha = s_m \ , \tag{2.1}$$

with the material density ρ, the velocity vector v^α and D/Dt, representing the substantial derivative by time t. The source term s_m is zero for source-free fields. In that case, Eq. (2.1) reduces to

$$\frac{D\rho}{Dt} = -\rho \, \nabla^\alpha v^\alpha \ . \tag{2.2}$$

2.2 Momentum equation

The momentum equation establishes a relationship between the stresses acting on a piece of matter and its acceleration. The mass specific momentum equation reads

$$\frac{Dv^\alpha}{Dt} = \frac{1}{\rho} \left[\nabla^\alpha \sigma^{\alpha\beta} + f^\alpha \right] + s_v \ , \tag{2.3}$$

with

$$s_v = -v^\alpha s_m \frac{1}{\rho} \, . \tag{2.4}$$

The vector f^α refers to external volumetric forces like e.g. gravity or other body forces. The surface stress tensor $\sigma^{\alpha\beta}$ can be split into an isotropic pressure portion representing the mean normal stresses and a deviatoric part:

$$\sigma^{\alpha\beta} = -p\delta^{\alpha\beta} + \tau^{\alpha\beta} \, , \tag{2.5}$$

with the pressure p, the unity tensor $\delta^{\alpha\beta}$ and the traceless deviatoric stress tensor $\tau^{\alpha\beta}$. Figure 2.1 illustrates the total surface stress tensor acting on an infinitesimal piece of material. The pressure p can be redefined in relation to the trace of the stress tensor, viz.

$$p = -\frac{1}{3}\left(\sigma^{11} + \sigma^{22} + \sigma^{33}\right) \, . \tag{2.6}$$

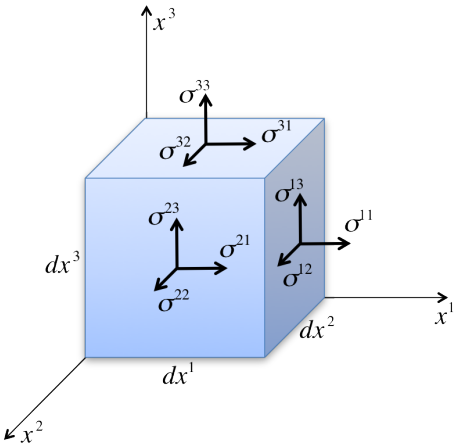

Figure 2.1: Schematic illustration of the stress tensor $\sigma^{\alpha\beta}$ acting on an infinitesimal piece of material.

3 Fundamentals of Smoothed-Particle-Hydrodynamics

"SPH provides a fascinating tool that has some of the properties of molecular dynamics while retaining the attributes of the macroscopic equations of continuum mechanics."

J. J. Monaghan [66]

This chapter outlines the essential formulations of the Smoothed-Particle-Hydrodynamics methodology. Starting from a continuous integral approximation of function values and the respective spatial derivatives (section 3.1), the discrete SPH summation approximations are derived in section 3.2. Kernel functions, representing a main element of the method, and their properties are introduced in section 3.3. These basic elements are applied in section 3.4 to the governing equations given in the previous chapter. Section 3.5 introduces state equations for the pressure evaluation of compressible and weakly compressible fluids. Finally, an overview on typical models for rigid boundaries is presented in section 3.6.

More comprehensive details of the method can be found in books by Liu and Liu [49] and Violeau [108]. It should be noted that the chapter does not discuss any numerical issues of the actual GADGET-$^{\mathrm{H}}2^{\mathrm{O}}$ implementation. This is matter will be outlined in *Chapter 7 – Numerical Model*.

3.1 Integral approximation

Function values

The basic principle of Smoothed-Particle-Hydrodynamics is an integral representation of arbitrary spatial functions $f(x^\alpha)$. The local value is exactly reproduced by the integral identity

$$f(x^\alpha) = \int_\Omega f(x'^\alpha)\, \delta(x^\alpha - x'^\alpha)\, dx'^\alpha \,, \tag{3.1}$$

with the surrounding values $f(x'^\alpha)$, the surrounding volume Ω and the Dirac delta function δ

$$\delta(x^\alpha - x'^\alpha) = \begin{cases} 1 & \text{if} \quad x^\alpha = x'^\alpha \\ 0 & \text{if} \quad x^\alpha \neq x'^\alpha \,. \end{cases} \tag{3.2}$$

The numerical strategy involves two primary steps, i.e. a mollification step which approximates the Dirac delta function by a smooth analytical kernel function W and a discretisation step which performs the quadrature. The mollification step is leading to the reproducing kernel approximation of a function f

$$f(x^\alpha) \approx \int_\Omega f(x'^\alpha)\, W(x^\alpha - x'^\alpha, h)\, dx'^\alpha \,. \tag{3.3}$$

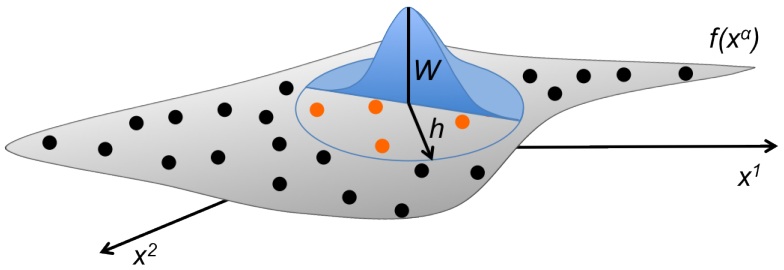

Figure 3.1: Two-dimensional function $f(x^\alpha)$ and the respective reproducing kernel approximation.

The spherical kernel function covers the volumetric fraction Ω which is proportional to the isotropic smoothing length h. Anisotropic kernel functions are rather exceptional [77]. Note, that many publications define the range of W to be $2h$ while the present work will generally refer to a coverage h. Figure 3.1 provides a schematic sketch of the basic principle in 2D: $f(x^\alpha)$ is reproduced by a kernel approximation. The kernel function

W is established at an arbitrary position x^α accounting on surrounding function values x'^α represented by the orange dots. Black dots denote locations outside the range of the smoothing length h. As shown in Fig. 3.1, W typically refers to a bell-shaped, even function that provides a compact support. Further requirements that should be fulfilled by W are discussed in section 3.3.

Function gradients

The approximation (3.3) can directly be applied to function gradients, viz.

$$\nabla^\beta f(x^\alpha) \approx \int_\Omega \left[\nabla^\beta_{x'} f(x'^\alpha)\right]\ W(x^\alpha - x'^\alpha, h)\ dx'^\alpha\ . \tag{3.4}$$

Gauss's theorem states that

$$\int_\Omega \nabla^\beta_{x'}\left[f(x'^\alpha) W(x^\alpha - x'^\alpha, h)\right]\ dx'^\alpha =$$

$$\int_\Omega f(x'^\alpha)\ \left[\nabla^\beta_{x'} W(x^\alpha - x'^\alpha, h)\right] + \left[\nabla^\beta_{x'} f(x'^\alpha)\right]\ W(x^\alpha - x'^\alpha, h)\ dx'^\alpha$$

$$= \int_{\partial\Omega} f(x'^\alpha) W(x^\alpha - x'^\alpha, h)\ dS'^\beta\ , \tag{3.5}$$

which can be rearranged and applied to (3.4)

$$\nabla^\beta f(x^\alpha) \approx \int_\Omega \left[\nabla^\beta_{x'} f(x'^\alpha)\right]\ W(x^\alpha - x'^\alpha, h)\ dx'^\alpha$$

$$= \int_{\partial\Omega} f(x'^\alpha) W(x^\alpha - x'^\alpha, h)\ dS'^\beta - \int_\Omega f(x'^\alpha)\ \left[\nabla^\beta_{x'} W(x^\alpha - x'^\alpha, h)\right]\ dx'^\alpha\ . \tag{3.6}$$

The surface integral in Eq. (3.6) vanishes for sufficiently submerged locations inside the fluid domain due to the compact support property of W. It is difficult to evaluate and thus a priori neglected by most SPH practitioners. Neglecting the surface integral, the integral approximation of gradients becomes

$$\nabla^\beta f(x^\alpha) \approx -\int_\Omega f(x'^\alpha)\ \nabla^\beta_{x'} W(x^\alpha - x'^\alpha, h)\ dx'^\alpha\ . \tag{3.7}$$

In conclusion, the gradient operation has been shifted away from the function f onto the kernel function. In case that gradients of W can be evaluated analytically, this shift significantly simplifies the overall procedure. However, as outlined by Colagrossi et al. [19], neglecting the surface integral is an approximation that impairs the accuracy and convergence along rigid boundaries and the free surface which may motivate further modifications of the gradient approximation.

3.2 Discrete summation approximation

The numerical integration forms the second main step towards an SPH formulation. Accordingly, the previously described integrals are converted into discrete summations. Equations (3.3 and 3.7) can be approximated by

$$f_i^\alpha \approx \sum_{j=1}^{N} V_j \; f_j^\alpha \; W_{ij} \; , \tag{3.8}$$

$$\nabla^\beta f_i^\alpha \approx -\sum_{j=1}^{N} V_j \; f_j^\alpha \;\; \nabla_j^\beta \; W_{ij} = \sum_{j=1}^{N} V_j \; f_j^\alpha \;\; \nabla_i^\beta \; W_{ij} \; , \tag{3.9}$$

with the abbreviation $W_{ij} = W({x_i}^\alpha - {x_j}^\alpha, h)$. Assuming an even kernel function W, one can swap between $-\nabla_j^\alpha W_{ij} = \nabla_i^\alpha W_{ij}$ which is more convenient for the implementation.

Discrete volumes V represent volumetric fractions of the overall domain and are assigned to the individual particles. The particles carry properties like density, mass, pressure, viscosity etc. which can be either fixed or vary in time. The subscript i refers to focal particles while j denotes its neighbours with the total number of neighbours N within the kernel support. The particle volume V_j follows from the relationship

$$V_j = \frac{m_j}{\rho_j} \tag{3.10}$$

with the mass m and density ρ.

Figure 3.2 shows a continuous domain represented by discrete cubic volumes. The focal particle is marked in green and the reference coordinates of neighbours residing inside the kernel support are coloured orange. The domain decomposition follows from the decomposition of the total mass and the particle volumes are thus not aligned with a special shape. Alternatives are for instance given by other polyhedral fragmentations. The volume is however usually associated to the favoured initial particle distance Δ_p which leads to $V_j \sim \Delta_{p_j}^d$ with the exponent d representing the regarded spatial dimension. Note, that V_j and the corresponding masses m_j are reduced to areas and masses per length in 2D. Throughout the simulation, the initial particle distribution is not necessarily maintained. Particles may enter or leave the support regime, which influences the approximation of the domain Ω. The kernel support thus represents an open variable mass system [107]. A reduction of particle distances leads to an overlapping of volume fractions what is usually not an issue for the discrete summation approximation. On the other hand, a significant increase of particle distances can counteract the procedure's convergence. To avoid such

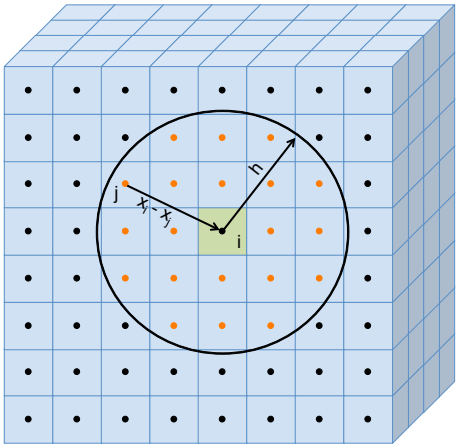

Figure 3.2: Sketch of an exemplary initial spatial domain discretised by SPH particles.

convergence problems, the particles always need to overlap with respect to their kernel coverage h.

Equations (3.8 and 3.9) can now be applied to the governing equations which have been presented in chapter 2.

3.3 Kernel functions

The kernel function W should fulfill several basic conditions. Liu and Liu [49] summarise the following seven constraints:

1. Unity

The kernel function must comply with the normalisation principle

$$\int_{\Omega} W(x_i^\alpha - x_j^\alpha, h)\, dx^\alpha = 1\ . \tag{3.11}$$

This ensures consistent approximations of homogeneous fields which should also be secured in discrete space.

2. Compact support

W needs to provide a compact support (and a limited range, accordingly):

$$W(x_i^\alpha - x_j^\alpha, h) = 0\,, \quad \text{if} \quad |x_i^\alpha - x_j^\alpha| > \kappa h\,, \tag{3.12}$$

with the scaling parameter κ. The condition transforms SPH approximations from global to local operations which leads to a significant reduction of the computational effort.

3. Positivity

The kernel function's output should always be positive:

$$W({x_i}^\alpha - {x_j}^\alpha, h) \geq 0 \tag{3.13}$$

for all particles ${x_i}^\alpha$ and ${x_j}^\alpha$. This condition is not necessary from a mathematical point of view but ensures a plausible reproduction of physical phenomena.

4. Decay

The kernel function should be monotonically decreasing with a growing distance between two particles ${x_i}^\alpha$ and ${x_j}^\alpha$. This restriction follows from the assumption that the influence of neighbouring function values declines with a growing distance.

5. Delta function property

If the kernel function approaches a single point function, W needs to correspond to the Delta-Dirac function

$$\lim_{h\to 0} W(x_i^\alpha - x_j^\alpha, h) = \delta(x_i^\alpha - x_j^\alpha), \tag{3.14}$$

with

$$\delta(x_i^\alpha - x_j^\alpha) = \begin{cases} 1 & \text{if} \quad x_i^\alpha = x_j^\alpha \\ 0 & \text{if} \quad x_i^\alpha \neq x_j^\alpha \end{cases}. \tag{3.15}$$

This condition is automatically fulfilled if W complies with the previous four restrictions.

6. Symmetric property

The kernel function should be even:

$$W(x_i^\alpha - x_j^\alpha, h_j) = W(x_j^\alpha - x_i^\alpha, h_i), \tag{3.16}$$

ensuring that points with the opposite distance always impose the same influence on each other. Assuming an even distribution of particles, the condition helps to maintain a pairwise interaction by means of anti-symmetric forces along the lines of centres between two particles and thus reduces spurious particle motion. On the other hand, asymmetric kernel functions can be of advantage if e.g. particles with different masses and kernel lengths are interacting.

7. Smoothness

The kernel function and its derivatives should be continuous and sufficiently smooth to obtain good approximations. A particle disorder will always occur at a certain level in SPH simulations. A smooth and continuous function is not very sensitive to such disorders and keeps the errors in approximating the integral interpolations small.

Various kernel functions exist which fulfil this set of conditions. They primarily differ with respect to their order. However, the choice of the kernel function influences numerical side-effects, like e.g. tensile instabilities, and slightly affects the final solution as presented e.g. by Macià et al. [53].

Most practically used kernels mimic the bell shape of a Gauss function which is traditionally considered to be the best function to find a plausible physical interpretation of the SPH methodology. Monaghan [64] even declared this consideration “the first golden rule of SPH”. Therefore, the direct application of a Gauss kernel function as it has been done e.g for early SPH-simulations by Gingold and Monaghan [27] is rather obvious. The respective function reads

$$W(R, h) = \alpha_d e^{-(2R)^2}, \tag{3.17}$$

with the relative particle distance $R = \frac{r}{h}$, $r = \left| x_i^\alpha - x_j^\alpha \right|$ and the normalisation parameter α_d depends on the dimension. Values of the dimension parameter are given by $\alpha_d = \frac{2}{\pi^{1/2} h}$, $\alpha_d = \frac{4}{\pi h^2}$, $\alpha_d = \frac{8}{\pi^{3/2} h^3}$ for 1D, 2D and 3D. Note, that contrary to most publication, the notation within this thesis accounts for a nominal kernel range being equal to the smoothing length h. Favourable features of Eq. (3.17) are related to its formulation that

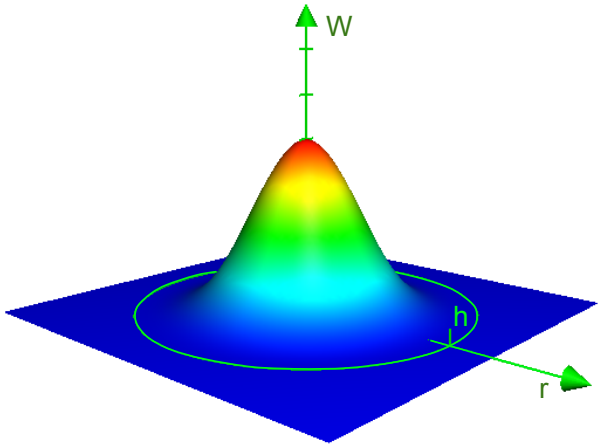

Figure 3.3: Cubic Spline kernel as a function of the particle distance r and the maximum range h.

is not divided into different sections and therefore returns smooth and continuous higher derivatives. The simple formulation also makes it easy to implement.

A disadvantage is that the function will theoretically drop to zero if R approaches infinity, violating the compact support principle. However, it practically approaches zero quite quickly. The compact support can therefore be forced by truncating the kernel with negligible impact on the numerical solution [30].

Alternatives are given by different spline kernel functions. A widely used one is the *Cubic Spline* kernel which is based on B-Splines. Figure 3.3 provides a 2D plot of the function which is also applied in GADGET-$^{\mathrm{H}}2^{\mathrm{O}}$. It was first introduced to SPH by Monaghan and Lattanzio [68]:

$$W(r,h) = \alpha_d \begin{cases} 1 - 6R^2 + 6R^3 & \text{if} \quad 0 \leq R \leq \frac{1}{2} \\ 2(1-R)^3 & \text{if} \quad \frac{1}{2} < R \leq 1 \\ 0 & \text{if} \quad R > 1 \end{cases}, \tag{3.18}$$

with $\alpha_d = \frac{4}{3h}$, $\alpha_d = \frac{40}{7\pi h^3}$, $\alpha_d = \frac{8}{\pi h^3}$ in 1D, 2D and 3D. The kernel function (3.18) as well as its first spatial derivative fulfil the afore listed constraints. A problem occurs if higher derivatives are necessary as the second derivative already becomes a linear step function. This problem can be overcome by applying higher order polynomials, such as

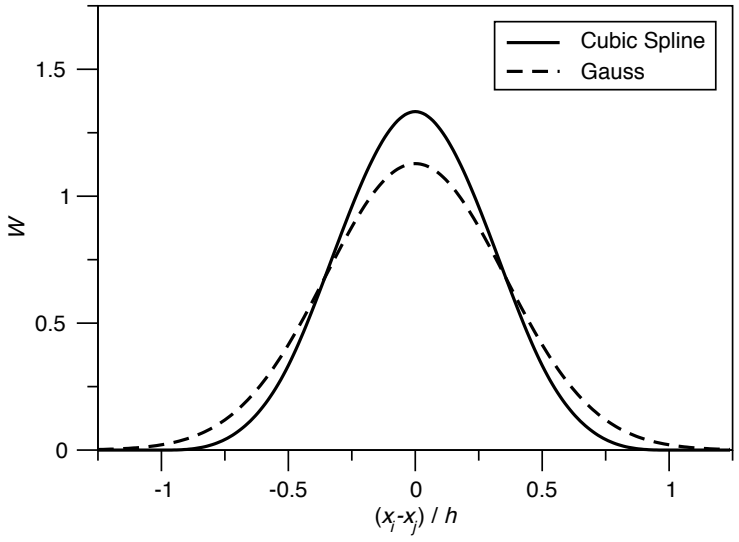

Figure 3.4: Cubic Spline and Gauss kernel functions (1D).

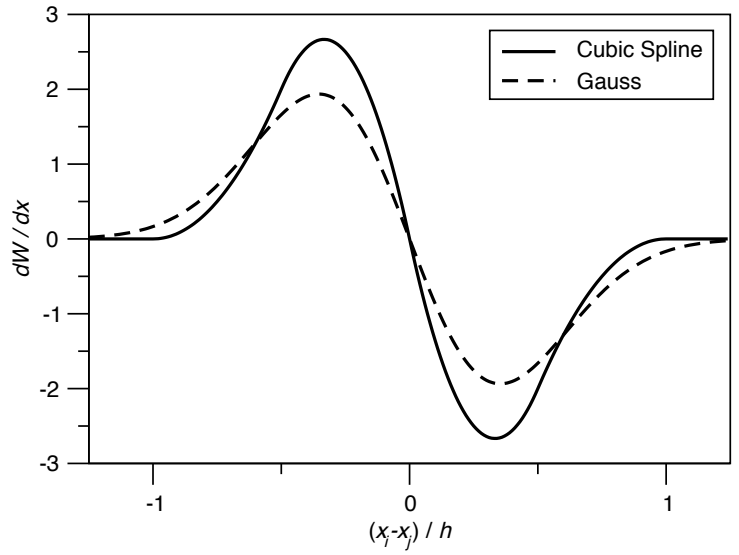

Figure 3.5: First derivative of Cubic Spline and Gauss kernel functions (1D).

Quartic and *Quintic Spline* kernel functions. They are, however, slightly more complex which counteracts the implementation's simplicity. Figures 3.4 and 3.5 illustrate the Gauss kernel and the Cubic Spline kernel function as well as the first derivative of each. Within the scope of this thesis, further kernel functions are not discussed. A comprehensive collection of SPH-kernels can be found for instance in the book by Liu and Liu [49].

The general characteristics of the kernel function makes the approximation of deriva-

tives non-collocational, meaning that the local function value does not contribute to the approximation. Moreover, the mollification does not support local collocation of function values.

3.4 SPH-approximation of the governing equations

3.4.1 Continuity equation

There are two common SPH-approaches for the calculation of the particle density. One possibility is given by a weighted sum over all neighbouring particles. This leads to a simple direct evaluation of the local particle density. The second possibility is an SPH-approximation of the continuity equation.

Direct density evaluation

The application of a weighted sum over neighbour particles according to Eq. (3.8) gives

$$\rho_i = \sum_{j=1}^{N} m_j W_{ij} = \sum_{j=1}^{N} V_j \rho_j W_{ij} \ , \tag{3.19}$$

with $V_j = \frac{m_j}{\rho_j}$.

Continuity equation

If the SPH-operation (3.9) is applied to Eq. (2.2) one gets

$$\frac{D\rho_i}{Dt} = -\rho_i \sum_{j=1}^{N} V_j \, v_j^{\alpha} \nabla_i^{\alpha} W_{ij}. \tag{3.20}$$

Equation (3.20) only considers the velocity of neighbour particles without accounting for the velocity of the focal particle. This can lead to undesired asymmetric particle interaction and might violate Galilean invariance. A variation of (3.20) that includes a relative particle velocity can be derived by making use of the identity

$$\nabla^{\alpha} 1 = 0 \tag{3.21}$$

and its respective SPH-approximation

$$\nabla^{\alpha} 1 = \sum_{j=1}^{N} V_j \nabla_i^{\alpha} W_{ij} = 0 \ . \tag{3.22}$$

The zero term $\rho_i v_i^\alpha \sum_{j=1}^{N} V_j \nabla_i^\alpha W_{ij}$ can be added to the RHS of Eq. (3.20) leading to a symmetric formulation of the continuity equation:

$$\frac{D\rho_i}{Dt} = \rho_i \sum_{j=1}^{N} \left[V_j \left(v_i^\alpha - v_j^\alpha \right) \right] \nabla_i^\alpha W_{ij}. \tag{3.23}$$

An alternative symmetric formulation can be obtained from applying the identity

$$-\rho \nabla^\alpha v^\alpha = -\left[\nabla^\alpha \left(\rho v^\alpha \right) - v^\alpha \ \nabla^\alpha \rho \right] \tag{3.24}$$

to Eq. (2.2) which leads to the discrete form

$$\frac{D\rho_i}{Dt} = v_i^\alpha \sum_{j=1}^{N} V_j \rho_j \nabla_i^\alpha W_{ij} - \sum_{j=1}^{N} V_j v_j^\alpha \rho_j \nabla_i^\alpha W_{ij} \tag{3.25}$$

that is simplified to

$$\frac{D\rho_i}{Dt} = \sum_{j=1}^{N} m_j \left(v_i^\alpha - v_j^\alpha \right) \nabla_i^\alpha W_{ij} \ . \tag{3.26}$$

Both variants (3.26 and 3.23) are usually preferred over (3.20) as they maintain invariance against a moving reference frame. Another advantage is that the term associated to v_i^α acts as a boundary term that vanishes in sufficiently submerged conditions and biases the error from neglecting the surface integral when the kernel is truncated [19, 30]. An interesting explanation for the heuristic modification of Eq. (3.20) is outlined by Vignjevic et al. [107].

Predictive differences between Eqs. (3.23 and 3.26) are related to the treatment of interacting phases with differing densities. Equation (3.23) aims at maintaining the focal particle's density even if the deviation to its neighbours is significant. This corresponds to the physical behaviour of immiscible fluids. On the other hand, Eq. (3.26) reduces density differences which is desirable if mixtures are regarded. The latter is the case in the macroscopic water/soil interaction model which involves suspensions and is applied in this thesis. Accordingly, Eq. (3.26) is used in conjunction with the present code.

Equivalence of direct and continuity approaches

The two different approaches of the density evaluation given by the direct summation Eq. (3.19) and the differential form Eq. (3.26) are formally equivalent as mentioned e.g. by Feldman [23]. Following Feldman, both functions can be rewritten in dependency on the

time t

$$\rho_i(t) = \sum_{j=1}^{N} m_j W(r(t)) \; , \tag{3.27}$$

$$\frac{D\rho_i(t)}{Dt} = \sum_{j=1}^{N} m_j \left(v_i^\alpha(t) - v_j^\alpha(t)\right) \nabla_i^\alpha W(r(t)) \; . \tag{3.28}$$

Subsequently, a constant smoothing length h is assumed. Accordingly, the particle distance r represents the only time dependent variable of the kernel function W. The differentiation of (3.27) with respect to time reads

$$\frac{D\rho_i(t)}{Dt} = \sum_{j=1}^{N} m_j \frac{d}{dt}\left[W(r(t))\right] = \sum_{j=1}^{N} m_j \frac{dr(t)}{dt}\frac{W(r(t))}{dr(t)} \; . \tag{3.29}$$

Introducing the two substitutions

$$\frac{dr(t)}{dt} = \frac{\left(x_i^\alpha(t) - x_j^\alpha(t)\right)\left(v_i^\alpha(t) - v_j^\alpha(t)\right)}{r(t)} \tag{3.30}$$

and

$$\nabla^\alpha W(r(t)) = \frac{1}{r(t)}\frac{dW(r(t))}{dr(t)}\left(x_i^\alpha(t) - x_j^\alpha(t)\right) \tag{3.31}$$

being applied to Eq. (3.29) gives

$$\frac{D\rho_i(t)}{Dt} = \sum_{j=1}^{N} m_j \frac{\left(x_i^\alpha(t) - x_j^\alpha(t)\right)\left(v_i^\alpha(t) - v_j^\alpha(t)\right)}{r(t)} \frac{\nabla_i^\alpha W(r(t))r(t)}{\left(x_i^\alpha(t) - x_j^\alpha(t)\right)} \; , \tag{3.32}$$

leading to

$$\frac{D\rho_i(t)}{Dt} = \sum_{j=1}^{N} m_j \left(v_i^\alpha(t) - v_j^\alpha(t)\right) \nabla_i^\alpha W(r(t)) \; , \tag{3.33}$$

what is equivalent to Eq. (3.28). Therefore, the theoretical solution for both density evaluations will be identical if the initial condition

$$\rho_i(t_0) = \sum_{j=1}^{N} m_j W(r(t_0)) \tag{3.34}$$

is applied to the differential formulation. It should be noted that due to numerical issues, practical solutions will probably be slightly different. Moreover, the equivalence of Eqs. (3.19 and 3.26) is caused by the specific kernel properties and is only valid for isotropic and homogenous kernels.

3.4.2 Momentum equation

Applying the SPH-operation (3.9) directly to the source-free Eq. (2.3) gives

$$\frac{Dv_i^\alpha}{Dt} = \frac{1}{\rho_i} \sum_{j=1}^{N} \left[m_j \frac{\sigma_j^{\alpha\beta}}{\rho_j} \right] \nabla_i^\alpha W_{ij} + \frac{f_i^\alpha}{\rho_i} \,. \tag{3.35}$$

Adding the identity

$$\sum_{j=1}^{N} m_j \frac{\sigma_i^{\alpha\beta}}{\rho_i \rho_j} \nabla_i^\alpha W_{ij} = \frac{\sigma_i^{\alpha\beta}}{\rho_i} \left(\sum_{j=1}^{N} \frac{m_j}{\rho_j} \nabla_i^\alpha W_{ij} \right) = 0 \,, \tag{3.36}$$

the symmetric formulation

$$\frac{Dv_i^\alpha}{Dt} = \sum_{j=1}^{N} m_j \left[\frac{\sigma_i^{\alpha\beta} + \sigma_j^{\alpha\beta}}{\rho_i \rho_j} \right] \nabla_i^\alpha W_{ij} + \frac{f_i^\alpha}{\rho_i} \tag{3.37}$$

is obtained. A third approximation of the momentum equation can be derived if the following identity is used

$$\frac{1}{\rho} \nabla^\alpha \sigma^{\alpha\beta} = \nabla^\alpha \left(\frac{\sigma^{\alpha\beta}}{\rho} \right) + \frac{\sigma^{\alpha\beta}}{\rho^2} \nabla^\alpha \rho \,. \tag{3.38}$$

This leads to the discrete notation

$$\frac{Dv_i^\alpha}{Dt} = \sum_{j=1}^{N} V_j \frac{\sigma_j^{\alpha\beta}}{\rho_j} \nabla_i^\alpha W_{ij} + \frac{\sigma_i^{\alpha\beta}}{\rho_i^2} \sum_{j=1}^{N} V_j \rho_j \nabla_i^\alpha W_{ij} + \frac{f_i^\alpha}{\rho_i} \tag{3.39}$$

and the respective simplification

$$\frac{Dv_i^\alpha}{Dt} = \sum_{j=1}^{N} m_j \left(\frac{\sigma_i^{\alpha\beta}}{\rho_i^2} + \frac{\sigma_j^{\alpha\beta}}{\rho_j^2} \right) \nabla_i^\alpha W_{ij} + \frac{f_i^\alpha}{\rho_i} \,. \tag{3.40}$$

Analogue to the SPH representation of the continuity equation, the two symmetric formulations (3.37) and (3.40) are preferred. If applied to interacting fluids with different densities, Eq. (3.37) tends to mimic the behaviour of immiscible fluids whereas mixture effects are supported by Eq. (3.40). Accordingly, Eq. (3.40) is applied in the present work.

The different SPH-approximations (3.35, 3.37, 3.40) of the momentum equation can be split according to Eq. (2.5) in order to get separate equations for the pressure and the deviatoric stresses. The following section outlines the most common SPH-approach for the pressure evaluations. Deviatoric stresses for water and soil will be derived in Chapter *4 – Constitutive Models*.

3.5 Pressure evaluation

The classical SPH method is based on evaluating pressures of compressible fluids by using a state equation. That method has successfully been transferred to nearly incompressible fluids like water. It is usually referred to the approach as *Weakly Compressible SPH (WCSPH)*. WCSPH is truly explicit and accordingly featuring a simple and efficient algorithm to implement. It shows a sufficient accuracy for a wide range of problems. Especially highly transient flows are well reproduced by the method. However, disadvantages are related to stronger time step restrictions due to the fully explicit formulation and the tendency towards noisy pressure fields as well as particle clustering [113].

An alternative is given by *truly Incompressible SPH (ISPH)*. ISPH can be very accurate and noise free but might get unstable if the particles are highly distorted [47]. The method makes use of the condition that the pressure follows from a projection method [113] which ensures either a vanishing velocity divergence [21], a constant density [91], or a combination [34]. The two constraints are, unfortunately, not synonym in SPH due to the spatial truncation error, thus the pressure is used to control both a regular particle spacing and the divergence of velocity. A similar approach is pursued in most mesh based CFD procedures. Unfortunately, ISPH features implicit links between the pressure and the velocities and requires an iterative solving process. This counteracts the explicit nature of SPH and can lead to high computational efforts, particular since the remainder of the approach generally is of explicit nature and must obey to CFL criteria. The ISPH approach is not applied in the present study and will therefore not further be discussed. Detailed descriptions are e.g. given by Lee et al. [44] or Xu et al. [113].

Weakly Compressible Smoothed-Particle-Hydrodynamics (WCSPH)

SPH has originally been developed to study astronomical phenomena including compressible gas dynamics. In his widely cited 1977 paper, Lucy [51] evaluated gas pressures according to the state equation for ideal gases

$$p = \rho R_g T \tag{3.41}$$

with the temperature T and the specific gas constant R_g. Generally, an additional transport equation for the temperature needs to be solved if Eq. (3.41) is applied. Considering

isentropic processes, the pressure/density-relation obeys to

$$\frac{p}{p_0} = \left(\frac{\rho}{\rho_0}\right)^{\gamma_g} \tag{3.42}$$

with the reference density ρ_0, reference pressure p_0 and the isentropic expansion factor γ_g. Typical values read $\gamma_g = \frac{5}{3}$ for inert gas and $\gamma_g = 1.4$ for dry air.

Compared to gases, a relevant compressibility of water appears only at very high pressures (corresponding values are e.g. reported by Borchers et al. [8]). Water is therefore usually modelled as an incompressible fluid. Still, Monaghan [65] introduced an equation of state for SPH-simulations of water flows very similar to the perfect gas equation of state:

$$p = \left(\left(\frac{\rho}{\rho_0}\right)^{\gamma_T} - 1\right) B \tag{3.43}$$

with the reference pressure B. The equation has been recommended e.g. by Batchelor [4] and MacDonald [52] as a physically correct state equation for water. According to Cole [20], the parameters γ_T and B have empirically been obtained for seawater as $\gamma_T \approx 7.15$ and $B \approx 3.047 \cdot 10^8$ Pa. Equation (3.43) is commonly called *Tait's equation* as the compressible behaviour of water has initially been investigated by Peter Guthrie Tait during the Challenger expedition (1872-1876).

Following Monaghan [65], most SPH researchers using WCSPH adopt Eq. (3.43) with $\gamma_T = 7$. A particular problem is related to the reference pressure B, as the employment of water specific values for B leads to practically unfeasible time-step limits. The Courant number restricts the time step size to preserve a stable response of the discrete approach to numerical disturbances. With respect to disturbances of the pressure force, the restriction states that the maximum time step size is limited by the spatial resolution (represented by the kernel length h) and the reciprocal speed of sound $1/c$:

$$\Delta t \sim \frac{h}{c} \tag{3.44}$$

A correlation between the pressure and the speed of sound is given by:

$$p = \frac{c^2 \rho}{\gamma^T} \tag{3.45}$$

Applying (3.45) to (3.43) yields

$$B = c^2 \frac{\rho_0}{\gamma_T} \tag{3.46}$$

in the limit of small relative density variations. Bearing in mind the high experimentally reported values of B, the CFL restriction (3.44) motivates the use of a more practical

definition for c than (3.46). Monaghan introduced an artificial compressibility to reduce the speed of sound and to mitigate the time step restriction. The basic idea is that fluids can generally be considered as incompressible if the Mach number stays small. Since differences due to compressible phenomena scale with $1 - M^2$, the typically assigned limit is $M \sim 0.1$. To stay below this bound, the minimum speed of sound is defined as

$$c = 10 v_{max} \ . \tag{3.47}$$

Here, v_{max} denotes the maximum fluid velocity which is case specific for the considered simulation. For many hydraulic engineering type of flows featuring a given water column height H, v_{max} can be estimated according to Torricelli's law:

$$v_{max}^2 = 2gH. \tag{3.48}$$

The employed reference pressure of the classical WCSPH reads

$$B = \frac{100 v_{max}^2 \rho_0}{\gamma_T}. \tag{3.49}$$

Equation (3.43) is used throughout this thesis.

3.6 Boundary conditions

Free surface and rigid wall boundary conditions are needed for most engineering fluid dynamics applications. While free surfaces are handled by SPH without any special treatment, rigid boundaries which mimic stationary as well as moving walls demand special attention.

Three major SPH-approaches to model such boundaries can be summarized: *repulsive boundary forces, ghost particles and fixed particles*. The following section provides a brief overview of the different concepts which are illustrated in Fig. 3.6. A comprehensive description of different techniques is e.g. be given by Feldman [23].

Repulsive boundary forces

The repulsive boundary force approach [65] is based on supporting points that are located on a defined spatial boundary. Such points can be obtained e.g. from triangulations of given boundary geometries or they can be introduced as an extra class of particles within

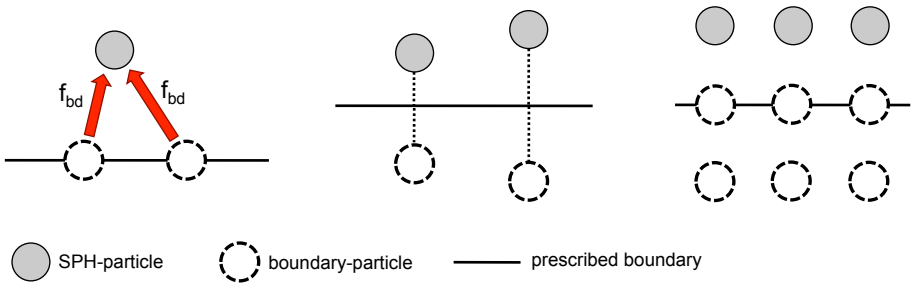

Figure 3.6: Illustration of basic boundary concepts. Left: repulsive force. Centre: ghost particles. Right: fixed particles.

the initial particle distribution process. The supporting points exert forces f_{bd} on the nearby material particles that do not follow from the standard SPH formalism and prevent them from penetrating the wall. The repulsive force usually increases with a decreasing distance between the wall and the affected SPH particles. A commonly applied force term is based on a Lennard-Jones potential which has e.g. been used by Monaghan [65] for free-surface flows. Advantages of the method are related to a wide range of force prescriptions that can be used and the fact that particles can be effectively hindered from penetrating the boundary. A disadvantage is that the SPH-particles close to the boundary will always experience a particle deficiency comparable to a free surface. Additionally, the approach requires a calibration of the applied force and viscous (no-slip) conditions are difficult to realize.

Ghost particles

By applying the ghost particle method, SPH-particles nearby a wall are mirrored and new fictitious *ghost* particles are created outside the wetted domain which carry the same properties as the source SPH-particle. These ghost particles enter the regular SPH-formalism and are treated as regular particles. Free-slip or no-slip conditions can easily be realized with this method. Free-slip is achieved by assigning the ghost particle's velocity tangentially to the boundary identical to the one of the source. Switching the direction of the tangential velocity results in a no-slip condition. The approach is very similar to the fixed particle method as noted e.g. by Souto-Iglesias et al. [94] and gives comparable results. A major difference is that boundary particles are only considered in the SPH-evaluation if they are needed. This is of special advantage for large, partly wetted domains. Difficulties arise at complex, sharply changing geometries or multiple interacting particle classes which can lead to an ambiguous boundary treatment [67]. Moreover, mirror particles are

regenerated every time step, which is not the case for fixed particles. A recently published study by Marrone et al. [57] therefore suggests to fix the particle resolution of walls and evaluate their properties at the respective mirror locations inside the wetted regime.

Fixed particles

The basic implementation of fixed particle boundaries [69] represents a simple no-slip condition. The wall is modelled by one or multiple rows of standard SPH-particles that are included in the SPH-computations during the whole simulation. The particles fill the kernel support of material particles near the wall, thus multiple rows are usually preferred. They are treated in a usual manner but their accelerations are assigned to zero. The boundary condition can easily be modified towards a free-slip condition analogous to the ghost method. It it also very simple to prescribe wall motions and accelerations if moving boundaries are of interest. A disadvantage is related to the computational effort as the particles are always included in the calculation loops. This is considered negligible for simulations in which the major part of the walls is always wetted. In this case, other drawbacks mentioned e.g. by Monaghan [67] related to spurious pressure forces due to a changing number of SPH-particles within the boundary particles' support domain are also deemed a minor problem.

SPH boundary conditions still are a subject of ongoing research. Recommendations which approach is to be preferred are strongly problem dependent. Due to its simplicity and flexibility, the fixed particle approach is used in the computations of this thesis. It shows a satisfactory performance against the background of the considered scenarios [1].

Next to velocity boundary conditions, published approaches differ in the treatment of pressure and density at the wall. Using repulsive force boundaries, the fluid particle's pressure and density follow from neighbouring particle properties within the wetted domain. Still, the pressure at the supporting wall points can be calculated from the total force at the wall over a certain reference length [67]. If ghost or fixed particles are applied, the pressure and density of fluid particles depends on neighbours within the wetted domain and the boundary particles. Ghost particles carry the properties of their corresponding mirrored fluid particles. Such properties are included into the evaluation of the governing equations for fluid particles in the vicinity of the wall. Here, pressures only depend on the properties within the wetted regime. Contrary to this, fixed wall particles carry properties

that are not only depending on the surrounding fluid particles but also on nearby wall particles.

4 Constitutive Models

The chapter describes the constitutive models that are employed for fluids, granular materials and fluid/granulate-suspensions. Since the focal applications of the thesis deal with water/soil-interaction, the fluid and granular material will subsequently be labeled as “water” and “soil” respectively. As illustrated in Fig. 4.1 four different situations should be captured by the computational models: pure water, homogeneously saturated soil, partly saturated soil and water/soil-suspension. In this work, macroscopic models are used in

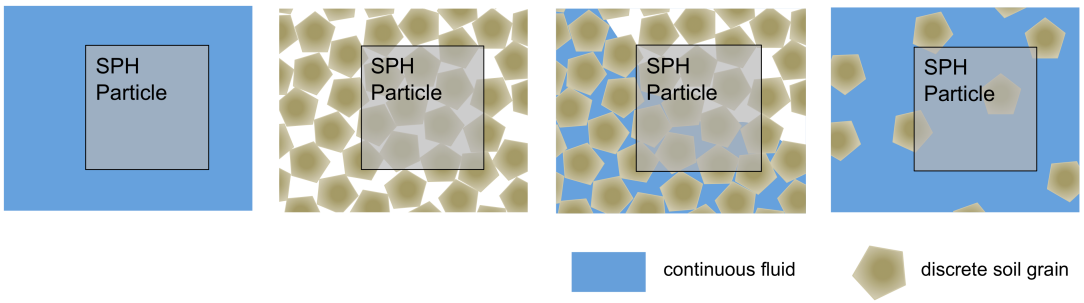

Figure 4.1: Sketch of the discretisation of water (left), homogeneously saturated soil (centre left), partly saturated soil (centre right) and water/soil-suspension (right) by an SPH particle.

which all of the four conditions are described in terms of continuous materials. This is obvious for fluids, but not necessarily for soils consisting of discrete grains. Nevertheless, macroscopic approaches are frequently applied in geotechnics. They describe the continuous soil by a constitutive model which employs a set of material specific parameters such as cohesion and the internal friction angle. Single SPH-particles thus represent a finite part of the continuum and may comprise several discrete grains as shown in Fig. 4.1.

When attention is given to the analysis of material failure induced by water/soil-interaction, two different mechanisms are of interest. Typical erosive processes dislocate parts of the soil and may therefore weaken the stability of load-bearing soil formations. Such

phenomena are usually induced by large relative motions between water and soil which yields a water/soil-suspension layer. Contrary to this, the failure of granular material is frequently caused by internal water flows through the porous soil skeleton and the associated change of soil saturation. In this case, the failure mechanism is not necessarily dominated by flow induced forces but by changing soil properties. Especially the effective material cohesion is significantly reduced for fully saturated soils. Both phenomena might interact, thus the numerical method should be able to cope with both mechanisms.

Accurate soil models [31] can become rather complicated and often require detailed knowledge about the specific soil. Rather than elaborating on the single phase model employed for the soil description the present thesis attempts to establish a reliable multi-phase/multi-continua approach. The approach can be supplemented by any more comprehensive soil description.

In the following, bold subscripts are utilised to distinguish between the water (**f**) and soil (**s**, **se**, **ses**, **sf**) phase for ambiguous properties.

4.1 Water

Water is considered to be a Newtonian fluid. Next to the isotropic pressure part that is evaluated by a state equation, the total stress tensor (2.5) consists of the deviatoric stresses $\tau_{\mathbf{f}}^{\alpha\beta}$ which depend on an isotropic dynamic viscosity $\mu_{\mathbf{f}}$ and the traceless strain-rate tensor $\dot{\epsilon}^{\alpha\beta}$

$$\tau_{\mathbf{f}}^{\alpha\beta} = 2\mu_{\mathbf{f}}\dot{\epsilon}^{\alpha\beta} \,, \tag{4.1}$$

$$\dot{\epsilon}^{\alpha\beta} = \frac{1}{2}\left[\frac{\partial v^{\beta}}{\partial x^{\alpha}} + \frac{\partial v^{\alpha}}{\partial x^{\beta}}\right] - \frac{1}{3}\left(\frac{\partial v^{\gamma}}{\partial x^{\gamma}}\right)\delta^{\alpha\beta} \,. \tag{4.2}$$

The dynamic molecular viscosity of water is assigned to $\mu_{\mathbf{f}} = 0.001$ Pa s in line with standard conditions at a reference temperature of 20° Celsius. The Large Eddy Simulation (LES) framework serves as an option to simulate turbulent flows. It uses a standard Smagorinsky model [93] to capture the unresolved sub-grid scale stresses by means of a supplementary Boussinesq-viscosity μ_t, viz.

$$\tau_{\mathbf{f}}^{\alpha\beta} = 2(\mu_{\mathbf{f}} + \mu_t)\dot{\epsilon}^{\alpha\beta} \,, \tag{4.3}$$

with

$$\mu_t = \rho\left(C_S\Delta\right)^2\sqrt{2\dot{\epsilon}^{\alpha\beta}\dot{\epsilon}^{\alpha\beta}} \,. \tag{4.4}$$

The Smagorinsky constant is assigned to common values in the range of $C_S = 0.1 - 0.2$. The filter length Δ works as a low pass filter, controlling the size of vortices that are captured by the LES model. If LES is applied to mesh based methods, the filter length is usually implicitly obtained from the cell volume. Analogous, Δ can be set equal to the smoothing length h in SPH-simulations. LES has successfully been used within SPH-frameworks by several authors (e.g. [29, 99]) and is favored in the present work due to its simplicity. Nevertheless, other approaches for turbulence modelling can be used in conjunction with SPH (in particular RANS, cf. [109]).

4.2 Soil

Regarding only small deformations, strain-rates, and relative motions, granular materials like soil are usually treated as a conventional (potentially elastic) solid that adheres to a failure criterion. This approach might not be adequate if the predictive focus is set on highly dynamic scenarios as e.g. landslides or the discharging of silos. In those cases, the soil behaves rate dependent, similar to a non-Newtownian fluid [38, 83].

In scouring simulations, both situations occur. Accordingly, the present procedure applies a combined approach that bridges between a quasi-static solid state (subsequently marked by bold subscripts **se**, **ses**) and a strain-rate driven fluid state (bold subscript **sf**). The transition between the two soil-states is managed by the magnitude of the strain-rate as suggested by Leppert [46]. The bipartite technique is not afflicted by material creeping in the limit of zero strain, a deficit that is frequently seen in conjunction with fluid-like representations of soil [54]. The linear-elastic solid state is supplemented by the von Mises yield criterion to account for the onset of plastic deformations. Exceeding the yield strength, the soil stress is gradually associated with the fluid-state. The employed yield strength is modeled in line with the Mohr-Coulomb theory which can be casted into the viscosity of a non-Newtonian fluid. Both branches of the model, i. e. the solid or the fluid state, can be separately used if needed.

To account for partly saturated soils, a simple Darcy-approach outlined by Lenaerts [45] is adopted to model the seepage flow through porous media. The model does not require additional fluid particles to represent the pore water flow. The latter offers an enhanced computational efficiency over alternative strategies [11]. The corresponding flow through the soil skeleton is evaluated with respect to material properties such as

capillarity, porosity, gravity and pressures. A variable soil cohesion which depends on the soil particles' saturation is used to account for changing material strengths.

4.2.1 Yield criterion

The soil model is based on a combined Mohr-Coulomb and von Mises yield criterion. Despite its relative simplicity, the adopted criterion is suitable to capture the basic soil behaviour which is primarily governed by the internal friction angle ϕ and the cohesion C of the granular soil. Figure 4.2 depicts a general (2D) illustration of the soil's stress state by means of Mohr's circle with the two principal stresses $\hat{\sigma}_1$ and $\hat{\sigma}_2$.

According to the Mohr-Coulomb criterion, the material failure commences if the shear stress magnitude exceeds a maximum value

$$\tau = \hat{\sigma}\tan\phi + C \tag{4.5}$$

with the normal stress $\hat{\sigma}$. Equation (4.5) is represented by the yield line in Fig. 4.2. In the present study, the mean principle stress $\hat{\sigma}_m$, which marks the stress circle's midpoint, follows from the pressure, i.e. $\hat{\sigma}_m = p$. The radius of the circle is defined by the maximum attainable shear stress τ_{yield}. No shear stresses τ will occur above the yield line, hence the yield line needs to be tangent to the circle. As outlined in Fig. 4.2, the radius of the circle can be calculated by a cohesion part τ_{m1} and a mean principle stress part τ_{m2}

$$\tau_{yield} = \tau_{m1} + \tau_{m2} \ , \tag{4.6}$$

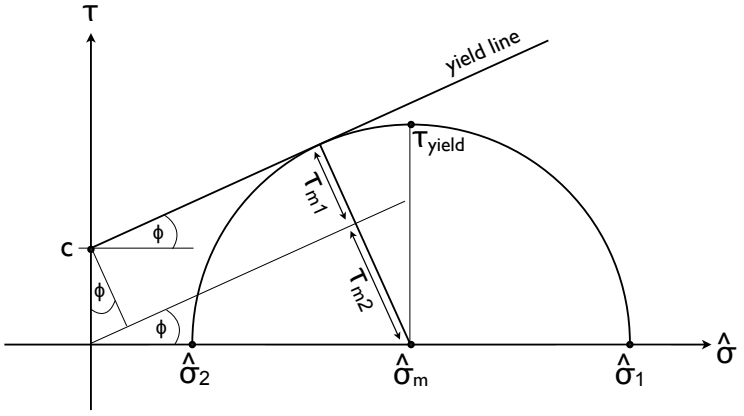

Figure 4.2: Mohr's circle with Coulomb yield line.

with

$$\tau_{m1} = C \cdot \cos\phi \quad \text{and} \quad \tau_{m2} = \hat{\sigma}_m \cdot \sin\phi = p \cdot \sin\phi \; . \tag{4.7}$$

The Mohr-Coulomb criterion can therefore be rewritten as

$$\tau_{yield} = C \cdot \cos\phi + p \cdot \sin\phi \; . \tag{4.8}$$

In line with the von Mises criterion, yielding requires the second invariant J_2 of the deviatoric shear stress tensor $\tau^{\alpha\beta}$ to exceed the threshold value τ^2_{yield}, i.e.

$$J_2\left(\tau^{\alpha\beta}\right) = \frac{\tau^{\alpha\beta}\tau^{\alpha\beta}}{2} \geq \tau^2_{yield} \; . \tag{4.9}$$

Following von Mises [110], the deviatoric stresses are restricted (or re-scaled) to the elastic limit in order to comply with Eq. (4.9).

4.2.2 Elastic solid state

An isotropic linear-elastic behaviour that obeys the previously described yielding conditions is assumed for the solid state of the soil. Accordingly, the deviatoric stresses $\tau^{\alpha\beta}$ are evaluated in line with well-known elastic relations, viz.

$$\dot{\tau}^{\alpha\beta} = \frac{E}{1+\nu}\dot{\epsilon}^{\alpha\beta} \; , \tag{4.10}$$

where E denotes Young's modulus and ν refers to the Poisson ratio. The traceless shear rate is given by Eq. (4.2).

When attention is directed to large deformations, a stress rate that is invariant with respect to rigid-body rotation must be employed. To obtain a material frame indifferent formulation, Eq. (4.10) is replaced by the Jaumann stress rate

$$\dot{\tau}^{\alpha\beta} = \frac{E}{1+\nu}\dot{\epsilon}^{\alpha\beta} + \tau^{\alpha\gamma}\dot{\omega}^{\gamma\beta} - \dot{\omega}^{\alpha\gamma}\tau^{\gamma\beta} \; , \tag{4.11}$$

where $\dot{\omega}^{\alpha\beta}$ denotes the rotation-rate tensor

$$\dot{\omega}^{\alpha\beta} = \frac{1}{2}\left(\frac{\partial v^\beta}{\partial x^\alpha} - \frac{\partial v^\alpha}{\partial x^\beta}\right) \; . \tag{4.12}$$

The final form of the adopted deviatoric stresses reads

$$\tau^{\alpha\beta}_{\mathsf{se}} = \frac{E}{1+\nu}\epsilon^{\alpha\beta} + \left(\mathcal{J}^{\alpha\beta} - \frac{1}{3}\mathcal{J}^{\gamma\gamma}\delta^{\alpha\beta}\right) \; . \tag{4.13}$$

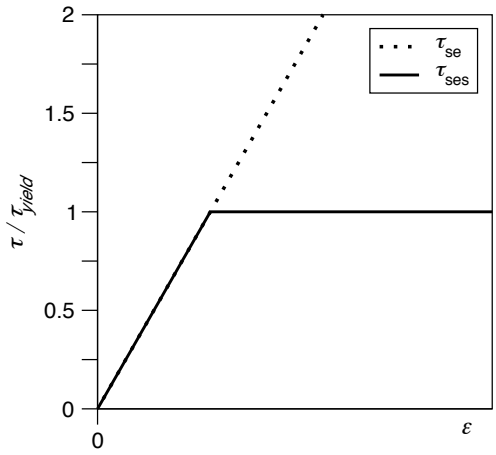

Figure 4.3: Plot of elastic stress magnitudes.

The Jaumann terms $\mathcal{J}^{\alpha\beta}$ follow from an explicit time integration of the previous stress and rotation-rate tensors (indicated by an overbar). Similarly, the shear tensor $\epsilon^{\alpha\beta}$ can be obtained by integrating the strain-rate tensor $\dot{\epsilon}^{\alpha\beta}$ in time

$$\frac{d\mathcal{J}^{\alpha\beta}}{dt} = \overline{\dot{\omega}^{\alpha\gamma}}\,\overline{\tau_{\mathbf{se}}^{\gamma\beta}} - \overline{\tau_{\mathbf{se}}^{\alpha\gamma}\dot{\omega}^{\gamma\beta}}\;, \quad \frac{\epsilon^{\alpha\beta}}{dt} = \overline{\dot{\epsilon}^{\alpha\beta}}\;. \tag{4.14}$$

The stresses following from Eq. (4.13) are re-scaled to maintain the von Mises yield criterion (4.9) as illustrated in Fig. 4.3:

$$\tau_{\mathbf{ses}}^{\alpha\beta} = \begin{cases} \tau_{\mathbf{se}}^{\alpha\beta} & \text{if} \quad R_{vm} \geq 1 \\ \tau_{\mathbf{se}}^{\alpha\beta}\sqrt{R_{vm}} & \text{if} \quad R_{vm} < 1 \end{cases}, \tag{4.15}$$

with the ratio R_{vm}

$$R_{vm} = \frac{\tau_{yield}^2}{J_2\left(\tau_{\mathbf{se}}^{\alpha\beta}\right)}\;. \tag{4.16}$$

4.2.3 Viscoplastic fluid state

Exceeding the yield strength, plastic deformations occur and the granular soil is assumed to behave rate-dependent like a non-Newtonian fluid. To this effect, the deviatoric stresses $\tau_{\mathbf{sf}}^{\alpha\beta}$ are composed from an apparent, inhomogeneous isotropic soil viscosity $\mu_{\mathbf{s}}$ and a strain-rate tensor (4.2)

$$\tau_{\mathbf{sf}}^{\alpha\beta} = 2\,\mu_{\mathbf{s}}\;\dot{\epsilon}^{\alpha\beta}\;. \tag{4.17}$$

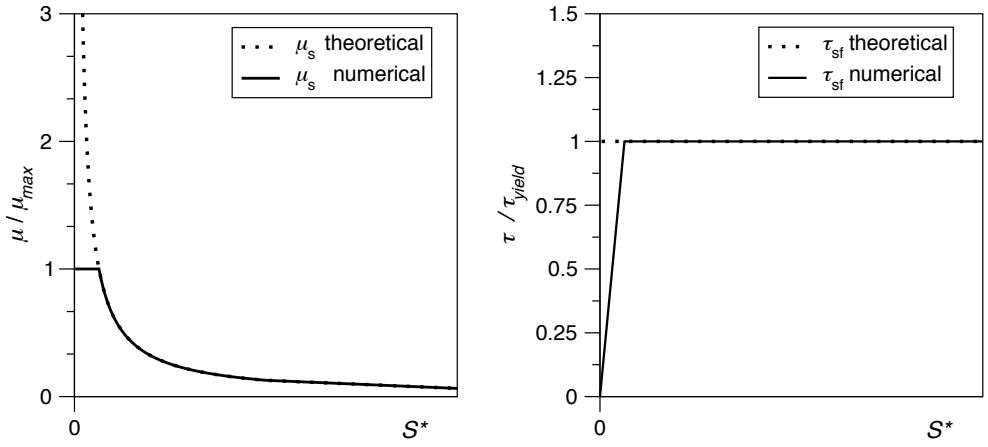

Figure 4.4: Numerical and theoretical soil viscosity and shear stress vs. strain-rate.

The deviatoric stresses $\tau_{\mathbf{sf}}^{\alpha\beta}$ are supposed to take over from the scaled elastic stresses $\tau_{\mathbf{ses}}^{\alpha\beta}$ and also have to satisfy the von Mises relation $J_2\left(\tau_{\mathbf{sf}}^{\alpha\beta}\right) = \tau_{yield}^2$. The latter yields

$$\mu_{\mathbf{s}} = \frac{C \cdot \cos\phi + p \cdot \sin\phi}{S^*} \,, \tag{4.18}$$

with $S^* = \sqrt{4\, J_2\left(\dot{\epsilon}^{\alpha\beta}\right)}$. Expression (4.18) becomes singular when the strain-rate invariant S^* vanishes as depicted in Fig. 4.4. Therefore, an upper viscosity limit μ_{max} is often introduced to avoid numerical instabilities

$$\mu_{\mathbf{s}} = \min\left(\frac{C \cdot \cos\phi + p \cdot \sin\phi}{S^*}, \mu_{max}\right) \,. \tag{4.19}$$

The choice of μ_{max} plays a decisive role for approaches that solely employ a viscoplastic model (4.19) for the granular soil. Due to the lack of memory effects, such models are prone to substantial amounts of spurious creeping when the strain-rate invariant S^* vanishes if the threshold viscosity μ_{max} is not chosen high enough. In these cases, the stresses significantly drop below the yield stress as shown in Fig. 4.4.

Related improvements have been outlined by Manenti et al. [54]. Accordingly, soil particles are fixed, i.e. the acceleration and the velocities are assigned to zero, if the soil viscosity exceeds the threshold value. Although this limited viscoplastic approach still employs a case-dependent threshold viscosity, it can suppress soil creeping much better and seems more appropriate for long-term simulations. On the contrary, particle freezing

can be inappropriate for suspended particles or significantly imbalanced body or pressure forces.

4.2.4 Combined solid/fluid approach

An efficient combination of elastic and viscoplastic stress models for the deforming granular soil has been reported by Leppert [46]. A similar strategy is applied in the present study. The technique blends between the two baseline approaches in the plastic regime where they feature the same stress level (Fig. 4.5).

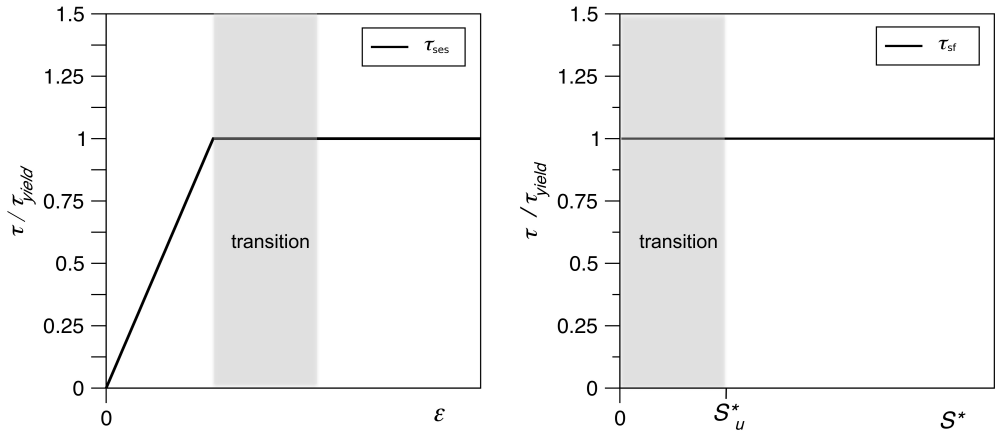

Figure 4.5: Elastic and fluidic soil stresses with transition zones for the combined solid/fluid approach.

The blending function is obtained from a normalised strain rate. For small strain rates, the fluid state is deactivated and the deviatoric stresses follow their solid-state definition. Since the viscoplastic stresses are only active for non-negligible strain rates, the singularity of (4.18) at $S^* \to 0$ is almost unnoticed. Therefore, no careful artificial limitation of the apparent soil viscosity is needed, nor need particles that exceed such a maximum viscosity be spatially fixed to avoid creeping. When the elastic stresses exceed the yield criterion (4.8), the actual solid stresses $\tau_{\mathbf{s}}^{\alpha\beta}$ are computed from the expression

$$\tau_{\mathbf{s}}^{\alpha\beta} = (1-\zeta)\tau_{\mathbf{ses}}^{\alpha\beta} + \zeta\tau_{\mathbf{sf}}^{\alpha\beta} \; . \tag{4.20}$$

applying a blending function ζ. Otherwise, the material is considered as an elastic solid as described in section 4.2.2:

$$\zeta = 0 \quad \text{if} \quad R_{vm} > 1 \; . \tag{4.21}$$

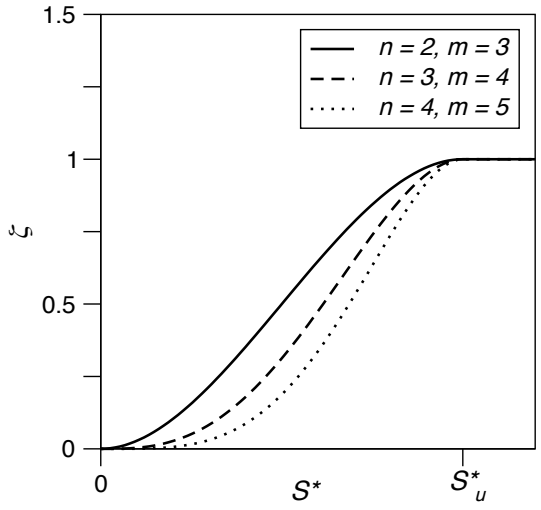

Figure 4.6: Blending function for soil stresses.

The transition to the fluid state is associated with an upper strain-rate limit S_u^*. A viable definition of S_u^* is given by

$$S_u^* = \frac{\tau_{yield}}{\mu_{max}} \,. \tag{4.22}$$

Note that here, μ_{max} represents an auxiliary quantity and that the applied soil viscosity is not scaled. In case the strain-rates exceed the upper limit, the material is treated as a granular fluid

$$\zeta = 1 \quad \text{if} \quad S^* \geq S_u^* \,. \tag{4.23}$$

The present work adopts a polynomial blending function which features zero gradients at the respective ends

$$\zeta = m \left(\frac{S^*}{S_u^*} \right)^n - n \left(\frac{S^*}{S_u^*} \right)^m \tag{4.24}$$

with the exponents $n > 1$ and $m = n + 1$. The blending behaviour of Eq. (4.24) can be adjusted by the variable exponents as illustrated in Fig. 4.6. In the present work, $n = 2$ has successfully been used, but other exponents might be of advantage for special applications.

4.2.5 Partly saturated soil

The yield criterion and the related fluid-state model employ a cohesion parameter. A constant cohesion value is deemed realistic for a homogeneous, time-invariant soil saturation Ψ. In general, the utilized cohesion value C can vary in space and time according to the variation of the saturation. The effective cohesion of granular materials is based on

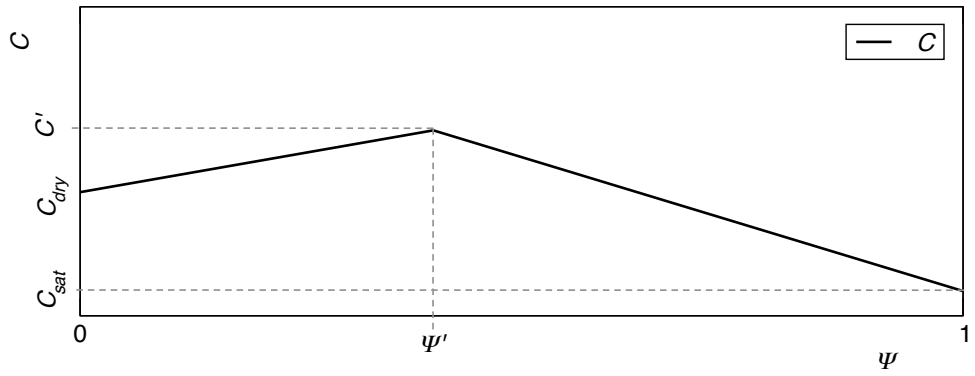

Figure 4.7: Pore water saturation depending effective soil cohesion.

capillary effects within the grain structure and the maximum cohesion C' often occurs for an intermediate saturation Ψ'. This maximum value is usually significantly larger than the values C_{dry} and C_{sat} for dry ($\Psi = 0$) and completely saturated ($\Psi = 1$) material. In the present study, cohesion values for partly saturated soil are obtained from a piecewise linear interpolation between $\Psi = [0, \Psi', 1]$ as illustrated in Fig. 4.7

$$C = \begin{cases} C_{dry} + \frac{C' - C_{dry}}{\Psi'} \Psi & \text{if } \Psi \leq \Psi' \\ C' + \frac{C_{sat} - C'}{1 - \Psi'} (\Psi - \Psi') & \text{if } \Psi > \Psi' \, . \end{cases} \tag{4.25}$$

The particle's saturation is computed from the fluid density $\rho_{\mathbf{f}}$, the porosity φ and an additional pore water mass $m_{\mathbf{p}}$ representing the fluid nested inside the soil skeleton

$$\Psi = \frac{m_{\mathbf{p}}}{\rho_{\mathbf{f}} \, \varphi \, V} \, . \tag{4.26}$$

Following a macroscopic approach, the SPH-represention of the soil is supplemented by two spatially varying particle properties, i.e. porosity φ and permeability K. For a given porosity, the pore-water mass adheres to the restriction $m_{\mathbf{p}} \leq \rho_{\mathbf{f}} \, \varphi \, V$. Different options are conceivable to determine $m_{\mathbf{p}}$. Bui et al. [14] propose to use a set of "background" fluid particles to resolve the water flow through the porous media. On the contrary, the present work is borrowed from a diffusive Eulerian description of the pore water flow presented by Lenaerts [45] that is based on a Darcy approach. An advantage of this formulation consists of the fact that no additional particles are needed which reduces the computational surplus.

The change of pore water mass is described in terms of a diffusion process. The corre-

sponding governing equation reads

$$\frac{\partial m_{\mathbf{p}}}{\partial t} = \nabla^{\beta} \left(d \nabla^{\beta} m_{\mathbf{p}} \right) \tag{4.27}$$

and employs a variable scalar diffusion coefficient d

$$d = \left(v_{\mathbf{p}}^{\alpha} \Delta_{p}^{\alpha} \right) \Psi^{\beta_{\mathbf{p}}} \tag{4.28}$$

which depends on the particle spacing vector Δ_{p}^{α}, the saturation Ψ and a pore water velocity $v_{\mathbf{p}}^{\alpha}$. The strength of the diffusion coefficient can be controlled by the exponent $\beta_{\mathbf{p}} > 0$. Recommended values [45] relate to $\beta_{\mathbf{p}} = 7$. The pore water mass $m_{\mathbf{p}}$ can now be evaluated by integrating Eq. (4.27) in time.

The pore water velocity in Eq. (4.28) is obtained from the generalized Darcy's law describing the flux inside a porous medium as a function of pressure gradients, the gravity vector g^{α}, and three scalar material properties, i. e. permeability K, porosity φ and fluid viscosity $\mu_{\mathbf{f}}$:

$$v_{\mathbf{p}}^{\alpha} = -\frac{K}{\varphi \mu_{\mathbf{f}}} \left(\nabla^{\alpha} p_{\mathbf{p}} - \nabla^{\alpha} p_{cap} - \rho_{\mathbf{f}} g^{\alpha} \right) \tag{4.29}$$

An estimation of the pore water pressure can be evaluated using a modified state equation which relates the pore water pressures to the soil pressure. The corresponding modification of Tait's equation that has been also used by Lenaerts reads

$$p_{\mathbf{p}i} = B_{\mathbf{p}} \Psi_i \left(\left(\frac{\rho_{\mathbf{s}i}}{\rho_{\mathbf{s}0}} \right)^{7} - 1 \right) , \tag{4.30}$$

with the reference pressure $B_{\mathbf{p}}$, soil particle density $\rho_{\mathbf{s}}$ and initial soil particle density $\rho_{\mathbf{s}0}$. Equation (4.30) leads to rather inaccurate pore pressures if the porous material is not completely submerged. This issue can be pointed out as the main disadvantage of methods solely based on soil particles as compared to approaches with an extra set of water particles. Still, the problem can be overcome by evaluating the pore pressure by case-specific analytical expressions.

The capillary pressure p_{cap} accounts for micro-fluidic effects inside the pores. It can be calculated as a function of the saturation:

$$p_{cap} = B_{cap} \left(1 - \Psi \right)^{\alpha_{cap}} \tag{4.31}$$

Here, B_{cap} refers to a reference pressure and the exponent α_{cap} controls the strength of the capillary potential with $0 < \alpha_{cap} < 1$.

The interaction between porous soil and water particles is realized by assigning a fixed maximum saturation $\Psi_i = 1$ to the water particles. For these particles, the pore water mass matches the total particle mass $m_{\mathbf{p}i} = m_i$. In this work, the fluid diffusion does not cause a change of the initial fluid particles' masses and is therefore not conservative. Note, that the approach could however be extended by absorption and emission models if needed [45].

4.3 Water/soil suspension

The constitutive soil model is supplemented by a suspension treatment to capture the viscosity transition along the water/soil interface. Accordingly, the suspension is assumed to be in the grain collisional regime where experiments [2] and predictions [37] indicate a quadratic, turbulent-like relation between the shear stress and the velocity in the limit of a vanishing suspension layer thickness [18]. Particles which feature a fluid behaviour and reside inside a fictitious suspension layer along the upper side of the interface are assigned to a viscosity that is derived from a Chézy-relation (subscript c) along a route outlined by Fraccarollo and Capart [25]. In practice, the shear-stress magnitude of the suspension is assumed to adhere to

$$\tau_c^* = \rho_{\mathbf{s}}\, C_f\ (v^\alpha v^\alpha)\ . \tag{4.32}$$

In accord with the viscoplastic soil model, Eq. (4.32) is used to determine a corresponding isotropic Chézy-viscosity

$$\mu_c = \frac{\rho_{\mathbf{s}}\, C_f\ (v^\alpha v^\alpha)}{S^*}\ . \tag{4.33}$$

In (4.32) and (4.33) the soil density is denoted by $\rho_{\mathbf{s}}$ and C_f refers to an empirical friction coefficient. Fraccarollo and Capart [25] recommend C_f-values between 0.007 - 0.03. In the present work, an intermediate value of $C_f = 0.01$ is applied. As outlined by Ulrich and Rung [102] the specific choice for C_f within these bounds is not that influential. The identification of the suspension layer and the associated viscosity transition are controlled by the local soil concentration $\tilde{c}_{\mathbf{s}}$ inside the kernel support.

To bridge between soil, suspension and fluid viscosity, three different regimes are distinguished (Fig. 4.8). Following Nnadi and Wilson [74], the Chézy-viscosity μ_c is imposed

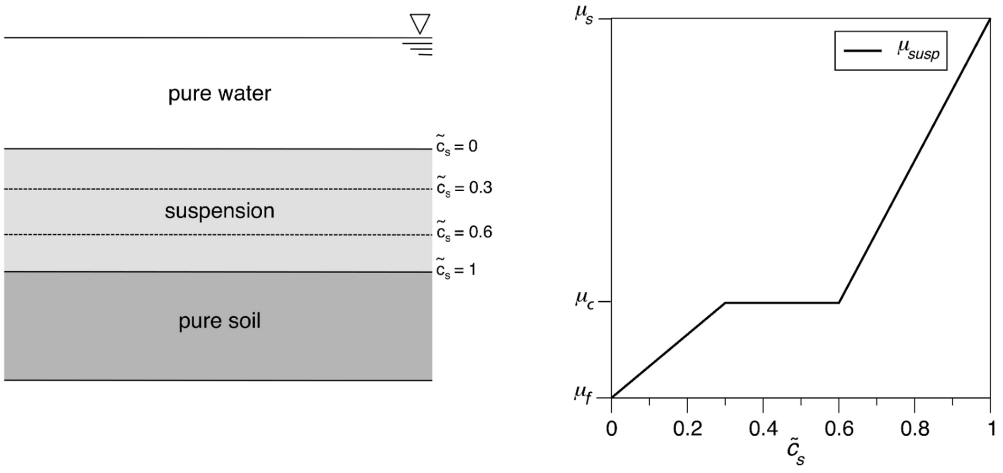

Figure 4.8: Left picture: sketch of the different suspension zones. Right picture: corresponding qualitative plot of the viscosities.

in the region $0.3 < \tilde{c}_\mathbf{s} < 0.6$. Piecewise linear interpolations between μ_c and the liquid- or solid-phase viscosities are applied in the transition zones (cf. Fig. 4.8)

$$\mu_{susp} = \begin{cases} \mu_\mathbf{f} + \frac{\mu_c - \mu_\mathbf{f}}{0.3}\tilde{c}_\mathbf{s} & \text{if} \quad \tilde{c}_\mathbf{s} \leq 0.3\,, \\ \mu_c & \text{if} \quad 0.3 < \tilde{c}_\mathbf{s} < 0.6 \\ \mu_c + \frac{\mu_\mathbf{s} - \mu_c}{(1-0.6)}(\tilde{c}_\mathbf{s} - 0.6) & \text{if} \quad 0.99 \geq \tilde{c}_\mathbf{s} \geq 0.6\,. \end{cases} \tag{4.34}$$

The suspension viscosity is confined by μ_{max}

$$\mu^*_{susp} = \begin{cases} \mu_{susp} & \text{if} \quad \mu_{susp} < \mu_{max} \\ \mu_{max} & \text{if} \quad \mu_{susp} \geq \mu_{max}\,. \end{cases} \tag{4.35}$$

The suspension treatment should not be applied to soil particles which are submerged in the soil phase. An application inside the soil regime is inhibited by the definition of an appropriate thereshold value for the local soil concentration, i.e. $\tilde{c}_\mathbf{s} < 0.99$. For particles with $\tilde{c}_\mathbf{s} < 0.99$ the deviatoric stresses follow from the suspension treatment, otherwise they are computed inline with the soil expression (4.20).

5 Self Propelled Ships

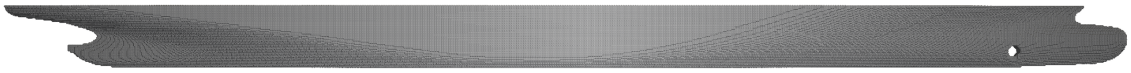

Figure 5.1: Particle discretisation of a container vessel's underwater hull.

This chapter outlines relevant approaches to mimic vessel motions and the impact of propulsion and manoeuvring devices which represent key features in the overall simulation of ship induced scours.

In the present work, the ship is considered to be a rigid body and its motions are evaluated by an external six degrees of freedom (6DOF) motion solver. Propellers and thrusters are not geometrically resolved but represented by appropriate body force models adopting a frequently employed approach for complex ship manoeuvring predictions.

5.1 6DOF motion solver

Ship motions can be captured by a 6DOF motion solver for freely floating rigid bodies. The present SPH code applies an external 6DOF module developed by Koliha [39] that is based on a unit quaternion formulation of the rotational body motions. The advantage of such approaches arise from the avoidance of the gimbal lock associated with Euler angles. Therefore, no restriction for the rotational motion exists making GADGET-$^{\mathrm{H}}2^{\mathrm{O}}$ capable of being applied to any kind of body movements [73].

Floating bodies are discretised by an extra set of particles. These particles hold the same properties as fluid particles despite their rigid alignment to the motion of the bodies' centre of gravity. They can be compared to the fixed wall boundary particles described in section 3.6. All forces acting on the single particles are collected to represent an integral force and moment evaluated at the floating body's centre of gravity x^{α}_{FB}. The summation

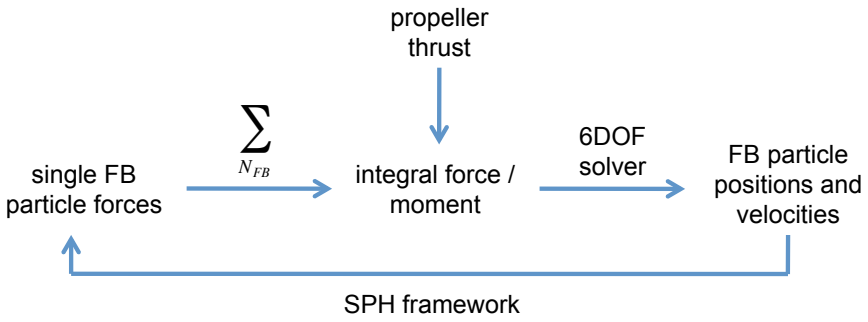

Figure 5.2: Schematic outline of the 6DOF ship motion evaluation.

of forces simply reads

$$f_{FB}^{\alpha} = \sum_{i=1}^{N_{FB}} f_i^{\alpha} \ , \tag{5.1}$$

with the total number of particles N_{FB} representing the floating body and the respective particle forces f_i^{α}. Gravitational influences are considered by the motion module itself, therefore, f_i^{α} is restricted to surface forces – i.e. pressure, shear-stress – and body forces from propulsor models. The integral moment t_{FB}^{α} is obtained with regard to the single particles' positions relative to the body's centre of gravity

$$t_{FB}^{\alpha} = \sum_{i=1}^{N_{FB}} \epsilon^{\alpha\beta\gamma} \ (x_i^{\alpha} - x_{FB}^{\alpha}) \ f_i^{\gamma} \ , \tag{5.2}$$

where $\epsilon^{\alpha\beta\gamma}$ refers to the permutation tensor.

The load components f_{FB}^{α} and t_{FB}^{α} are passed to the motion solver module which determines the body's new velocity, position and orientation. Rotations are evaluated in the afore mentioned quaternion representation. According to the rotation theorem of Euler, a coordinate transformation is given by a single rotation around an appropriate axis [28]. A transformation can thus be described using four parameters, i.e. three coordinates of the rotation axis n_{FB} and the angle φ_{FB}. These four Euler parameters

$$e^0 = \cos\left(\frac{\varphi_{FB}}{2}\right), \quad e^{\alpha} = \begin{pmatrix} e^1 & e^2 & e^3 \end{pmatrix}^T = n_{FB} \sin\left(\frac{\varphi_{FB}}{2}\right) \tag{5.3}$$

define a unit quaternion in the scalar-vector formulation (e^o, e^{α}).

Body particle properties are updated after passing back the new rigid body motion to the SPH solver. The particles reenter the regular SPH procedure except for the part of integrating their accelerations (or forces, respectively) to velocities and positions. The

whole cycle is illustrated in Fig. 5.2. Pressures and densities are evaluated by accounting for participations of fluid particles as well as floating body particles analogue to fixed wall particles (3.6).

5.2 Body force propulsor models

Resolving the geometries of propellers or other propulsive devices requires very fine particle resolutions far below the typical particle descretisations applied in the present work. A reasonable resolution for a full-scale ship hull geometry lies in the range of 0.1-0.5 m particle spacing while propeller blades do not feature thicknesses of more than a few centimeters. Therefore, a direct modeling approach is not further investigated. Instead, propulsion and active manoeuvring devices are approximated by appropriate body force models that mimic the required force contributions.

5.2.1 Propeller

Ship propellers are simulated by using a radial distribution of body forces along a route outlined by Stern et al. [97]. The formulation used in the present work represents an SPH adaption of Xing-Kaeding's [112] body force model for RANS based VoF procedures which has successfully been applied to different complex ship manoeuvre predictions [56, 41].

The propeller is idealized as a cylindrical actuator disc with a certain thickness Δx_p which is illustrated in Fig. 5.3. Δx_p spans several rows (5 - 10) of particles. The radial dimensions of the disc are restricted by the propeller's outer radius r_p and r_h, the radius of the propeller hub. Axial and tangential body forces b_x and b_ϕ, respectively, are applied to each particle which resides inside this hollow cylinder. Following Stern et al. [97], the radial circulation distribution is a function of the radial distance from the hub r_D

$$r' = \frac{r_D - r_h}{r_p - r_h}\sqrt{1 - \frac{r_D - r_h}{r_p - r_h}} \; . \tag{5.4}$$

Equation (5.4) is non-zero only if $r_h < r_D < r_p$. The integral thrust T and torque Q of the propeller are equal to the sums of all individual contributions b_x and $b_\phi r_D$ of all particles inside the disc regime. The discrete forces applied to the single particles therefore become

$$b_x(r') = \frac{1}{\sum\limits_{N_{pp}}(r')} r' T_p \; , \tag{5.5}$$

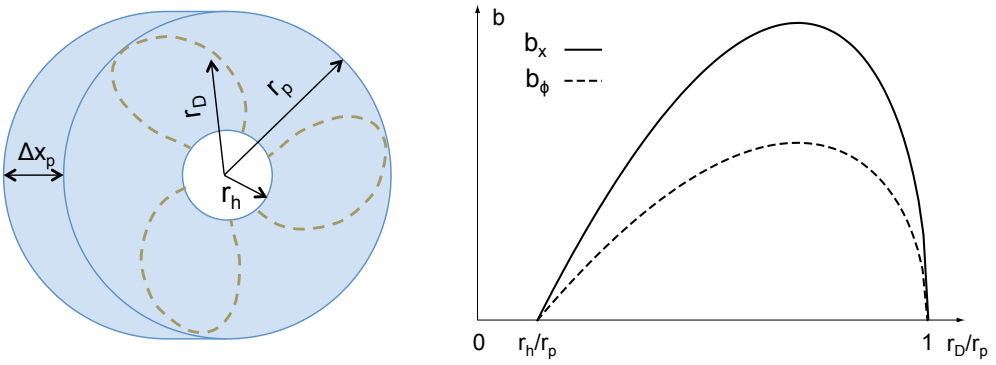

Figure 5.3: The left picture shows the propeller approximation by an actuator disc. Body force distributions over the propeller radius are plotted in the right picture (modified picture from [112]).

$$b_\phi(r') = \frac{1}{\sum\limits_{N_{pp}} (r' r_D)} r' Q_p \ , \tag{5.6}$$

where N_{pp} represents the number of particles that reside inside the propeller disc regime. The employed radial body force distributions are illustrated in the right picture of Fig. 5.3. The integral thrust T_p and torque Q_p follow from linearized open-water characteristics

$$T_p = (c_{T1} - c_{T2} J) \rho n_p^2 D_p^4 \ , \tag{5.7}$$

$$Q_p = (c_{Q1} - c_{Q2} J) \rho n_p^2 D_p^5 \tag{5.8}$$

with the advance coefficient

$$J = v_a / (n_p D_p) \ , \tag{5.9}$$

the propeller's mean axial inflow velocity v_a, rotation rate n_p and propeller diameter D_p. The constants c_{T1}, c_{T2}, c_{Q1}, c_{Q2} can be chosen to give a close fit to open water propeller diagrams. Such diagrams do only account for homogeneous approach flow conditions. Mind that the propeller approach velocity v_a is generally not known but can be determined in an iterative procedure.

For the simulation of harbour manoeuvres, the ship velocities will be rather small or even zero if the vessel is initially at rest which is frequently called bollard pull condition. For the sake of simplicity, the propeller inflow velocity v_a is assigned to the ship's axial velocity v_{sx}. This implies that the propeller delivers its maximum thrust and torque if the

ship is not moving forward. An acceleration of the ship is achieved by imposing additional axial body forces to particles discretising the ship hull, hence

$$b_{sx} = T_p / N_{sp} \ , \tag{5.10}$$

with the total number of hull particles N_{sp}. Mind that the hull forces resulting from Eq. (5.10) need to be applied in the opposite direction than the fluid forces (Eq. (5.5)). The present work does not consider propeller induced side forces and the effect of the propeller torque on the ship is deemed negligible.

5.2.2 Transverse thruster

The afore described propeller model is not applicable to ducted transverse thrusters. Thruster tunnels are of rather small diameter which leads to a relatively rough resolution of the enclosed fluid. In that case, especially the rotational motions will not correctly be captured which can result in significant inaccuracies of the overall flow prediction. A simple body force model that does not consider angular accelerations is presented in the following. As illustrated in Fig. 5.4, the propulsor is modeled by an actuator disc with a extension Δy (3-5 rows of particles) in line with the ship's lateral axis. Radial restrictions are given by the shape of the thruster tunnel which does not necessarily need to be of cylindrical shape. Body forces applied to the fluid particles within the actuator disc are derived from a thruster jet model presented by Brix [10].

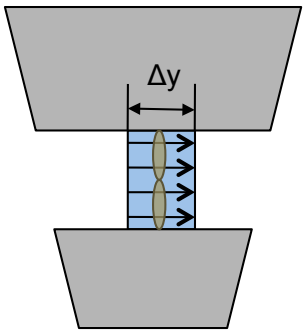

Figure 5.4: Transverse thruster approximation by an actuator disc embedded into an idealized ship frame.

According to Brix [10], the thruster's jet velocity v_t can be approximated by a simple momentum theory

$$v_t = \sqrt[3]{\frac{2P_t}{\rho A_t}}, \tag{5.11}$$

with the fluid density ρ, thruster's power P_t and cross-sectional area A_t. The thrust T_t is related to the power and jet velocity

$$T_t = \frac{2P_t}{v_t} \ . \tag{5.12}$$

Body forces b_y that are needed to accelerate each thruster particle to the desired jet velocity v_t are derived from a relative particle velocity and the simulation's time step

$$b_y = V_i \rho_i (v_i - v_t)/\Delta t \ , \tag{5.13}$$

with the particle velocity v_i and the time step Δt. The ship hull is accelerated by lateral body forces applied to hull particles:

$$b_{sy} = T_t / N_{st} \ . \tag{5.14}$$

with the number of considered hull particles N_{st}. Equation (5.14) should only be applied to those particles located in the vicinity of the thruster to account for induced rotational hull motions. In terms of global coordinates, the forces applied to the hull and the fluid are of opposite orientation.

6 Variable Particle Resolution

An efficient variable particle resolution is a key feature if full-scale marine engineering problems have to be simulated. The computational costs associated to homogeneous resolution strategies in large scale applications are often prohibitive. Since practical applications are frequently concerned with the analysis of subtle details in a confined region which is embedded in a large physical domain, variable resolution techniques - next to code-parallelisation - are a viable attempt to enhance the industrial applicability of SPH. The restriction to homogeneous isotropic resolutions is quite significant and denotes an important drawback of SPH when compared with mesh based methods.

In the field of port hydrodynamic problems, e.g. the subregions around vessel propulsion devices require a rather fine resolution while large parts of harbour basins need to be covered within the simulation but can be treated by a much coarser particle resolution. This way, the total number of particles and the corresponding computational effort can significantly be reduced compared to uniform particle spacings which are defined by the smallest resolution needed.

Most problems related to variable SPH-resolutions are due to the method's Lagrangian formulation. Compared e.g. to Eulerian mesh-based CFD methods, this makes it quite challenging to develop efficient, conservative and numerically stable variable resolution schemes. The chapter provides a brief overview of state of the art techniques. Subsequently, a new strategy is described which is based on a fixed amount of particles with dynamically changing properties.

6.1 State of the art techniques

Basically, two different approaches are applied in state of the art SPH-simulations to adjust the number of particles to the importance of subdomains (variable resolution) and/or local

physics (dynamic resolution).

An evident simple technique is based on initialising the simulation with an inhomogeneous particle distribution and retain the initial particle properties during the simulation, as shown e.g. by Omidvar et al. [76]. The method is suitable for simulations with moderate, confined particle displacements where particles stay within their initial region. A disadvantage of such a fixed masses approach is the rigid alignment to the initial particle configuration. The resolution is not adjusted to the simulation dynamics and might be inappropriate at a later stage. Moreover, as illustrated in Fig. 6.1 “large” particles can penetrate into “small-particle” regions (and vice versa) when large motions occur, which can cause inaccuracies or even numerical instabilities.

Figure 6.1: Lagrangian variable resolution (fixed masses). Initial (left) and subsequent (right) particle distribution: small particles can penetrate into a large particle region.

As opposed to the above mentioned Lagrangian variable-resolution approach, Eulerian approaches to variable and dynamic resolution exist. Feldman [23] has outlined a dynamic-resolution strategy in which “old particles” are split into “new particles”. The properties and the location of the new particles need to be initialised in compliance with the conservation of mass and momentum. The refinement follows the simulation dynamics and is not restricted to small deviations from the initial scenario. An extension of this method has been presented by Vacondio et al. [104] which allows the merging of particles to overcome the problem of increasing numbers of total particles during the simulation. It has successfully been applied to shallow water equation in full scale scenarios. The approach is, however, related to rather difficult coalescing algorithms that may counteract the improvement of computational efficiency, especially if the focus is shifted towards three dimensional applications.

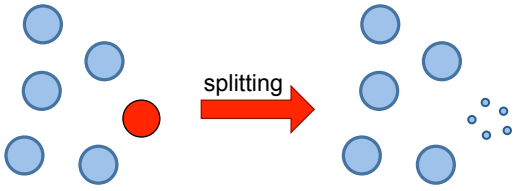

Figure 6.2: Splitting technique: single particles are split into a set of new particles.

6.2 Variable particle-mass approach

In the present work, an efficient variable-resolution strategy is persued. The key-feature is to assign the particle mass m and kernel length h to a prescribed spacing Δ_p of Eulerian subregions that are defined with respect to global coordinates. The properties are not aligned to the initial position of the particle (Lagrangian approach) but possibly vary in line with the actual position x^α (Eulerian approach). The approach is not truly dynamic, as the resolution is governed by the location of a particle and not the local dynamics. The strategy is therefore labeled Eulerian variable-resolution technique. Accordingly, regions with an analytically described, zonal gradient of the (initial) spacing Δ_p are defined in a preprocessing step. To provide smooth variations, constant gradients $\nabla(\Delta_p)$ are employed.

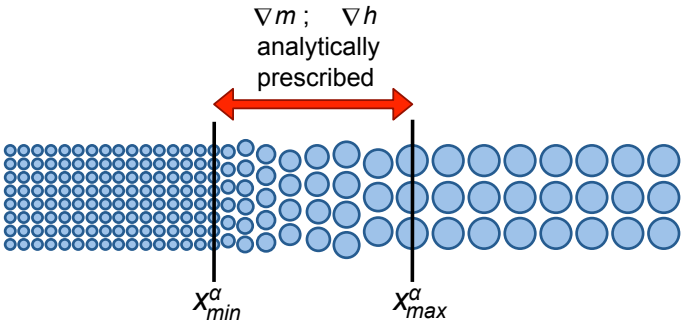

Figure 6.3: Sketch of the basic mechanism of the variable resolution strategy. In the illustrated example, a linear transition bridges between particles of large masses and those of lower masses. The mass gradient as well as the corresponding gradient of the smoothing length are analytically prescribed in relation to global reference coordinates.

The gradients of the particle spacing, mass and kernel length are linked by

$$\nabla^\alpha h = 2.4\,\nabla^\alpha(\Delta_p) \quad \text{and} \quad \nabla^\alpha m = \nabla^\alpha\left(\rho\cdot\Delta_p^d\right)\ , \tag{6.1}$$

where d denotes the dimension of the problem. Both, the particle mass and the kernel length are updated according to

$$\frac{Dm_i}{Dt} = v_i^\alpha\,\frac{\partial m}{\partial x_i^\alpha}\ , \qquad \frac{Dh_i}{Dt} = v_i^\alpha\,\frac{\partial h}{\partial x_i^\alpha}\ . \tag{6.2}$$

The gradients of the particle mass and kernel length follow from the analytical description (6.1) which reduces the computational effort compared to an evaluation based on an additional kernel operation [59]. Figure 6.3 illustrates the basic set-up.

Since the particle mass can change, the continuity equation is no longer necessarily source free and the source term s_m in Eq. (2.1) is different from zero. Thus, Eq. (2.2)

needs to be supplemented by an appropriate source term to the RHS which accounts for the variation of the particle mass

$$s_{\rho_i} = \sum_{j=1}^{N} V_j v_j^\alpha \frac{\partial \rho_j}{\partial x_j^\alpha} W_{ij} \tag{6.3}$$

which can be simplified to

$$s_{\rho_i} = \sum_{j=1}^{N} v_j^\alpha \frac{\partial m}{\partial x_j^\alpha} W_{ij} \ . \tag{6.4}$$

The variation of particle masses intents to result in a variation of particle volumes at (ideally) constant density. Hence particles should adjust the interparticle distance when entering the variable resolution zone. Using a weakly compressible approach, the particle spacing is controlled by the pressure-density relation (3.43) which augments density variations introduced by Eq. (3.26) into counteracting pressure changes that aim to restore the particles into constant density positions. In an incompressible fluid, density variations bias volume variations measured by the divergence of the velocity field. In conjunction with constant mass particles, the divergence should ideally vanish. When attention is given to variable particle masses, the change of mass should ideally correspond to a change of volume. Thus, the generalised density change is obtained from the imbalance between the divergence of the velocity field and the transient change of particle mass (6.4) due to particle convection.

In practice, the source term initially introduces a density change which leads to a change of the particle's pressure caused by the state equation (3.43). In the case of increasing masses, the resulting overpressure causes the particles to rearrange until an increased average particle distance is obtained that matches the updated mass. For decreasing masses, the mechanism is working in a converse manner. Due to the rearrangement, the density is balanced again. The velocity divergence is adjusted accordingly from the momentum equation.

Analogous to the continuity equation, the classical momentum equation (2.3) holds only for solenoidal fields. Therefore, a source term is also added to the RHS of the momentum equation

$$s_{v_i^\alpha} = -\sum_{j=1}^{N} \frac{v_i^\alpha}{m_i} \frac{m_j}{\rho_j} \left(v_j^\beta \frac{\partial m}{\partial x_j^\beta} W_{ij} \right) \ . \tag{6.5}$$

The source term (6.5) ensures a conservation of the particle's momentum that would otherwise be increased by growing particle masses (and vice versa if masses are decreased).

Important to be noted, the global mass and volume are not necessarily preserved which is a deliberate feature of the present strategy. The latter is deemed defensible for free-surface flows. Using the variable resolution scheme, both parameters governing the kernel function, i.e. h and r_{ij}, can vary in space and time. However, the kernel function requires a modification for different entering kernel widths h_i and h_j. In order to remove any ambiguity and preserve a conservative particle interaction, the employed kernel function is assigned to the average of the interacting particles

$$\overline{W}_{ij} = \frac{1}{2}\left[W_{ij}(r,h_i) + W_{ij}(r,h_j)\right] \ . \tag{6.6}$$

Moreover, the gradient of the kernel function, which frequently occurs in the governing equations, needs be supplemented by the second term which addresses the spatial variation of the kernel width, viz.

$$\underline{\nabla} W_{ij} = \frac{\partial W_{ij}}{\partial r}\underline{\nabla} r + \frac{\partial W_{ij}}{\partial h}\underline{\nabla} h. \tag{6.7}$$

Following the above mentioned procedure, a conservative formulation is maintained due to producing symmetrical interactions

$$\begin{aligned}\overline{\underline{\nabla} W_{ij}} = &\frac{1}{2}\left[\frac{\partial W_{ij}(r,h_i)}{\partial r}\underline{\nabla} r + \frac{\partial W_{ij}(r,h_i)}{\partial h}\underline{\nabla} h_i\right] \\ &+\frac{1}{2}\left[\frac{\partial W_{ij}(r,h_j)}{\partial r}\underline{\nabla} r + \frac{\partial W_{ij}(r,h_j)}{\partial h}\underline{\nabla} h_j\right].\end{aligned} \tag{6.8}$$

All terms of the gradient expression (6.8) are evaluated analytically and no additional SPH operation is required. The source terms (6.4, 6.5) can be calculated within the existing momentum and continuity equation neighbour loops. Hence, the variable-resolution scheme causes virtually no computational surplus.

The technique helps to significantly reduce the computational effort, in particular as regards the resolution of a far field. Since the amount of particles is kept constant, dynamic load balancing is no issue and the parallel performance remains unchanged. The advantage of the Eulerian over the Lagrangian variable-resolution method [76] refers to the avoidance of severe particle distribution inhomogeneities, which also supports the stability and accuracy of the algorithm.

7 Numerical Model

This chapter describes the solving procedures that are applied within GADGET-$^{\mathrm{H}}2^{\mathrm{O}}$ in conjunction with the constitutive equations presented in chapters 4, 5 and 6. Beside SPH approximations of the governing equations, numerical details such as correction and stabilization schemes, evaluation of soil concentration and boundary treatment are included. Furthermore, the utilized neighbour search and parallelisation strategies are outlined.

7.1 Governing equations

Comprehensive derivations of several alternative SPH approximations of the continuity and momentum equation are given in section 3.4. The present code utilizes symmetric SPH formulations for both equations to reduce errors arising from conservation problems [49] and to maintain Galilean invariance. They are supplemented by source terms for simulations which apply variable resolutions following the variable particle-mass scheme outlined in section 6.2.

7.1.1 Continuity equation

Throughout the present work, the discrete form of the continuity equation introduced as Eq. (3.26) is deployed

$$\frac{D\rho_i}{Dt} = \sum_{j=1}^{N} m_j \left(v_i^\alpha - v_j^\alpha\right) \nabla_i^\alpha W_{ij} + s_{\rho_i} \,, \tag{7.1}$$

with a source term s_{ρ_i} according to section 6.2

$$s_{\rho_i} = \sum_{j=1}^{N} v_j^\alpha \nabla_j^\alpha m W_{ij} \,, \tag{7.2}$$

that accounts for spatial mass gradients in the case of variable resolution zones being present.

7.1.2 Momentum equation

The symmetric SPH approximation (3.40) is used to evaluate particle velocities

$$\frac{Dv_i^\alpha}{Dt} = \sum_{j=1}^{N} m_j \left(\frac{\sigma_i^{\alpha\beta}}{\rho_i^2} + \frac{\sigma_j^{\alpha\beta}}{\rho_j^2} \right) \nabla_i^\beta W_{ij} + \frac{f_i^\alpha}{\rho_i} + s_{v_i^\alpha} \ . \tag{7.3}$$

Following Eq. (2.5), it can be rewritten as

$$\frac{Dv_i^\alpha}{Dt} = -\sum_{j=1}^{N} m_j \left(\frac{p_i}{\rho_i^2} + \frac{p_j}{\rho_j^2} \right) \nabla_i^\alpha W_{ij} + \left(\frac{\tau_i^{\alpha\beta}}{\rho_i^2} + \frac{\tau_j^{\alpha\beta}}{\rho_j^2} \right) \nabla_i^\beta W_{ij} + \frac{f_i^\alpha}{\rho_i} + s_{v_i^\alpha} \ . \tag{7.4}$$

All regarded material phases are captured by a WCSPH approach, therefore the pressure p in Eq. (7.4) directly follows from the state equation (3.43)

$$p = \left(\left(\frac{\rho}{\rho_0} \right)^7 - 1 \right) B \ . \tag{7.5}$$

As pointed out in detail in section 3.5, the reference pressure B is set as a function of the maximum fluid velocity v_{max}

$$B = \frac{100 v_{max}^2 \rho_0}{7}. \tag{7.6}$$

For the evaluation of deviatoric stresses $\tau^{\alpha\beta}$, it needs to be distinguished between fluids and solids as discussed in chapter 4. Furthermore, external volumetric forces caused by propulsion devices and gravitation as well as a source term for variable resolutions following the scheme outlined in section 6.2 need to be considered.

Fluid

The general fluid formulation

$$\tau_{\mathbf{f}}^{\alpha\beta} = 2\mu_{\mathbf{f}} \dot{\epsilon}^{\alpha\beta} \quad \text{with} \quad \dot{\epsilon}^{\alpha\beta} = \frac{1}{2} \left[\frac{\partial v^\beta}{\partial x^\alpha} + \frac{\partial v^\alpha}{\partial x^\beta} \right] - \frac{1}{3} \left(\frac{\partial v^\gamma}{\partial x^\gamma} \right) \delta^{\alpha\beta} \tag{7.7}$$

requires an SPH approximation of the shear rate $\dot{\epsilon}^{\alpha\beta}$. Applying the SPH-gradient formulation (3.7) to $\dot{\epsilon}^{\alpha\beta}$ yields

$$\dot{\epsilon}_i^{\alpha\beta} = \frac{1}{2} \sum_{j=1}^{N} \left(\frac{m_j}{\rho_j} v_j^\beta \right) \frac{\partial W_{ij}}{\partial x_i^\alpha} + \frac{1}{2} \sum_{j=1}^{N} \left(\frac{m_j}{\rho_j} v_j^\alpha \right) \frac{\partial W_{ij}}{\partial x_i^\beta} - \left[\frac{1}{3} \sum_{j=1}^{N} \left(\frac{m_j}{\rho_j} v_j^\gamma \right) \frac{\partial W_{ij}}{\partial x_i^\gamma} \right] \delta^{\alpha\beta} \tag{7.8}$$

which can be converted to a symmetric expression by making use of the identity

$$\nabla^\alpha 1 = \sum_{j=1}^{N} V_j \nabla^\alpha W_{ij} = 0 \ , \tag{7.9}$$

$$\dot{\epsilon}_i^{\alpha\beta} = \frac{1}{2}\sum_{j=1}^{N}\left[\frac{m_j}{\rho_j}(v_i^\beta - v_j^\beta)\right]\ \frac{\partial W_{ij}}{\partial x_i^\alpha} + \frac{1}{2}\sum_{j=1}^{N}\left[\frac{m_j}{\rho_j}(v_i^\alpha - v_j^\alpha)\right]\ \frac{\partial W_{ij}}{\partial x_i^\beta} \tag{7.10}$$

$$- \left[\frac{1}{3}\sum_{j=1}^{N}\frac{m_j}{\rho_j}(v_i^\gamma - v_j^\gamma)\frac{\partial W_{ij}}{\partial x_i^\gamma}\right]\delta^{\alpha\beta}\ .$$

Assuming equivalence of the two symmetric formulations of the continuity equation (3.23) and (3.26)

$$\sum_{j=1}^{N}\left[\frac{m_j}{\rho_j}(v_i^\beta - v_j^\beta)\right]\ \frac{\partial W_{ij}}{\partial x_i^\beta} = \frac{1}{\rho_i}\sum_{j=1}^{N}\left[m_j(v_i^\beta - v_j^\beta)\right]\ \frac{\partial W_{ij}}{\partial x_i^\beta}. \tag{7.11}$$

and substituting the corresponding terms in Eq. (7.10) gives the final expression that is used in the present code:

$$\dot{\epsilon}_i^{\alpha\beta} = \frac{1}{2\rho_i}\sum_{j=1}^{N}\left[m_j(v_i^\beta - v_j^\beta)\right]\ \frac{\partial W_{ij}}{\partial x_i^\alpha} + \frac{1}{2\rho_i}\sum_{j=1}^{N}\left[m_j(v_i^\alpha - v_j^\alpha)\right]\ \frac{\partial W_{ij}}{\partial x_i^\beta} \tag{7.12}$$

$$- \left[\frac{1}{3\rho_i}\sum_{j=1}^{N} m_j(v_i^\gamma - v_j^\gamma)\ \frac{\partial W_{ij}}{\partial x_i^\gamma}\right]\delta^{\alpha\beta}\ .$$

Solid

For the complete evaluation of the elastic deviatoric stress tensor $\tau_{\mathbf{se}}^{\alpha\beta}$ (Eq. (4.13)), the rotational tensor $\dot{\omega}^{\alpha\beta}$

$$\dot{\omega}^{\alpha\beta} = \frac{1}{2}\left(\frac{\partial v^\beta}{\partial x^\alpha} - \frac{\partial v^\alpha}{\partial x^\beta}\right) \tag{7.13}$$

needs to be transformed into an SPH-expression which can be obtained analogous to the shear rates (7.12). The discrete tensor approximation reads

$$\dot{\omega}_i^{\alpha\beta} = \frac{1}{2\rho_i}\left[\sum_{j=1}^{N}\left[m_j(v_i^\beta - v_j^\beta)\right]\ \frac{\partial W_{ij}}{\partial x_i^\alpha} - \sum_{j=1}^{N}\left[m_j(v_i^\alpha - v_j^\alpha)\right]\ \frac{\partial W_{ij}}{\partial x_i^\beta}\right]\ . \tag{7.14}$$

External volumetric forces

External volumetric forces like gravity and body forces from propulsion devises (section 5.2) are represented by the vector f_i^α in Eq. (7.4)

$$f_i^\alpha = \rho_i g^\alpha + \frac{b_i^\alpha}{V_i}\ . \tag{7.15}$$

In Eq. (7.15), g^α denotes the vector of gravitational acceleration. The propulsion body forces derived in section 5.2 can be casted into the vector b_i^α.

Variable resolution source term

In case the spatial mass gradients are considered due to variable particle resolutions, the source term in Eq. (7.4) takes the non-zero expression

$$s_{v_i^\alpha} = -\sum_{j=1}^{N} \frac{v_i^\alpha}{m_i}\frac{m_j}{\rho_j}\left(v_j^\beta \frac{\partial m}{\partial x_j^\beta} W_{ij}\right) . \tag{7.16}$$

7.2 Kernel function

A cubic spline kernel function of width h is used in the present study. It provides the necessary mathematical features outlined in section 3.3. The even kernel function is obtained from the normalised distance $r/h = \|x_i^\alpha - x_j^\alpha\|/h$, viz.

$$W(r,h) = \alpha_d \begin{cases} 1 - 6\left(\frac{r}{h}\right)^2 + 6\left(\frac{r}{h}\right)^3 & \text{if} \quad 0 \le \frac{r}{h} \le \frac{1}{2} \\ 2\left(1 - \frac{r}{h}\right)^3 & \text{if} \quad \frac{1}{2} < \frac{r}{h} \le 1 \\ 0 & \text{if} \quad \frac{r}{h} > 1 \end{cases} . \tag{7.17}$$

The integral over the kernel function is normalised to unity using $\alpha_d = \frac{40}{7\pi h^2}$ and $\alpha_d = \frac{8}{\pi h^3}$ in 2D and 3D, respectively. The relation between the kernel width h and the initial particle spacing Δ_P is assigned to $h = 2.4\,\Delta_P$ in the present work.

The spatial derivative of Eq. (7.17) needs to consider gradients of the particle distance as well as kernel length gradients

$$W(r(x^\beta), h(x^\beta)) \;\rightarrow\; \nabla W = \frac{\partial W}{\partial r}\nabla r + \frac{\partial W}{\partial h}\nabla h. \tag{7.18}$$

The derivative with respect to r reads

$$\frac{\partial W(r,h)}{\partial r} = \tilde{\alpha}_{rd} \begin{cases} -2\frac{r}{h} + 3\left(\frac{r}{h}\right)^2 & \text{if} \quad 0 \le \frac{r}{h} \le \frac{1}{2} \\ -1\left(1 - \frac{r}{h}\right)^2 & \text{if} \quad \frac{1}{2} < \frac{r}{h} \le 1 \\ 0 & \text{if} \quad \frac{r}{h} > 1 \end{cases} , \tag{7.19}$$

with $\tilde{\alpha}_{rd} = \frac{240}{7\pi h^2}$, $\tilde{\alpha}_{rd} = \frac{48}{\pi h^3}$ in 2D and 3D.

In case of variable resolution zones being applied, h is no longer a constant. The associated part of the derivative is evaluated by

$$\frac{\partial W(r,h)}{\partial h} = \tilde{\alpha}_{hd} \begin{cases} 2\left(\frac{r}{h}\right)^2 - 3\left(\frac{r}{h}\right)^3 & \text{if} \quad 0 \leq \frac{r}{h} \leq \frac{1}{2} \\ \frac{r}{h} - 2\left(\frac{r}{h}\right)^2 + \left(\frac{r}{h}\right)^3 & \text{if} \quad \frac{1}{2} < \frac{r}{h} \leq 1 \\ 0 & \text{if} \quad \frac{r}{h} > 1 \end{cases}, \tag{7.20}$$

with the normalisation coefficients $\tilde{\alpha}_{hd} = -\frac{480}{7\pi h^4}$, $\tilde{\alpha}_{hd} = \frac{144}{\pi h^5}$ in 2D and 3D.

7.3 Correction and stabilisation techniques

The section outlines several techniques being applied to enhance the accuracy and numerical stability of the standard WCSPH model. This includes kernel normalisation, additional smoothing of field values and interface treatment. Furthermore, hydrostatic pressure initialization and damping approaches are described aiming at appropriate initial conditions.

7.3.1 Kernel correction

The kernel function 7.17 is normalised to unity which represents a key feature of smoothing functions as described in 3.3. However, the respective discrete partition of unity ($\sum_j W_{ij} V_j = 1$) might not be satisfied, especially close to a boundary or in the interior once the particles have started to move. The latter can lead to numerical instabilities and impair the convergence of the method. Accordingly, a normalisation of the kernel function based on the widely used Shepard normalisation technique [92, 30] is a remedy also being adopted here

$$W_{ij}^* = \frac{W_{ij}}{\alpha_w} \;, \quad \text{with} \quad \alpha_w = \sum_{j=1}^{N} \frac{m_j}{\rho_j} W_{ij}. \tag{7.21}$$

The Shepard normalisation helps to restore zero-order consistency which ensures an accurate reproduction of homogeneous field values (i.e. $f_i = f_j = const.$), viz.

$$f_i = \sum_{j=1}^{N} V_j f_j W_{ij}^* \rightarrow f_i = f_j \sum_{j=1}^{N} V_j W_{ij}^* \rightarrow 1 = \sum_{j=1}^{N} V_j W_{ij}^* \;. \tag{7.22}$$

The approach is applied to the kernel gradients by referring to the initial configuration

$$\nabla W_{ij}^* = \frac{\alpha_{w0}}{\alpha_w} \nabla W_{ij} \;, \tag{7.23}$$

where α_{w0} represents the initial state of α_w. Expression (7.23) tends to maintain the initial desired spatial descretisation and accordingly minimizes particle clustering and clumping.

Note that this form does not correspond to the one obtained after differentiation of the Shepard kernel [30].

The corrected kernel function W_{ij}^* and kernel gradients ∇W_{ij}^* are used throughout the simulations as substitutes for W_{ij} and ∇W_{ij}. In the case of variable particle resolution and smoothing lengths a correction of the averaged kernel function (6.6) reads

$$\overline{\underline{\nabla} W_{ij}} = \frac{1}{2}\left[\frac{\partial W_{ij}^*(r,h_i,\alpha_{w_i})}{\partial r}\underline{\nabla} r + \frac{\partial W_{ij}^*(r,h_i,\alpha_{w_i})}{\partial h}\underline{\nabla} h_i\right] + \frac{1}{2}\left[\frac{\partial W_{ij}^*(r,h_j,\alpha_{w_j})}{\partial r}\underline{\nabla} r + \frac{\partial W_{ij}^*(r,h_j,\alpha_{w_j})}{\partial h}\underline{\nabla} h_j\right]. \tag{7.24}$$

7.3.2 Velocity, pressure and density smoothing

Along with the particles' density and momentum, their position is advanced in time using $\dot{x}^\alpha = v^\alpha$. Because particles should properly interact at any time, the maintenance of regular particle locations is a frequently addressed issue. In more particular, the approximation (3.8) fails to converge when being not well-sampled anymore. The weakly compressible SPH approach utilized in the present study often displays disturbances and particle clustering for problems featuring negligible dynamics, e.g. in hydrostatic investigations. Accordingly, Monaghan [65] suggested an additional smoothing – commonly referred to by the acronym XSPH (eXtended SPH) – which is usually only imposed on the change of the particles' location by introducing a specific displacement velocity field

$$\frac{dx_i^\alpha}{dt} = v_{ix}\,, \qquad v_{ix} = v_i^\alpha - \tilde{\epsilon}_v \sum_{j=1}^{N} V_j \left(v_j^\alpha - v_i^\alpha\right) W_{ij}^* \tag{7.25}$$

and aims to conserve locally regular particle spacings. In the present work, the XSPH approach is applied by introducing the smoothing operation to both the momentum and displacement velocity field v^α

$$v_i^\alpha \rightarrow v_i^\alpha - \tilde{\epsilon}_v \sum_{j=1}^{N} V_j \left(v_j^\alpha - v_i^\alpha\right) W_{ij}^*\,. \tag{7.26}$$

Equation (7.26) is employed to evaluate the right hand side of the displacement, continuity and momentum equation. The advantage of this procedure refers to an implicit smoothing of every property that depends on the velocity field at the expense of an artificial damping. In order to limit the XSPH influence, $\tilde{\epsilon}_v$ should be assigned to a value that is just sufficiently large to provide a clean velocity field without changing the gross dynamics

of the simulation

$$\tilde{\epsilon}_v = 0.00125 \cdot \left[\frac{\Delta t \cdot v_{max}}{h}\right] \left[\frac{v_{max}}{\sqrt{h\,g}}\right] \ . \tag{7.27}$$

The respective $\tilde{\epsilon}_v$ values are usually fairly small $\tilde{\epsilon} \sim 10^{-2} - 10^{-3}$. Moreover, an additional smoothing is introduced for the particle pressure when large dynamics are involved – e.g. in impact cases – along a route suggested by Manenti et al. [55]

$$p_i \rightarrow p_i - \tilde{\epsilon}_p \sum_{j=1}^{N} V_j \left(p_j - p_i\right) W_{ij}^* \ . \tag{7.28}$$

The smoothing coefficient is assigned to $\tilde{\epsilon}_p = 5\,\tilde{\epsilon}_v$ when the pressure difference between particles i and j exceeds twice their hydrostatic pressure difference. Otherwise, no pressure smoothing is applied ($\tilde{\epsilon}_p = 0$). In order to keep a consistent pressure/density relation, the density is readjusted to the smoothed pressure by inverting Eq. (7.5):

$$\tilde{\rho}_i = \left(\frac{\tilde{p}}{B} + 1\right)^{\frac{1}{7}} \rho_0 \ . \tag{7.29}$$

Mind that this explicit filter techniques can also be interpreted in the framework of LES [35].

7.3.3 Density blending

Due to the density difference between water and soil, pressure instabilities arise from the applied equation of state (7.5) at the water-soil interface. The problem can be addressed by modifying the pressure-gradient evaluation for sharp interfaces as outlined by Bui et al. [14] or introducing a stabilisation term based on a buoyancy correction for very large density ratios as shown by Kruisbrink [43].

In the present study, the particle's mass, density and reference density are blended in agreement with the species concentration $\tilde{c}_{\mathbf{s}}$ to compose a suspension layer, viz.

$$m = \tilde{c}_{\mathbf{s}} m_{\mathbf{s}} + (1 - \tilde{c}_{\mathbf{s}}) m_{\mathbf{f}} \ , \quad \rho = \rho_{0b} + (\bar{\rho} - \bar{\rho}_{0b}) \ , \tag{7.30}$$

with $\rho_{0b} = \tilde{c}_{\mathbf{s}} \rho_{0\mathbf{s}} + (1 - \tilde{c}_{\mathbf{s}}) \rho_{0\mathbf{f}}$. Here $\bar{\rho}$ and $\bar{\rho}_{0b}$ refer to values from the previous time steps.

7.4 Initialisation and initial transient

The pressure field within a water column that is abruptly loaded by gravity shows an undesirable oscillating behaviour. To avoid such initial disturbances in SPH simulations,

the water particles' pressure can be initialised based on hydrostatic conditions

$$p_{i_{w_{init}}} = \rho_w g h_w \ , \tag{7.31}$$

with the water density ρ_w, gravitational constant g and the distance on the gravitational axis between the particle and the free surface h_w. Soil particles located underneath a water layer are initialised in a similar way

$$p_{i_{s_{init}}} = \rho_w g h_w + \rho_s g h_s \ , \tag{7.32}$$

with the soil density ρ_s and the distance on the gravitational axis between the particle and the phases interface h_s. In this case, h_w is the distance between water/soil interface and free surface.

The corresponding initial particle density is obtained from inverting Eq. (7.5):

$$\rho_{i_{init}} = \left(\frac{p_{i_{init}}}{B} + 1\right)^{\frac{1}{7}} \rho_0 \ . \tag{7.33}$$

Even if the particle pressure is initialised based on analytical considerations, initial transients can occur e.g. due to an irregular particle spacing. This can lead to undesirable pressure oscillations or noisy initial pressure fields. Especially the evaluation of soil strain strongly depends on an accurate pressure evaluation.

Bui et al. [12] therefore propose to damp these initial transients in order to start with non-oscilating initial soil stresses. Accordingly, a damping term can be added to the momentum equation

$$D_i^\alpha = -c_d v_i^\alpha \ , \tag{7.34}$$

with a damping coefficient $c_d \approx 0.001$.

7.5 Soil concentration

Knowledge about the volumetric soil concentration $\tilde{c}_\mathbf{s}$ is primarily needed for the evaluation of suspension viscosities (cf. section 4.3). Furthermore, $\tilde{c}_\mathbf{s}$ is used in conjunction with the density blending approach (section 7.3.3). The concentration inside the kernel width h is obtained from the algebraic expression

$$\tilde{c}_{i\mathbf{s}} = \frac{\sum_{k_{soil} \in h} V_k}{\sum_{k \in h} V_k} \ . \tag{7.35}$$

7.6 Boundary conditions

The present work utilizes the fixed particle approach discussed in section 3.6 for rigid walls. In conjunction with stationary walls, this is realized by imposing zero acceleration

$$a^{\alpha}_{i_{wall}} = 0 \; . \tag{7.36}$$

Many engineering applications are based on moving walls. Therefore, the wall-particle velocities $v^{\alpha}_{i_{wall}}$ can be assigned to the dedicated value $\tilde{v}^{\alpha}_{wall}$. Note that $\tilde{v}^{\alpha}_{wall}$ might be a time dependent function $\tilde{v}^{\alpha}_{wall}(t)$.

The actual wall position can be evaluated from an integration of the prescribed wall velocities

$$x^{\alpha}_{i_{wall_{(I+1)}}} = x^{\alpha}_{i_{wall_{(I)}}} + \tilde{v}^{\alpha}_{i_{wall_{(I)}}} \Delta t \; . \tag{7.37}$$

Alternatively, if possible, a compliant direct specification can be applied

$$x^{\alpha}_{i_{wall_{(I)}}} = \tilde{x}^{\alpha}_{wall_{(I)}} \; . \tag{7.38}$$

The latter is the favoured procedure as it does not include numerical integration errors.

In order to minimize kernel truncations at the boundaries, multiple rows of boundary particles are employed as illustrated in Fig. 7.1. In this work, the relationship between particle spacing and kernel length is kept constant with $h = 2.4\,\Delta_P$. Therefore, three rows of fixed particles provide “complete” kernel evaluations at the boundary. The density and pressure evaluation of wall particles and fluid particles in the kernel range of the wall is performed in a straight forward way. Within the density loop, wall particles are treated as regular fluid particles except their prescribed velocity.

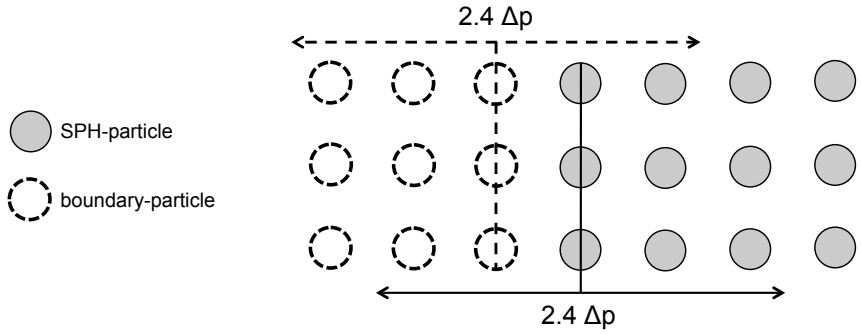

Figure 7.1: Zones of influence at a boundary for fixed boundary and standard SPH particles.

7.7 Time integration

7.7.1 Integration scheme

Time integration is performed using a symplectic leapfrog scheme. Similar to a Verlet [106] integration, the particle positions x^α and the particle accelerations a^α (i.e. forces) are updated every "entire" time step, whereas the particle velocities $\hat{v}^\alpha$ are computed at centred "intermediate" time steps, viz.

$$x^\alpha_{i_{(I+1)}} = x^\alpha_{i_{(I)}} + \hat{v}^\alpha_{i_{(I+1/2)}} \Delta t \ , \tag{7.39}$$

$$\hat{v}^\alpha_{i_{(I+3/2)}} = \hat{v}^\alpha_{i_{(I+1/2)}} + a^\alpha_{i_{(I+1)}} \Delta t \ , \tag{7.40}$$

with the bracketed subscript indices denoting the time level. Figure 7.2 displays the relationship between positions and velocities. The evaluation of positions is usually called *drift*, while the velocities are calculated in a *kick* step.

This explicit integration method provides second-order accuracy due to the staggered arrangement between the RHS and LHS variables of the evaluated equations. Its equivalence to a central difference scheme (CDS) can be shown by Taylor series expansions with the function's derivatives being defined at an intermediate time-step.

An advantage of the scheme over other biased second or higher-order approximations is related to the error term which accounts on uneven derivatives, only. Thus the truncation error does not lead to numerical diffusion which is associated to even derivatives. Therefore, the dissipation of the numerical procedure can accurately be controlled.

However, the integration scheme may lead to numerical instabilities. These can be minimized by adding a controlled level of artificial or physical viscosity and choosing small time-step sizes.

The procedure is started by an Euler-Integration over half a time-step for the velocity $\hat{v}^\alpha$. Additional to the velocity $\hat{v}^\alpha$, a second velocity v^α defined at the "entire" time-step is introduced. The physical properties - such as density, pressure, viscosity etc. - are evaluated at every "entire" time-step. Therefore, a velocity v is also needed for these instants, which is derived from applying an Euler-Integration to the acceleration a^α. As soon as the more accurate velocity $\hat{v}^\alpha$ is available for a new intermediate time-step, v is corrected by half an Euler-Integration step (cf. Fig. 7.2).

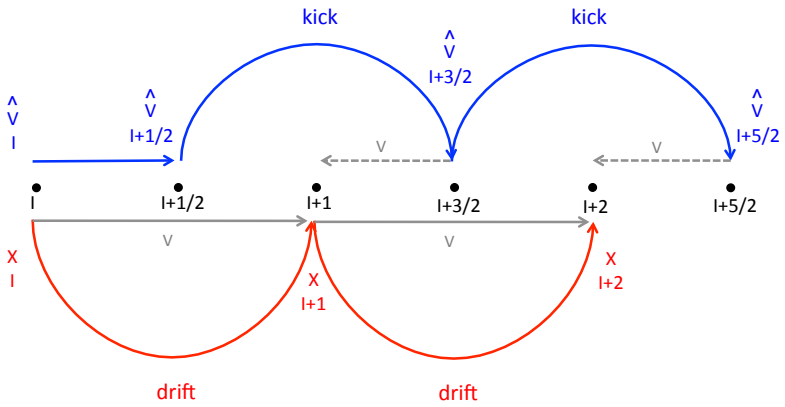

Figure 7.2: Leapfrog integration scheme.

A special treatment is applied to the density. Its evolution is obtained from a two-step approach. The first fraction utilizes equation (7.1) by means of

$$\rho_{i_{(I+1/2)}} = \rho_{i_{(I)}} + \dot{\rho}_{i_{(I)}} \frac{\Delta t}{2} \ . \tag{7.41}$$

The second fraction refers to an analytical solution of the continuity relation

$$\frac{D\rho}{Dt} = -\rho \frac{\partial v^\alpha}{\partial x^\alpha} + s_m \ , \tag{7.42}$$

$$\rho_{i_{(I+1)}} = \rho_{i_{(I+1/2)}} e^{((-\nabla^\alpha v^\alpha - \frac{v^\alpha \nabla^\alpha m}{m})\frac{\Delta t}{2})} \ . \tag{7.43}$$

This fractional step approach allows an evaluation of the pressure field at the “entire” as well as the “intermediate” time-steps.

Table 7.1: Values obtained from time integration and their dependencies.

Value	Symbol	Depending on
Entire Time-Step		
Position	x^α	$\hat{v}^\alpha$
Acceleration	a^α	v^α, ρ
Density	ρ	v^α
Velocity	v^α	a^α , $\hat{v}^\alpha$
Intermediate Time-Step		
Velocity	$\hat{v}^\alpha$	a^α
Density	ρ	v^α

7.7.2 Time-step restrictions

The time-step size is restricted by a generalized Courant number criterion (CFL-criterion). The criterion states that the condition

$$v_{sig}\frac{\Delta t}{h} \leq Co \tag{7.44}$$

needs to be fulfilled in order to accurately resolve a signal traveling through the continuum with the velocity v_{sig}. In conjunction with SPH, the kernel length h serves as a discretisation length scale. The Courant number Co defines the travel distance of a signal per time step Δt. In order to maintain a stable explicit integration scheme, Co needs to be restricted to $Co \approx 0.1$. The signal can result from pressure, viscosity or external volumetric forces (gravity, propeller thrust). Thus, three separate time-step restrictions are considered.

A limitation derived from traveling pressure waves reads

$$\Delta t \leq Co\,\frac{h}{c}\,. \tag{7.45}$$

Viscous influences are considered by

$$\Delta t \leq Co\,\frac{\rho h^2}{\mu} \tag{7.46}$$

and external forces reveal

$$\Delta t \leq Co\,\sqrt{\frac{h\rho}{f}}\,. \tag{7.47}$$

The actual time-step is given by the smallest value obtained from Eqs. (7.45, 7.46, 7.47).

7.8 Neighbour search and parallelisation

The nearest neighbour search and the parallelisation strategy of GADGET-$^{\mathrm{H}}2^{\mathrm{O}}$ are adopted from Springel's cosmological TreeSPH code GADGET-2 [95]. The high efficiency of these code structures have been the reason for choosing GADGET-2 as a basis for the development of the present hydrodynamic multi-physics SPH procedure. The following section provides a brief summary of the neighbour search and parallelisation approach which are

intimately connected with each other. A more elaborate description is given in Springel's original publication of the algorithm [95].

7.8.1 Nearest neighbour search

SPH-simulations require an efficient identification of nearest neighbours. As outlined by Springel et al. [96], a range-search based on a regular, isotropic search grid is unfavorable for clustered particle situations, which frequently occur in practical simulations. The nearest-neighbour search of GADGET-2 uses a more flexible hierarchical tree algorithm based upon a Barnes & Hut oct-tree (BH oct-tree) [3]. The search is based upon the oct-tree and the definition of a spherical search region around the location of the target particle.

During the set up of the BH oct-tree, the physical domain is hierarchically subdivided into cubical cells. These cells are associated to branched tree-nodes of the oct-tree. Each individual cell contains a cubic domain and hosts a certain number of particles. The oct-tree cells are further subdivided (branched) into 8 subcells (in 3D computations) if they contain more than one particle.

The search radius of the spherical region corresponds to the radius of the (local) kernel length h. The tree is walked for the search region. If the region overlaps with the current tree-node domain, the associated subcells are examined. If there is no overlap, the branch of the tree is ignored. The tree walk proceeds until all particles ("all" might also refer just to one, in special cases) of the investigated cell fall inside the search region and the resident particle(s) are added to the interaction list. The procedure is repeated until all paths in the tree are examined.

7.8.2 Parallelisation strategy

Parallel applications of GADGET-$^{\mathrm{H}}2^{\mathrm{O}}$ refer to data-parallel single-program multiple-data (SPMD) computations, where different processes use their own physical memory while running an individual copy of the code.

Grid-based Eulerian simulation procedures are traditionally parallelised in space by means of a static domain-decomposition technique. The technique is difficult to adopt to particle-simulation methods due to the dynamic relation between the particle position and the domain. Different decomposition approaches striving for an adequate dynamic load-

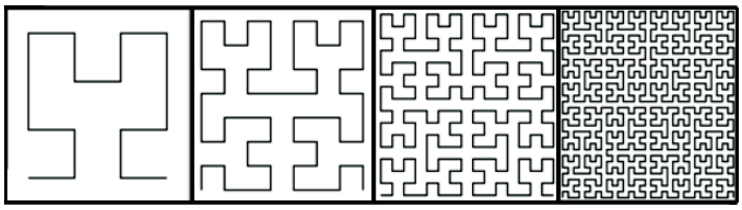

Figure 7.3: Two-dimensional Peano-Hilbert curves (2nd- to 5th-order).

and communication balancing exist for particle codes (cf. Moulinec et al. [70]). One possibility is to construct the domains with orthogonal recursive bisections as described by Dubinski [22]. This method was adopted earlier by Springel for the first version of GADGET [96]. In order to improve the parallel efficiency, the authors of GADGET have used a different approach for GADGET-2 [95]. The basic idea is to use a space-filling curve to map a 3D space into a 1D curve. The curve is chopped into segments which then define the different domains. The approach was first proposed by Warren and Salmon [111], who used a spatial ordering based upon Morton curves. This curve contains spatial discontinuities which can be a source of inefficiency. They also mentioned that Peano-Hilbert curves do not inhere such discontinuities, and might arguably be a better choice for the spatial ordering. Fig. 7.3 displays examples for a 2D Peano-Hibert curve, which is used in conjunction with GADGET-2.

The advantage of a domain decomposition based on a space-filling curve is the conservation of particle proximities. Particles that are located close to each other in physical space are also closely located along the space-filling curve. The curve-segments (or processor-domains) mostly consist of particles within a compact physical space. The governing nearest-neighbour interactions of the SPH-methodology can thus be evaluated with a minimum amount of particle information from other domains. This way, the inter-processor communication is reduced. Another benefit of the Peano-Hilbert ordering is related to cache optimisation. Particles often find most of their nearest neighbours in the same cache line. Therefore, the code balance is significantly improved by the Peano-Hilbert ordering.

The domain decomposition is performed in the following way: a *key* for each particle is computed by converting the particle's coordinates into an integer value. The Peano-Hilbert curve is constructed based on these *key-values*. The global list is segmented and distributed to the different processors. Accordingly, it is important to recall that the particle data and keys are distributed over the various processors. In order to establish a

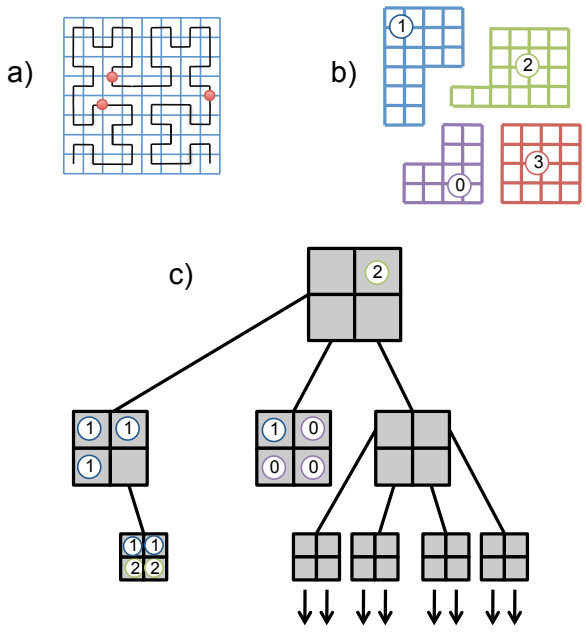

Figure 7.4: 2D sketch of the domain decomposition and the BH-tree on a single processor. The global Peano-Hilbert curve is chopped into pieces (a). The resulting domains are associated to different processors (b). On each processor, a local BH-tree is constructed (c). The sketch shows the tree on processor 3. Within the tree, the data of the neighbour processors are included as pseudo-particles.

global list, distributed data must be collected and merged into a joint space-filling curve. The sortation is carried out using the keys only. It employs an adaptive hashing method based upon pre-chopped local segments [95]. The collection of local segments from each processor are adjusted in order to generate a global key-list. Segments of this global list can then be distributed to the single processors. The particles are finally distributed to the processors in accord with the keys. This method is afflicted with smaller communication effort compared to a global sorting procedure.

Subsequent to the domain decomposition, local BH trees are constructed for each processor as described in section 7.8.1. The local trees correspond to top-level trees. They inhere the complete branches leading to the local particles in addition to the unique entrance nodes for residents of other processors, which are represented by pseudo particles. Fig. 7.4 illustrates the domain decomposition and tree construction process. The tree is updated each time-step in order to track the movement of particles outside the boundaries of the processor domain. Thereby, updates of the interior nodes of the local processor as well as modifications of pseudo-particle nodes are initiated. This offers the possibility to rarely repeat the domain decomposition, most likely at the expense of enhanced non-local contributions.

The neighbour search proceeds as usual. If a pseudo-particle node needs to be opened, the requesting particle is penciled for an export to the host processor of the pseudo-particle. Following all tree-walk operations on the local processor, penciled particles are exchanged between the processors and the unfinished tree walks are remotely continued. The results of the interaction with remotely located neighbours are send back to the local processor as partial results. The final step is to add the different partial results.

8 Validation and Verification

The following chapter presents different verification and validation cases. The studies aim to analyse the code's performance for a range of typical phenomena to be considered in harbour hydrodynamic simulations.

Examples included refer to single-phase fluid and soil problems as well as water/soil interaction cases. In addition, the capability of predicting static and dynamic pressure fields is scrutinised, followed by an evaluation of the variable resolution and 6DOF body motion models. The tests generally apply the correction and stabilising techniques outlined in section 7.3 as long as not differently stated.

8.1 Fluid motion

The predictive accuracy for fluid motion is evaluated for pressure and shear driven flows. SPH results obtained from the present procedure are compared to experimental and numerical reference data for a pressure/inertia driven dam break test-case. The analytical solutions for axisymmetric Couette flows are employed as a benchmark for shear flows.

8.1.1 Dam break flow

Dam break examples represent typical validation cases for pressure/inertia driven free-surface flows. Early SPH investigations of this type of flow were performed e.g. by Monaghan [65]. The present work refers to a widely used benchmark experiment presented by Martin and Moyce in 1952 [60].

In this specific example, the considered initial water column's height is twice as large as its width a. At time $t = 0$ s, the column is set free at one side, which was realized experimentally by a sudden removal of a paper diaphragm that was initially supporting the fluid.

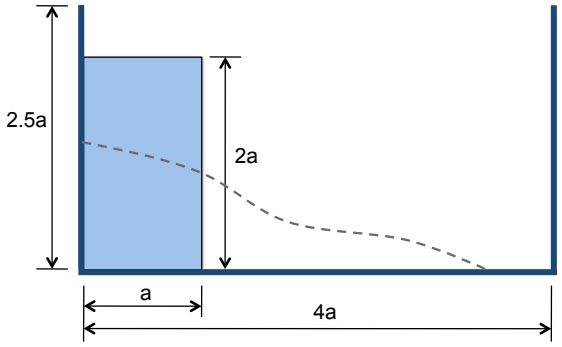

Figure 8.1: Schematic sketch of the initial set-up for the investigated dam break flow. A water column is collapsing in an open-top basin.

Figure 8.1 illustrates the set-up used in the present study which differs from the original experiment with respect to the observed basin. The basin's length is limited to $4a$ and the vertical walls have a height of $2.5a$. The investigated configuration has been used in earlier validation exercises, e.g. by Sauer [88] for the validation of a VoF procedure. The change of the basin size introduces an enhanced complexity to the test-case due to the re-entering of water that is deflected by the limiting wall.

An initial column width of $a = 146$ mm as reported by Sauer is adopted in this work to support a comparison of GADGET-$^{H}2^{O}$'s results with the experiments and Sauer's numerical reference. The fluid is considered to be water with a density of $\rho = 1000$ kg/m^3 and a dynamic viscosity of $\mu = 1 \cdot 10^{-3}$ Pa s. Note that the present simulation does not account for a second phase (air), contrary to the VoF reference simulations.

The water column is discretised in 2D by 71 particles in the horizontal and 141 particles in the vertical direction, leading to a total of 10011 constant-mass particles with a $2.085714 \cdot 10^{-3}$ m spacing. This particle spacing is chosen to match the edge length of the hexahedral cells used by the VoF procedure [88]. Fluid particles can leave the basin at the open top but are obstructed from reentering.

Figures 8.2 and 8.3 show contours of the collapsing water column at different instants, both for the SPH simulation and the VoF reference. A very good agreement can be observed up to $t = 0.6$ s. After this time, the fluid, wich was deflected by the vertical wall, hits back into the basin and impacts into the remaining water on the bottom of the basin. The snapshots taken at $t =$0.8 s and $t = 1.0$ s still indicate a fair accordance of the basic flow characteristics between the two simulations. Obvious deviations are related to the position and shape of enclosed air or void spaces, respectively. The differences in the results

can be attributed to the absence of the second phase in the present SPH simulations.

In their experiments, Martin and Moyce [60] evaluated the remaining water column height η and the front position of the surge z. Both values are normalised by introducing the dimensionless height H and width Z

$$H = \frac{\eta}{2a} \qquad , \qquad Z = \frac{z}{a}.$$

The corresponding dimensionless times τ and T read

$$\tau = t\sqrt{\frac{g}{a}} \qquad , \qquad T = t\sqrt{\frac{2g}{a}}.$$

The resulting curves are constructed with respect to the fixed reference points $Z = 1.44$ with $T = 1.19$ and $H = 1.00$ with $\tau = 0$. The employed normalisations and reference points are applied to both considered numerical simulations (SPH, VoF). For the SPH results, z is taken as the horizontal position of the first particle of the surge front. The height η is evaluated at a distance of four-times the particle spacing away from the left wall. This position is chosen in order to reduce inaccuracies that are induced by the applied wall boundary model.

A comparison of the SPH results to experimental data and the numerical reference is depicted in Figs. 8.4 and 8.5. In the diagrams, the normalised time $\tau = 5$ corresponds to $t \approx 0.6$ s and $T = 3$ to $t \approx 0.26$ s. respectively. The results obtained by GADGET-$^{\mathrm{H}}2^{\mathrm{O}}$ are in very good agreement with the VoF reference as well as the experiments, especially for the column's height. Some deviations between the two numerical predictions occur for the surge front's position which are probably due to the absence of the second phase in the present SPH simulations. The dam break test-case therefore demonstrates that the procedure provides a satisfactory accuracy for pressure driven free-surface flows.

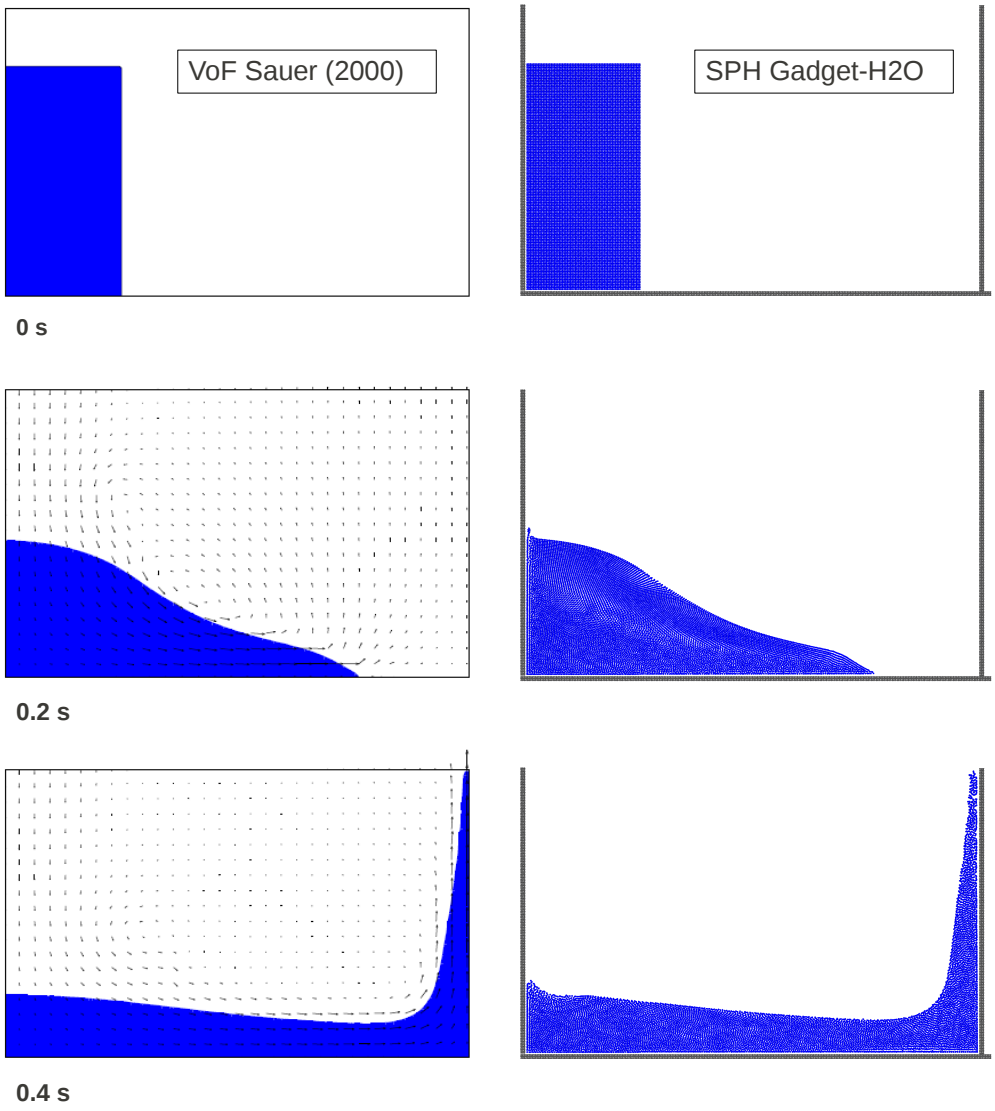

Figure 8.2: Contours of the collapsing water column at t = 0 s, t = 0.2 s and t = 0.4 s. The left sequence is taken from Sauer [88] and represents a mesh-based reference solution. Results obtained by GADGET-$^{H}2^{O}$ are shown on the right.

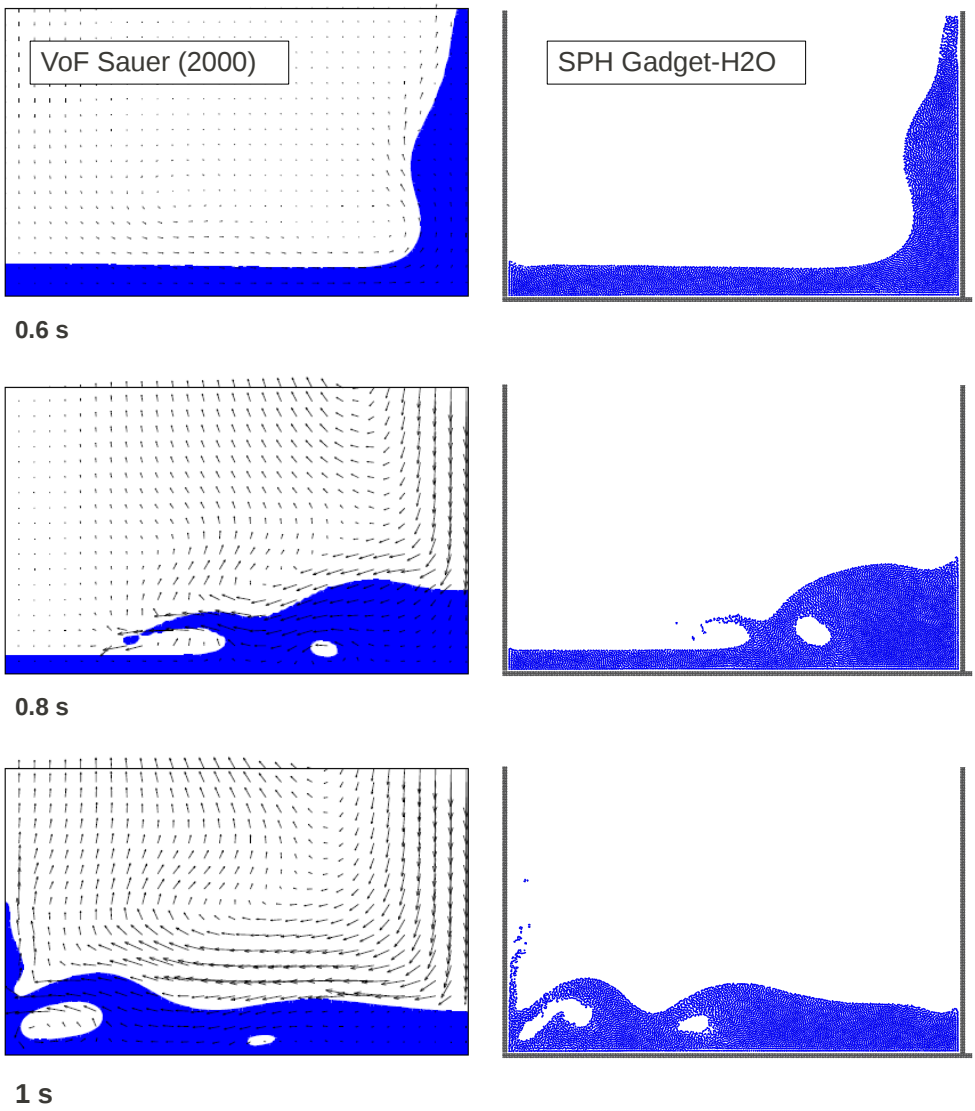

Figure 8.3: Contours of the collapsing water column at t = 0.6 s, t = 0.8 s and t = 1.0 s. The left sequence is taken from Sauer [88] and represents a mesh-based reference solution. Results obtained by GADGET-$^{H}2^{O}$ are shown on the right.

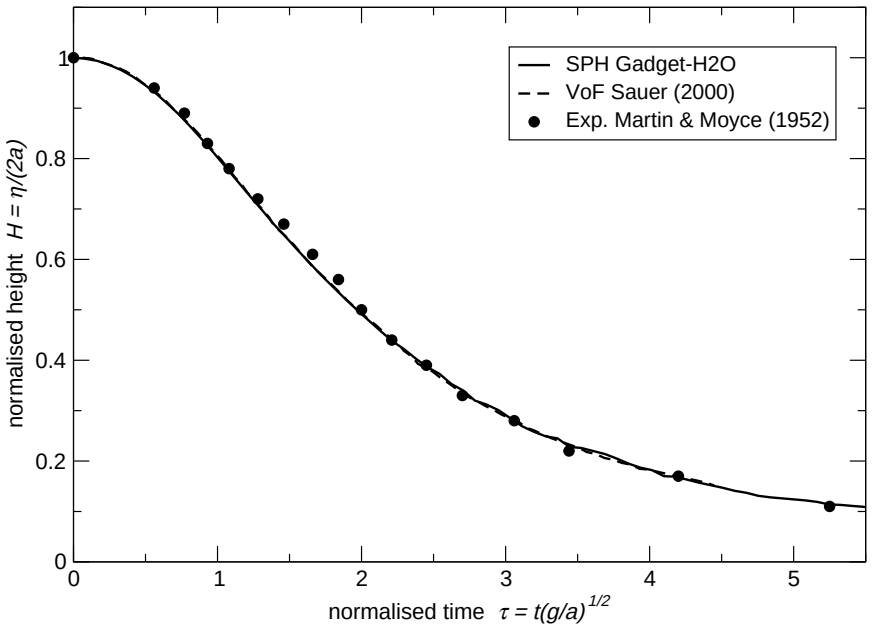

Figure 8.4: Evolution of collapsing water column by means of remaining column height.

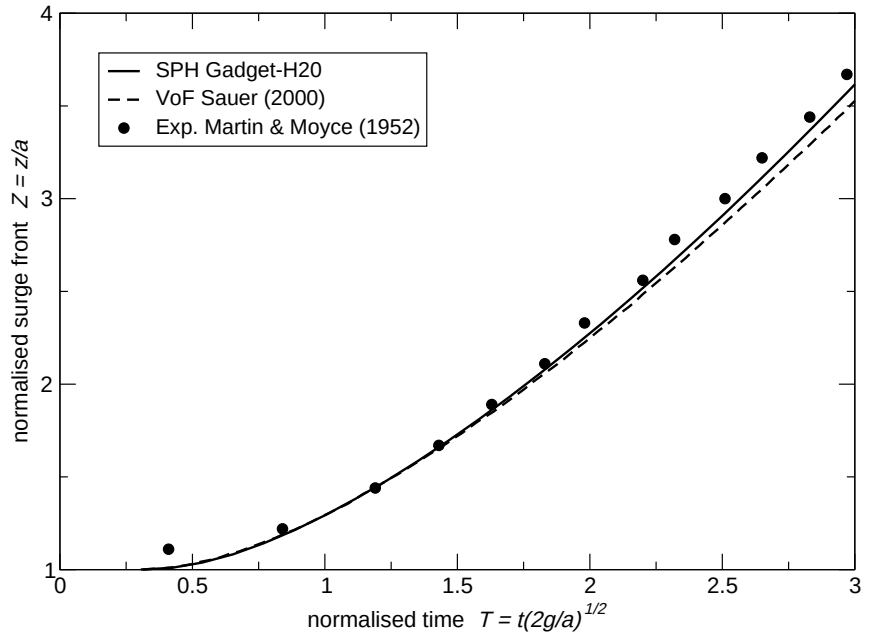

Figure 8.5: Evolution of collapsing water column by means of the surge position.

8.1.2 Axisymmetric Couette-Flow

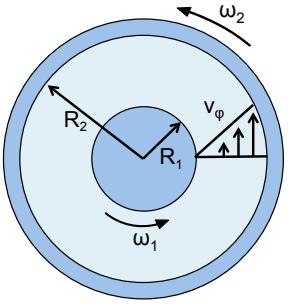

Figure 8.6: Schematic sketch of the axisymmetric Couette-Flow. A shear driven velocity profile develops between two cylinders rotating with the angular velocities ω_1 and ω_2.

The shear driven 2D flow between two coaxial cylinders rotating with different angular velocities ω_1 and ω_2 is commonly referred to as axisymmetric Couette-Flow (cf. Fig. 8.6). For stable, laminar conditions the circumferential velocity can be evaluated analytically by

$$v_\varphi(R_{ac}) = \frac{A_{ac}}{2} R_{ac} + \frac{B_{ac}}{R_{ac}} \ , \tag{8.1}$$

where R_{ac} denotes to the radius and the constants A_{ac} and B_{ac} depend on the geometry and the rotation rates of the cylinders [17, 89]. The test-case aims to examine the ability to capture viscous effects. Results are computed for two different rotation rates and refer to cylinder radii of $R_1 = 0.15$ m and $R_2 = 1$ m. Table 8.1 summarises the details of the two Couette-Flow cases. The first case features a linear velocity profile, the second case refers to a non-linear velocity profile. An estimation of the associated Reynolds and Taylor numbers yields $Re < 5$ and $Ta < 8$ with

$$Re = \frac{0.5\omega_2 \cdot R_2 \cdot (R_2 - R_1)}{\nu} \ , \ Ta = \sqrt{\frac{\omega_1^2 \cdot R_1 \cdot (R_2 - R_1)^3}{\nu^2}} \ ,$$

indicating laminar and stable flow conditions.

Table 8.1: Details of the examined single-phase Couette-Flow cases.

Couette-Flow case	ρ[kg/m^3]	μ[Pa · s]	ω_1[Hz]	ω_2[Hz]	A_{ac}[Hz]	B_{ac}[m^2/s]
(1) co-rotating:	1000	1000	10	10	20	0
(2) non-linear:	1000	1000	0	10	20.4604	-0.2302

The 2D problem is modelled using 19365 fluid particles with an initial particle spacing of $\Delta_p = 0.0125$ m. No gravitational force is considered and the walls are gradually accelerated to their prescribed rotation rate over a period of 0.1 second in order to suppress initial disturbances. Due to the low Reynolds number, the solution rapidly approaches steady-state. Figures 8.7 and 8.8 compare the predicted and analytical velocity profiles using normalised variables

$$v_{\varphi,n} = \frac{v_\varphi(R) - v_\varphi(R_1)}{v_\varphi(R_2) - v_\varphi(R_1)} \ , \qquad r_n = \frac{R_{ac} - R_1}{R_2 - R_1} \ .$$

An excellent predictive agreement is observed for the co-rotating linear verification case ($\omega_1 = \omega_2$). The agreement is still satisfactory if the inner cylinder is at rest ($\omega_1 = 0$). Small deviations occur close to the inner wall indicating inaccuracies of the wall-modelling strategy and the pressure-density relation. Nonetheless, results reveal that the procedure can simulate shear-driven phenomena with engineering accuracy, which is of importance for single-phase fluid and soil motion as well as suspension flows.

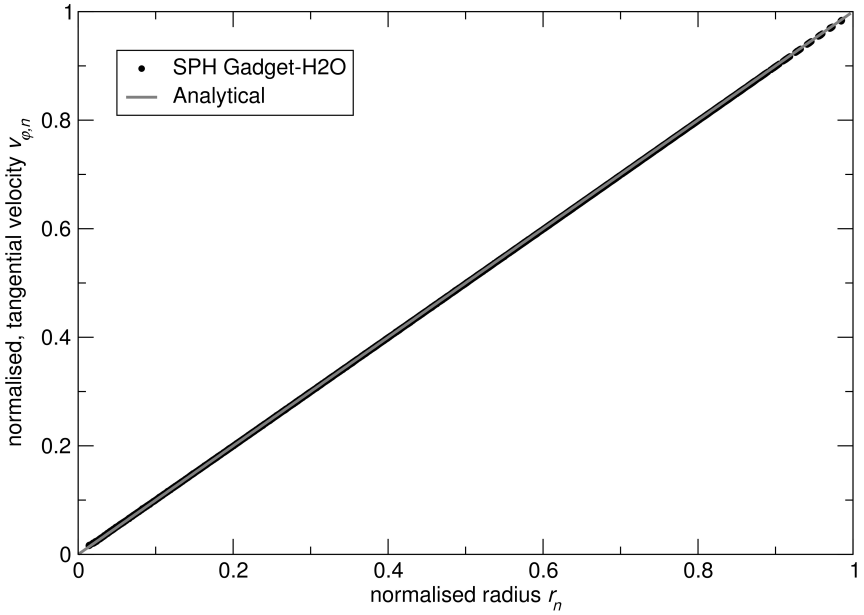

Figure 8.7: Predicted and analytical velocity profiles for the axisymmetric Couette-Flow with $\omega_1 = \omega_2 = 10$ Hz.

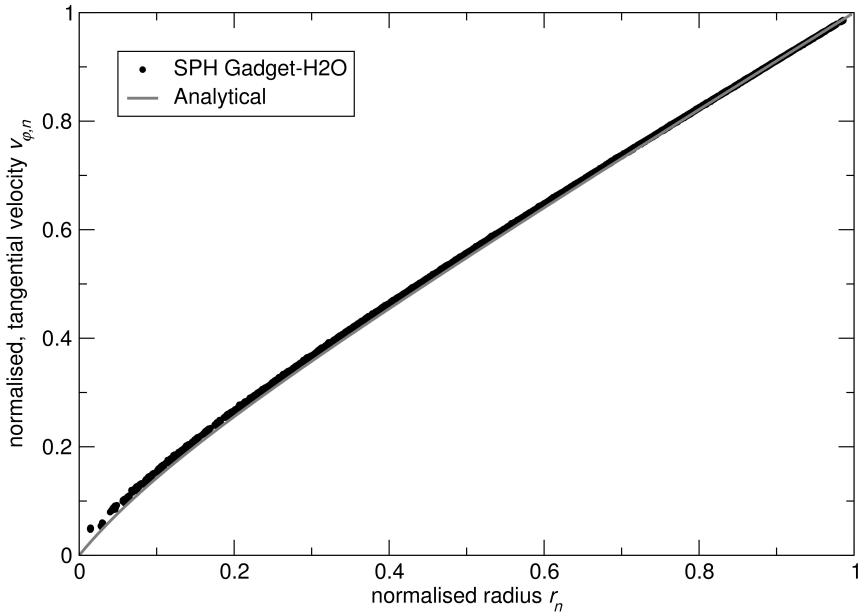

Figure 8.8: Predicted and analytical velocity profiles for the axisymmetric Couette-Flow with $\omega_1 = 0$ Hz and $\omega_2 = 10$ Hz.

8.2 Soil motion

The following validation exercise is devoted to the performance of the employed soil models. Depicted studies refer to two similar examples of a collapsing single-phase soil block. A generic case is initially discussed with respect to the principal features of the soil models. Subsequently, an experimentally investigated case is computed to validate the combined solid/fluid model.

8.2.1 Generic case

The two-dimensional case illustrated in Fig. 8.9 is used to analyse the characteristics of the different soil-stress models. It refers to an initially supported granular material block of 0.04 m x 0.04 m which is discretised by 20 x 20 particles. The properties of the investigated soil are described by Tab. 8.2. Collapse simulations were performed with the viscoplastic (vp), the limited viscoplastic (lvp), the elastic (el) and the combined solid/fluid (csf) soil model (cf. chapter 4.2 for a detailed description of the different approaches). The viscosity limit was assigned to the general value of $\mu_{max} = 150$ Pa $\cdot$ s.

Table 8.2: Details of the examined single-phase soil collapse cases.

	ρ_s[kg/m^3]	E[Pa]	C[Pa]	ϕ [°]	ν[1]
Generic soil collapse case	1500	$3.0 \cdot 10^5$	0	31.0	0.3
Soil collapse case [13]	2650	$8.4 \cdot 10^5$	0	19.8	0.3

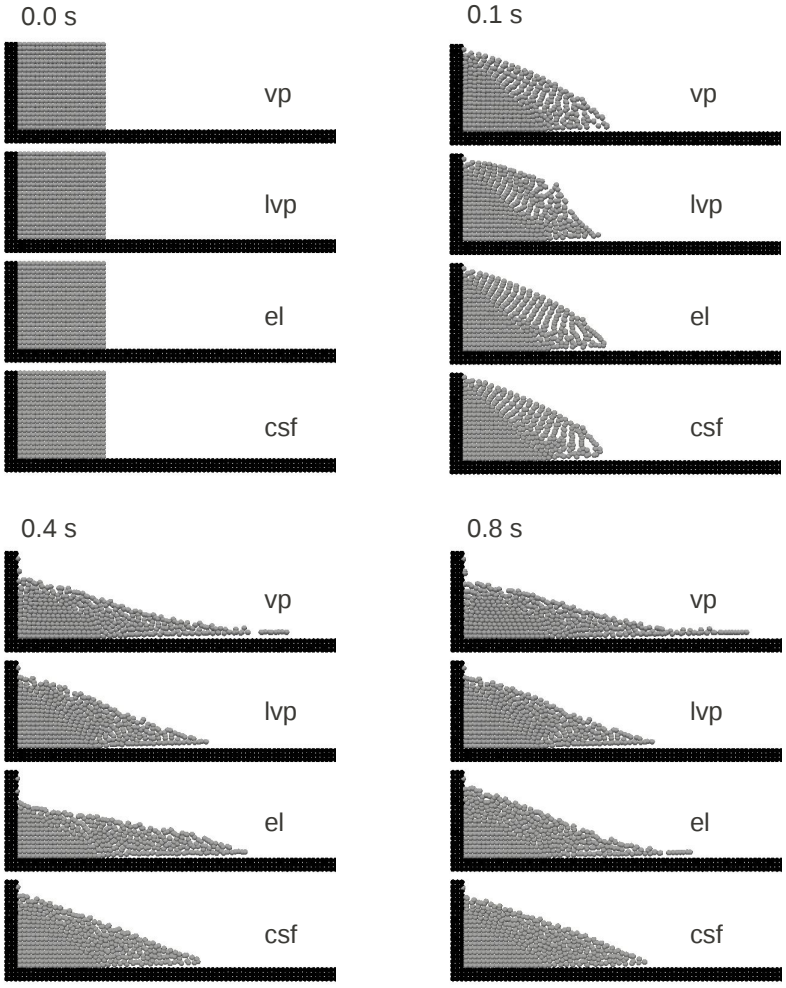

Figure 8.9: Behaviour of viscoplastic (vp), limited viscoplastic (lvp), linear elastic (el) and combined solid/fluid (csf) soil models for a generic soil collapse.

As indicated by Fig. 8.9, the limited viscoplastic, linear elastic and combined solid/fluid models return a similar final slope. In contrast to this, the viscoplastic soil model displays a pronounced creeping that does not lead to a steady final state. A drawback of the elastic model is related to an excessive swinging motion (cf. t=0.4 s and t=0.8 s) due to strong

memory effects. Compared to the other models, the limited viscoplastic approach shows a different surge front development, as depicted by the snapshot at t=0.1 s. Its overall performance is, however, still comparable to the combined solid/fluid approach. The discussion of the subsequent validation case is thus confined to the limited viscoplastic and the combined solid/fluid model.

8.2.2 Validation case

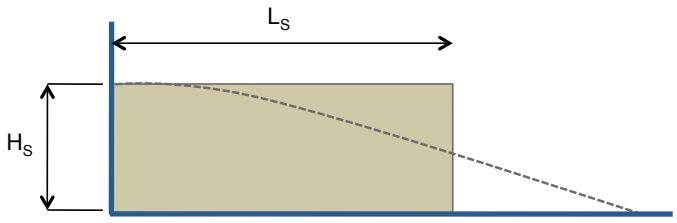

Figure 8.10: Sketch of the set-up for the soil collapse validation test.

The second 2D soil collapse case refers to an experiment published by Bui et al. [13]. Results obtained from the limited viscoplastic and the combined solid/fluid soil models are compared with experiments and SPH simulations of Bui et al. [13]. Small aluminium bars were used to represent the granular material in the experiment and simultaneously ensure two-dimensionality. Figure 8.10 illustrates a sketch of the initial configuration. The utilized bars have a length of 0.05 m. They span 0.0015 m and 0.001 m in diameter. The ensemble is positioned in a laterally restricted channel forming an initial block of length L_s = 0.2 m and height H_s = 0.1 m.

The properties of the cohesionless aluminium bars are described by Tab. 8.2. The employed 2D discretisation is based upon 5000 particles with an initial spacing of $\Delta_p = 0.002$ m. Attention is directed to the influence of the threshold-viscosity value on the predictive performance. Several maximum viscosities μ_{max} between 175 to 1500 Pa · s are considered for the limited viscoplastic simulations, while only the upper and lower limits of 175 and 1500 Pa · s are used in conjunction with the combined solid/fluid approach.

Figure 8.11 compares experimental results reported by Bui et al. [13] and SPH prediction from the present study using the limited viscoplastic and the combined solid/fluid model. The figure indicates a satisfactory level of agreement for both SPH simulations utilizing a threshold viscosity value of 1500 Pa · s. Differences to the experiments can be

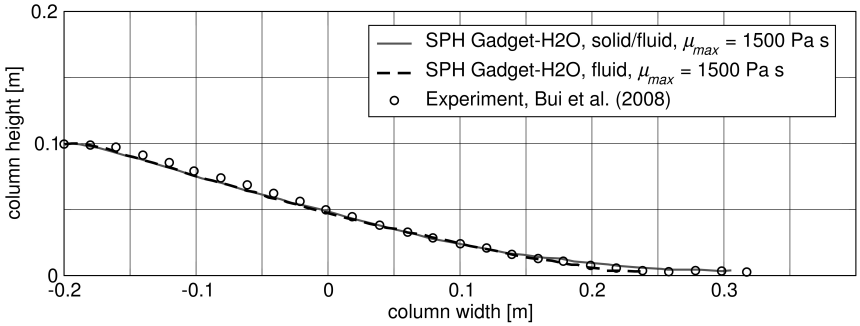

Figure 8.11: Final profiles for the soil collapse test. Results obtained by GADGET-$^{H}2^{O}$ are compared to numerical and experimental results from Bui et al. [13].

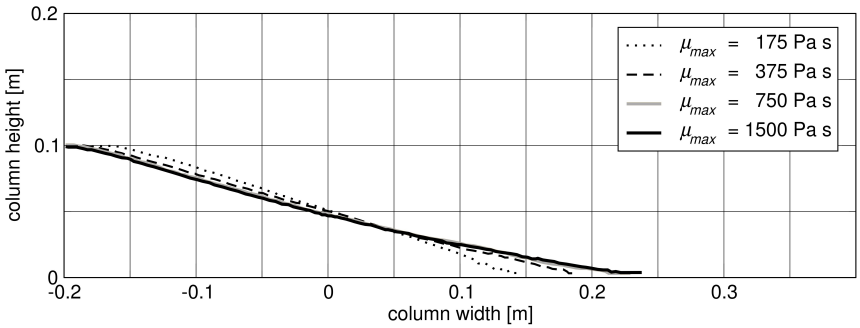

Figure 8.12: Final profiles for the soil collapse test. Results obtained from the limited viscoplastic approach with different maximum soil viscosities are compared.

observed in the upper part of the slope where both models of the present study yield a small over-prediction of material motion. Nevertheless, results illustrate that the rather simple Mohr-Coulomb criterion at the root of the present study can reproduce the principal behaviour of the granular soil. An interesting point is related to the influence of the applied threshold viscosity. Results shown in Fig. 8.12 indicate negligible changes beyond $\mu_{max} \geq 750$ Pa $\cdot$ s in conjunction with the limited viscoplastic model. Below this value, the attainable predictive accuracy is significantly reduced. Such sensitivities are not observed using the combined solid/fluid model as documented by Fig. 8.13 which compares results obtained from $\mu_{max} = 175$ Pa $\cdot$ s and $\mu_{max} = 1500$ Pa $\cdot$ s. The predicted final slopes are almost indistiguishable and display a good agreement with experiments. Minor deviations refer to the run-out length which is slightly underpredicted for $\mu_{max} = 175$ Pa $\cdot$ s. The combined solid/fluid soil model thus offers promising results for single-phase soil predictions and obviates algorithmic disadvantages of the other investigated models.

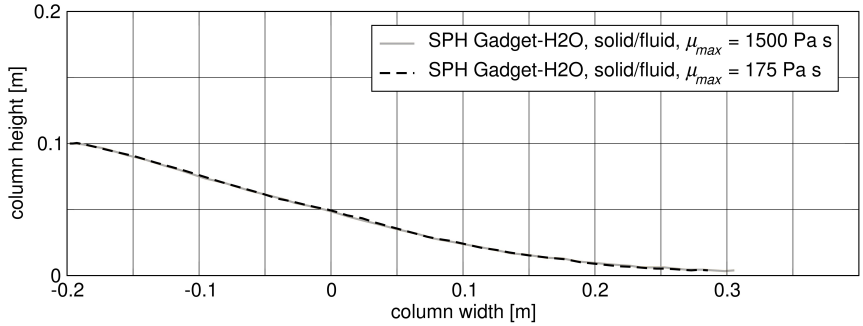

Figure 8.13: Final profiles for the soil collapse test. Results obtained from the combined solid/fluid approach with different maximum soil viscosities are compared.

8.3 Water/soil-interaction

Two different test-cases are meant to scrutinise the water/soil-suspension model and the approach for porous media with saturation dependent cohesions. A two-phase dam break experiment represents the reference to study erosional mechanisms whereas seepage flow induced failures are examined by comparing SPH data to a river embankment model test.

8.3.1 Erosional dam break

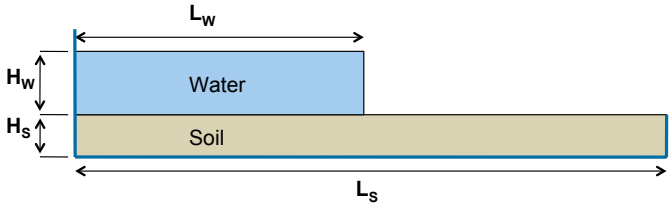

Figure 8.14: Schematic sketch of the Louvain erosional dam break experiment [25].

The first water/soil-interaction test-case focuses upon the *Louvain* experiment published by Fraccarollo and Capart [25]. The experiment consists of a collapsing water column placed above a bed of cohesionless granular soil. The collapsing water column erodes the soil and a water/soil suspension layer develops between the pure fluid and pure granular regimes. Figure 8.14 provides a schematic overview of the initial set-up. The water column features the dimensions $L_w = 1$ m and $H_w = 0.1$ m and is placed above a granular bed of $L_s = 2$ m and $H_s = 0.06$ m. The soil material consists of PVC pellets with a density of 1540 kg/m^3. The approximate porosity reads $\varphi = 0.3$, hence the density of the saturated model soil is assigned to $\rho_s = 1378$ kg/m^3. Further details of the materials are given in

Table 8.3: Details of the examined erosional dam break validation cases.

	$\rho_{\mathbf{s}}$	E	C	ϕ	ν	φ	$\rho_{\mathbf{f}}$	$\mu_{\mathbf{f}}$	μ_{max}
	[kg/m^3]	[Pa]	[Pa]	[°]	[1]	[1]	[kg/m^3]	[Pa · s]	[Pa · s]
Louvain test-case	1378	8.4·10^5	0	31.0	0.3	0.3	1000	0.001	1500

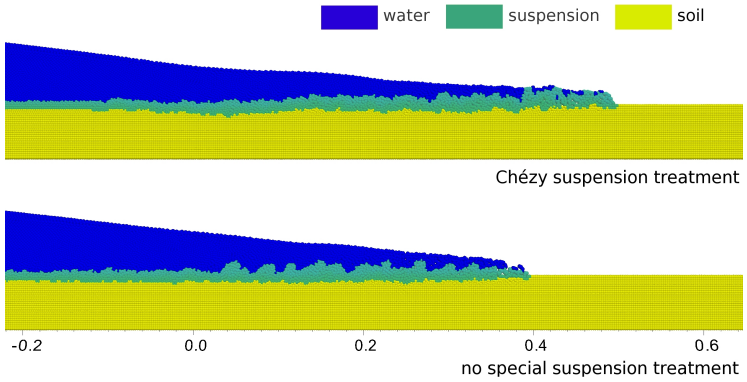

Figure 8.15: Comparison between two different simulations for the Louvain test-case [25]: the upper picture shows a simulation with suspension model whereas the lower picture represents the same instant with disabled suspension treatment.

Tab. 8.3.

Three different 2D SPH discretisations with particle spacings of 0.0025 m, 0.005 m and 0.01 m are used in this study. In the following, it will be referred to them as *fine*, *medium* and *coarse*, respectively. The friction coefficients C_f for the suspension is assigned to $C_f = 0.01$. Generally, a threshold soil viscosity $\mu_{max} = 1500$ Pa · s is applied. The following comparison between experimental and numerical results includes the position of the progressing surge front as well as the evolution of material interfaces. Furthermore, a parameter study is performed to assess the influence of different particle resolutions.

An important result of the study is shown in Fig. 8.15 which illustrates the influence of the suspension treatment. The two pictures show snapshots of the fine resolution SPH simulations at 0.5 s. Two different simulations are depicted: the upper picture refers to a Chézy-suspension treatment while the lower picture is related to a simulation without a special suspension model. The propagation velocity of the surge front is obviously lower for the standard approach and the erosion pattern is more pronounced for the Chézy-

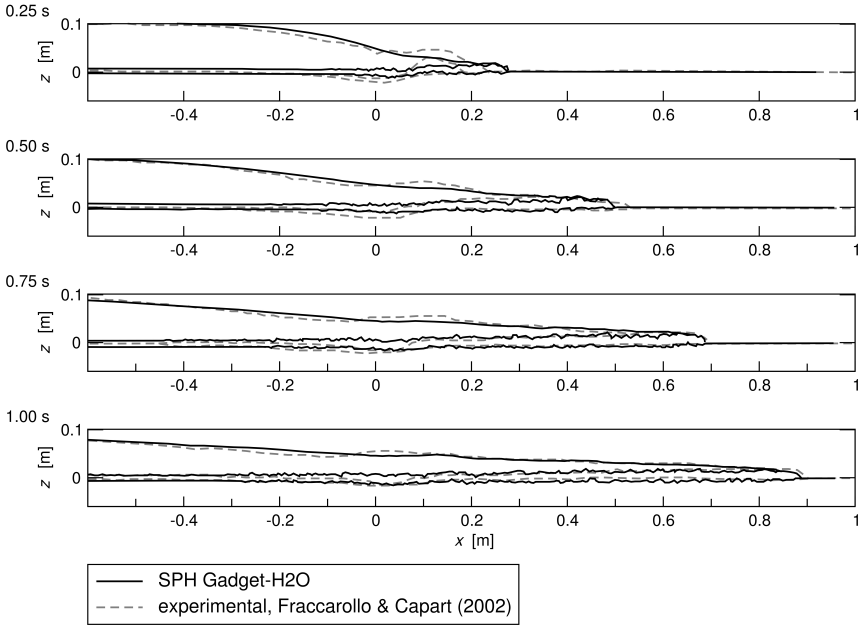

Figure 8.16: Contours of the phases interfaces for the wetted surface, water/suspension and suspension/pure-soil. The black lines represent the SPH results, the dashed grey lines show the experimental results by Fraccarollo and Capart [25].

suspension treatment which captures the thickness of the suspension layer, defined by $0 < \tilde{c}_{\mathbf{s}} < 1$, remarkably well as shown in the Fig. 8.16.

Figure 8.16 displays the evolution of the predicted interfaces using the Chézy-suspension treatment together with the fine resolution in comparison to experimental data at four different points in time. The simulations match the measured interface-contours quite well. Deviations, both in the interfaces and the surge front, are seen for the earlier time instant $t = 0.25$ s. They are attributed to effects being related to experimental details – such as the opening of a gate – that are not captured by the simulation. The overall agreement is nonetheless satisfactory, especially for $t \geq 0.5$ s.

The progression of the surge front is also outlined by Fig. 8.17. The figure supports a direct comparison of the present SPH results using the suspension treatment with the experimental results of Fraccarollo and Capart [25]. Attention is given to the influence of resolution aspects. A fair agreement is obtained for all three resolutions during the early phase of the collapse. An influence of the particle resolution is anticipated for the suspension model since it affects the computation of the volumetric concentration. A thicker initial interaction layer is expected if the resolution becomes coarser and thus influences the predicted erosion and delays the downstream propagation of the surge front. Figure 8.18 describes the early erosional mechanism as returned by the three resolutions. Mind

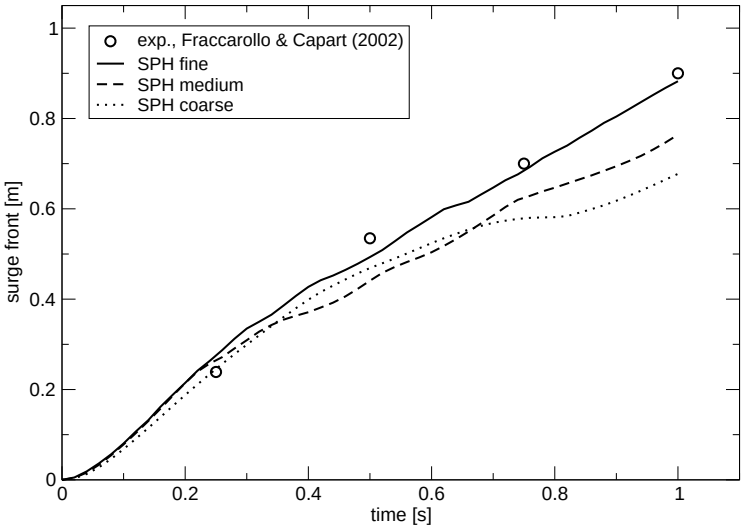

Figure 8.17: Surge fronts for the Louvain test-case for different particle resolutions.

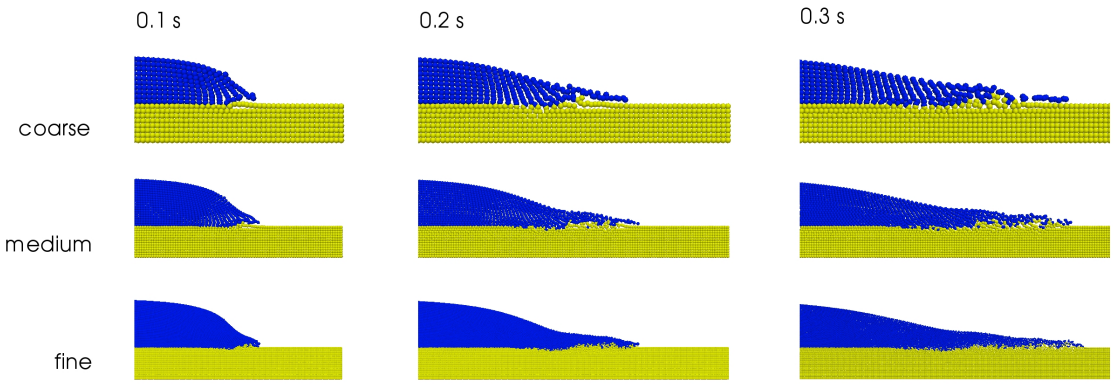

Figure 8.18: Erosional mechanism predicted by different particle resolutions.

that the suspension layer is not separately coloured to give a better impression of the initial erosion. At a later stage, the medium and coarse resolution surge fronts start to lag behind until they get significantly slower than in the fine resolution case. This suggests that the resolution dependency increases when the pure water layer becomes thinner.

8.3.2 Saturation driven embankment failure

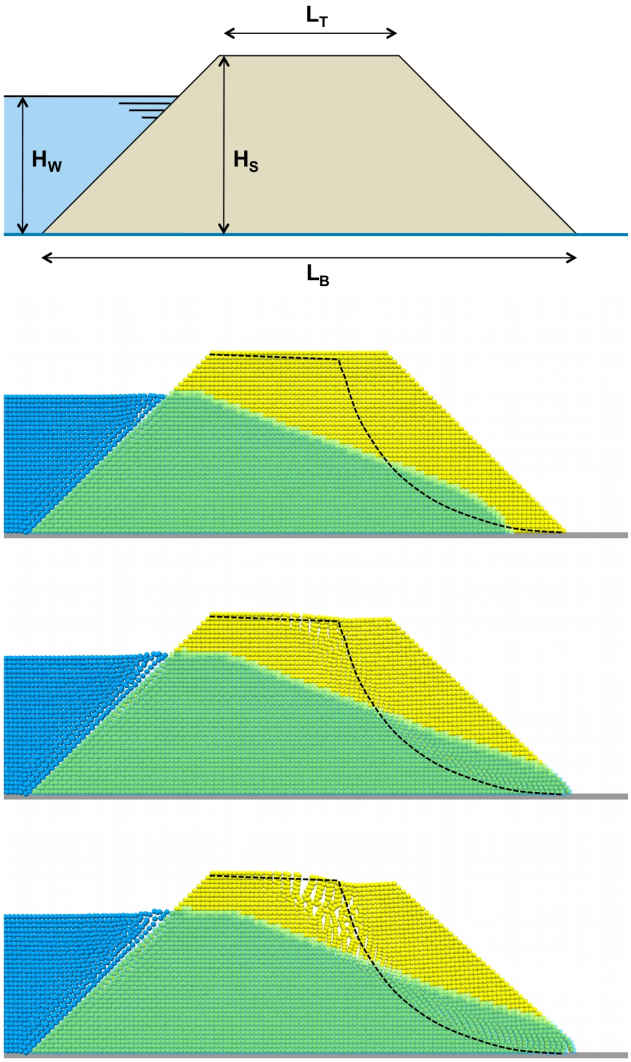

Figure 8.19: Sketch of the initial set-up of the river embankment test-case and progressing failure. The experimental failure line [14] is marked with the black dashes.

Bui et al. [14] have published a model-scale experiment on the progressive failure of a river embankment due to a reduced soil strength at a fully saturated state. The test-case is used in the present study to evaluate the performance of the partly saturated soil model. Figure 8.19 provides an overview of the two-dimensional test-case. The model embankment is of trapezoid shape with the base lengths $L_T = 0.4$ m and $L_B = 0.8$ m and a height of $H_s = 0.4$ m. A watercolumn with $H_w = 0.3$ m is initially wetting the construction. The model soil features a friction angle of $31.2°$, a density of 1560 kg/m^3, an initial cohesion of $C_{dry} = 550$ Pa, a Young's modulus of $E = 3 \cdot 10^6$ Pa and a Poisson

ratio of $\nu = 0.3$. The porosity values in the simulation read $K = 3 \cdot 10^{-9}$ m^2, $\varphi = 0.5$, $B_{cap} = 100$ Pa and $\alpha_{cap} = 0.1$. Fully saturated soil particles are assigned to zero cohesion. The applied particle spacing of 0.01 m leads to an overall number of 3280 soil and 420 water particles.

Due to the reduction of the effective cohesion, material failure sets in right after the inland foot of the embankment is reached by the pore-water front as illustrated in Fig. 8.19. A sickle-shaped failure line develops from the foot to the dike top. On the inland side of this failure line, an almost undeformed block of soil is sliding downwards. The predicted failure progression coincides fair with the experimentally evaluated behaviour indicated by the dashed line in Fig. 8.19, although tensile instability effects are seen at the final stage along the intersection of the crest with the failure line.

8.4 Pressure evaluation

The prediction of pressure fields for static and dynamic scenarios is examined in the following section. Emphasis is given to the assessment of density and pressure smoothing operations.

8.4.1 Hydrostatic two-phase case

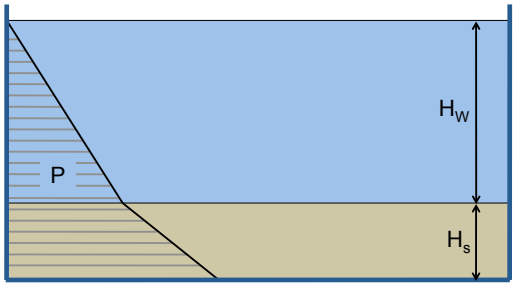

Figure 8.20: Sketch of the hydrostatic test-case.

The performance in hydrostatic cases is verified by a simple two-phase hydrostatic stratification example as illustrated in Fig. 8.20. Accordingly, a two-dimensional basin of 1.1 m x 2.0 m (height x width) is filled with a 0.35 m thick soil layer located underneath a 0.75

m deep water column. The material properties of the soil and water phase follow from Tab. 8.4.

Table 8.4: Details of the two phases hydrostatic verification case.

	$\rho_{\mathbf{s}}$ [kg/m^3]	E [Pa]	C [Pa]	ϕ [°]	ν [1]	φ [1]	$\rho_{\mathbf{f}}$ [kg/m^3]	$\mu_{\mathbf{f}}$ [Pa · s]	μ_{max} [Pa · s]
Hydrostatic case	2000	8.4·10^5	0	31.0	0.3	0.0	1000	0.001	1500

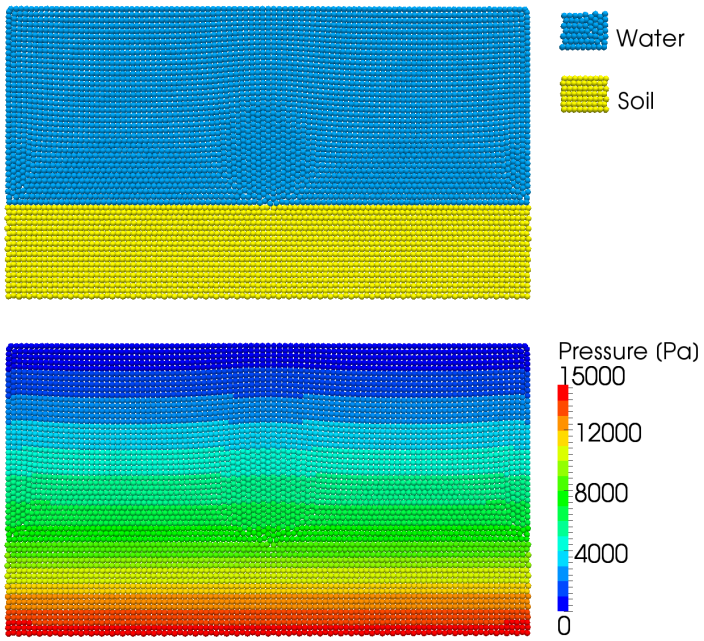

Figure 8.21: Hydrostatic test-case: the upper picture shows the particle distribution after 5 s simulation time. Hydrostatic pressure for the same instant is displayed in the lower picture.

An initial particle spacing of 0.02 m leads to 1818 soil and 3838 water particles. The particle motion is damped within the first 0.5 s according to Eq. (7.34) with a damping coefficient $c_d = 25$ s^{-1} in order to reduce oscillating effects due to the initial loading by gravity. Figure 8.21 depicts the particle distribution and the pressure field obtained after 5 seconds of simulation time. A smooth pressure profile can be observed that is not disturbed at the water/soil interface. A direct comparison between the predicted and the analytical solution is given by Fig. 8.22. The figure shows an encouraging agreement, with the little

difference that the discontinuity of the density and pressure gradient along the interface is slightly smoothed by the SPH-solution due to the density blending approach (7.30).

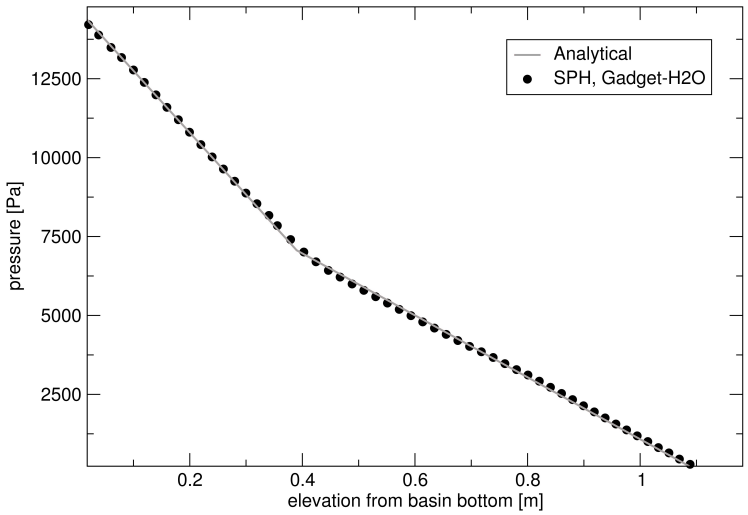

Figure 8.22: Hydrostatic test-case: pressure predicted by GADGET-$^{H}2^{O}$ is compared to the analytical solution.

8.4.2 Wedge impact

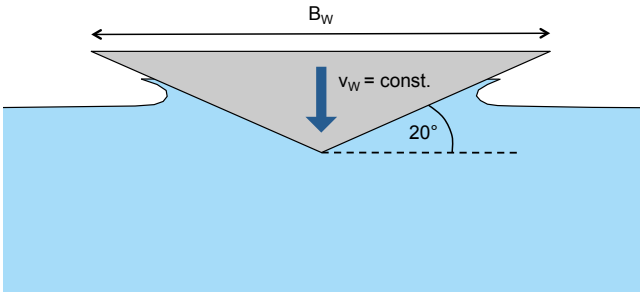

Figure 8.23: Sketch of the wedge impact test-case.

The impact of a two-dimensional wedge into water reported by Zhao and Faltinsen [115] is a widely used benchmark case for the prediction of pressure dynamics. Figure 8.23 illustrates the basic set-up. A wedge with the total width B_W symmetrically hits the still water surface with a constant velocity v_W. Zhao and Faltinsen [115] consider different deadrises at the wedge's tip. The test-case is particularly challenging for obtuse angles due to the increasing contribution of compressible effects. A deadrise of $20°$ is applied in the present study to allow for a performance analysis of the WCSPH pressure evaluation.

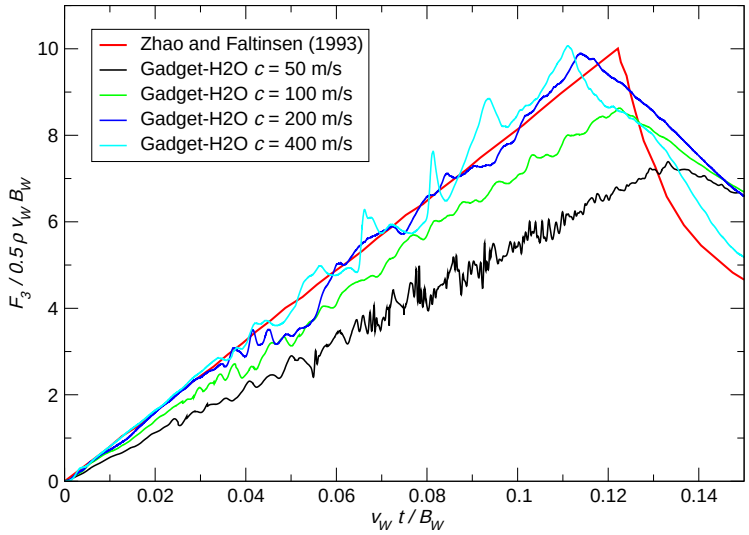

Figure 8.24: Wedge impact test-case with fine resolution: vertical force on the wedge for different predefined sound-speeds. Results are compared to a BEM solution by Zhao and Faltinsen [115].

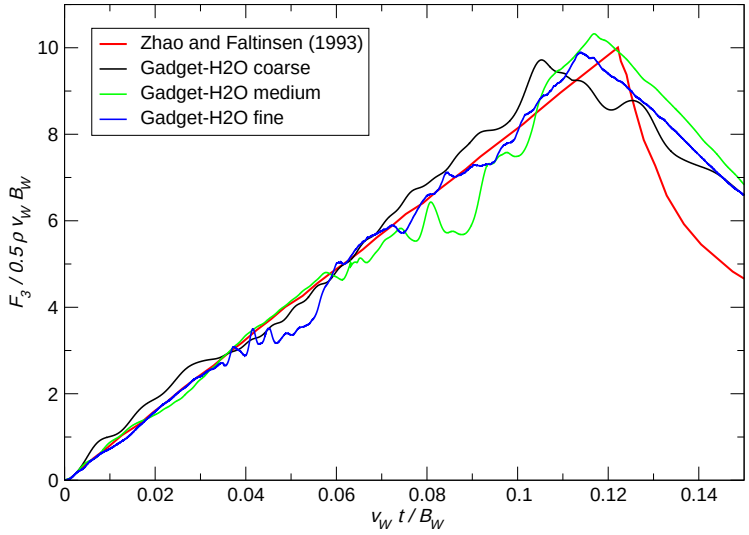

Figure 8.25: Wedge impact test-case with $c = 200$ m/s: vertical force on the wedge for different particle resolutions. Results are compared to a BEM solution by Zhao and Faltinsen [115].

The wedge features a width of 5.5 m and hits the water with 5 m/s impact velocity. The basin dimensions read 15 m x 15 m (depth x width). Three different particle spacings with 0.1, 0.05 and 0.025 (*coarse*, *medium* and *fine*) are investigated to assess resolution dependencies. For the investigated problem, a certain sound speed sensitivity is expected. Therefore, a range of sound speeds from 50 - 400 m/s is considered for a sensitivity study.

Figures 8.24 and 8.25 show the normalised vertical force acting on the wedge plotted over the normalised time after the initial water contact. The simulations are performed

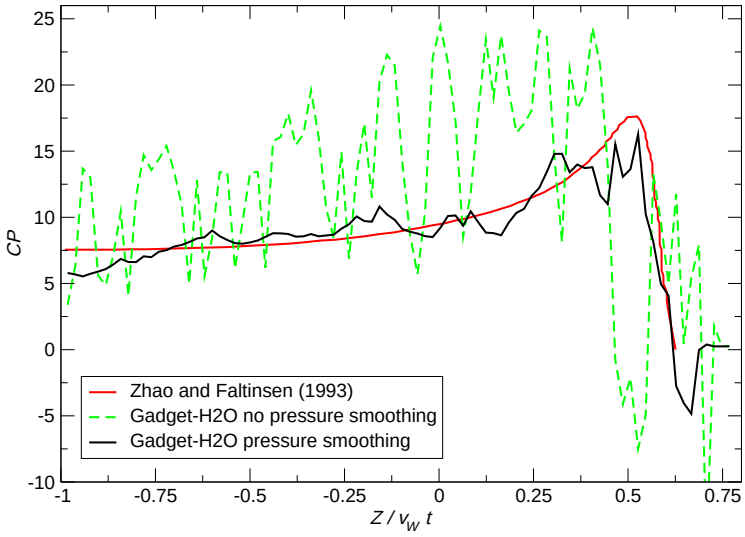

Figure 8.26: Pressure coefficient on the wedge for the fine particle resolution with and without pressure smoothing. Results are compared to a BEM solution by Zhao and Faltinsen [115].

with applying the standard smoothing schemes for velocity and pressure fields described in section 7.3.2.

A significant influence of the sound speed settings is depicted in Fig. 8.24. Following Eq. (3.47), a first estimate for the sound speed is given by $c = 10v_W = 50$ m/s. Unfortunately, this leads to a strong underprediction of the vertical force. Satisfying force magnitudes are obtained for sound speed values of 200 m/s and above. This behaviour can be explained by increased local fluid velocities at a range of approx. 20 m/s during the impact. The results also indicate that too large sound speed values might lead to numerical problems like the oscillating behaviour obtained for $c = 400$ m/s. Concerning resolution sensitivities, only small deviations between the three different discretisations can be observed as depicted in Fig. 8.25. The three displayed resolutions are related to a sound speed of $c = 200$ m/s. Regarding the integral on the wedge, this result is very encouraging as it indicates the applicability of SPH to impact problems with engineering accuracy even using rather coarse resolutions which significantly decreases the overall number of particles and therefore the computational time for full-scale applications.

Generally, a comparison of results to a fully non-linear BEM simulation by Zhao and Faltinsen [115] reveals a satisfactory agreement. Some deviations can be observed especially when the wedge is fully submerged. At this instant, SPH predictions of the drop of the vertical force do of course not follow the BEM solution since separation effects are not captured by the regarded potential flow BEM approach. However, the oscillating be-

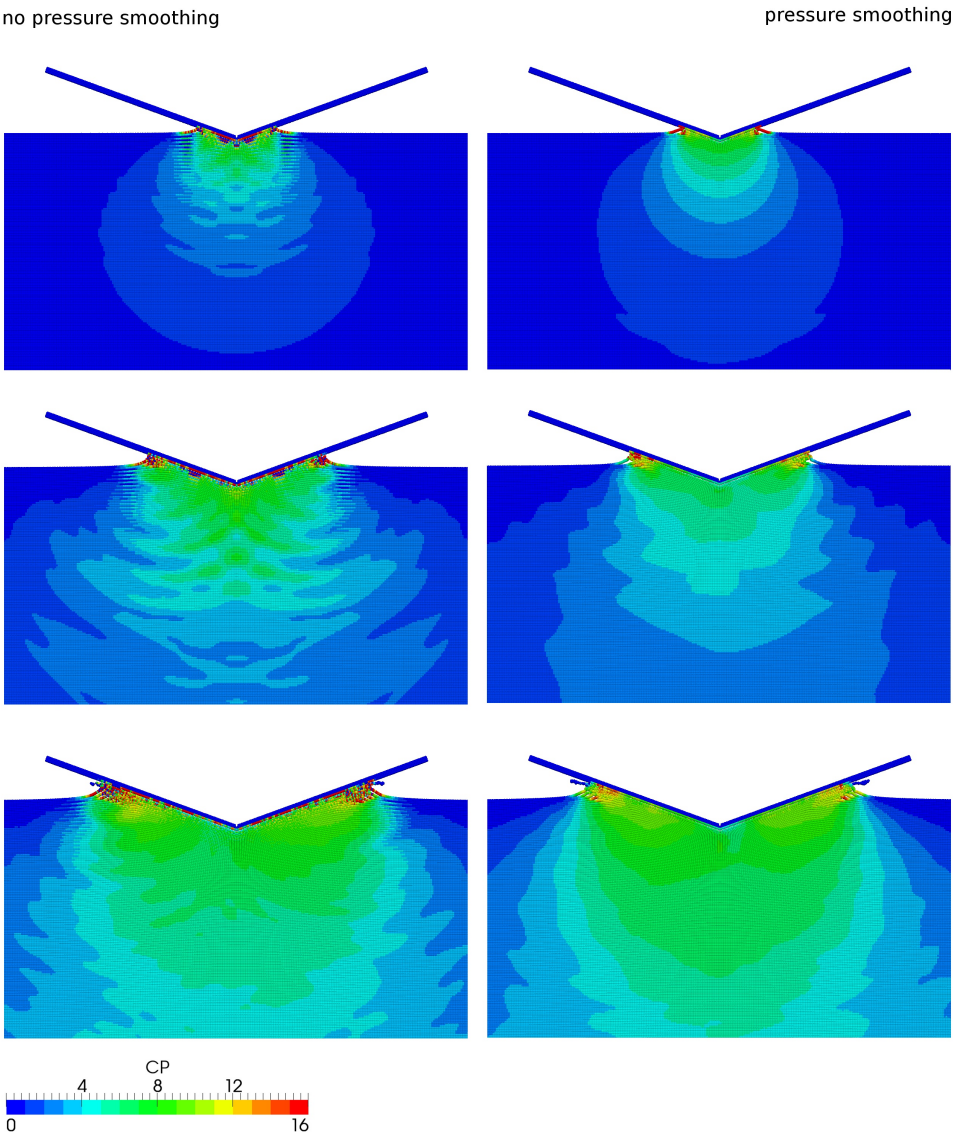

Figure 8.27: Pressure coefficient on the wedge and within the water during impact. Simulations with pressure smoothing are compared to those without.

haviour of the force during the impact can be considered a systematical drawback of the applied WCSPH approach. The overall quality of results is in the same range as reported for similar weakly compressible procedures [75].

Figures 8.26 and 8.27 illustrate the favorable influence of the pressure field smoothing outlined in section 7.3.2. Figure 8.26 shows the distribution of the pressure coefficient $CP = p/(0.5\rho v_W^2)$ along the leg of the wedge whereas Fig. 8.27 provides contour plots for CP at different instants. Both figures indicate significant predictive improvements and a strong noise reduction if the pressure smoothing is applied.

8.5 Variable resolution

The variable resolution approach is tested by a hydrostatic case and a dynamic tank sloshing example. Attention is paid to the influence of ∇h terms and discretisation alternatives. Finally, the reduction of computational time is evaluated.

8.5.1 Hydrostatic tank simulation

The first verification case elucidates the importance of ∇h-contributions to ∇W. It refers to a 2D basin, which is $H_y = 15$ m deep and $B_x = 32.6$ m wide. The liquid volume is exclusively subjected to gravitational forces in y-direction and pressure. The initial transient is smoothed according to section 7.4 for the first 5 s.

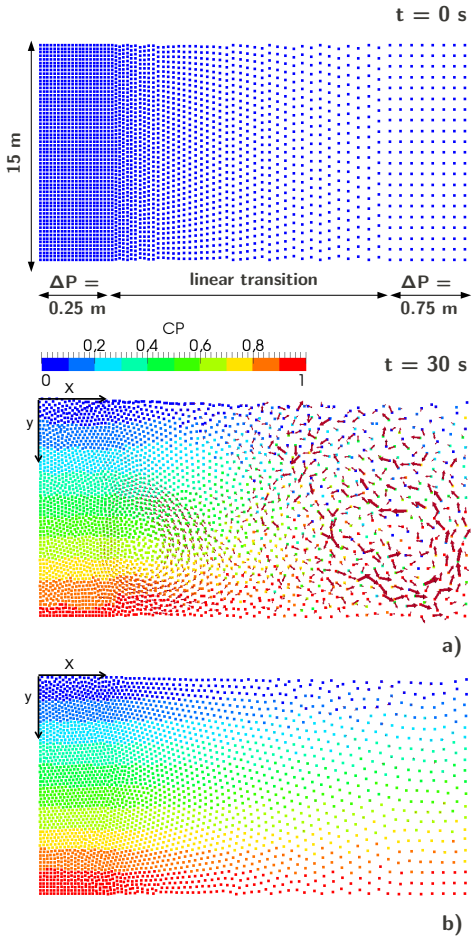

Figure 8.28: Hydrostatic test-case simulated with a variable-particle resolution. The upper figure shows the initial particle spacing. The centre figure depicts the pressure profile and velocity vectors after 30 s simulation time for a simulation without the ∇h-contributions to ∇W, the lower figure refers to the analogue simulation with ∇h-contributions after 30 s.

The particle spacing at the left border is assigned to $\Delta_p = 0.25$ m. An 18.5 m long transition zone bridges towards the final spacing $\Delta_p = 0.75$ m. Within the transition zone, particle spacings occur which cannot be multiplied to exactly fit the same initial water height. This yields a slightly uneven initial free surface, as illustrated in the upper part of Fig. 8.28. Results of two simulations, i.e. with and without the inclusion of the ∇h-contributions to ∇W in Eq. (7.18), are presented in the lower two subfigures of Fig. 8.28. Both depict the flow field obtained after 30 s simulation time. Particles are coloured according to the normalised hydrostatic pressure $CP = p/(\rho\, g\, y)$. Vectors indicate the particle velocities and employ an identical scaling for both pictures. It can clearly be observed that the ∇h-terms significantly improve the predicitive performance and should be included. While the pressure and velocity fields are quite noisy neglecting the ∇h-contributions, a smooth pressure distribution and no spurious velocities are obtained if the terms are considered. A horizontal free surface only settles when ∇h-terms are considered.

8.5.2 Tank sloshing

The capability of reproducing convective flows that travel through areas with a variable resolution is analysed in the second case. The 2D example refers to laminar-sloshing simulations for a 1 m $\times 1$ m tank. The free surface is initialised by an 0.2 m high sinusoidal wave, i.e.

$$y = 1 - 0.1 \sin\left[(x - 0.5)\pi\right]. \tag{8.2}$$

The initial configuration is illustrated in Fig. 8.29. The dynamic viscosity is assigned to $\mu = 1$ Pa s. VoF-simulations are performed applying TUHH's in-house code FreSCo$^+$ for comparison. Supplementary to a homogeneous discretisation, two different coarsening/refinement scenarios are investigated. The initial mass and particle distributions of both variable resolutions are indicated by Fig. 8.30. The left part depicts a discretisation with one transition from $\Delta_p = 0.008$ m to $\Delta_p = 0.012$ m over the lower 0.708 m of the domain. The second case (Fig. 8.30; right) uses two transition zones: the first one increases the particle spacing from $\Delta_p = 0.008$ m to $\Delta_p = 0.009$ m in negative y-direction, subsequently a more keen increase to $\Delta_p = 0.02$ m is performed in the lower 0.356 m of the domain. Figure 8.31 depicts the streamlines after a quarter of one wave period. The figure reveals that particles are convected into the variable-resolution region(s) and also return from there owing to the orbital motion. The continuous property change along the

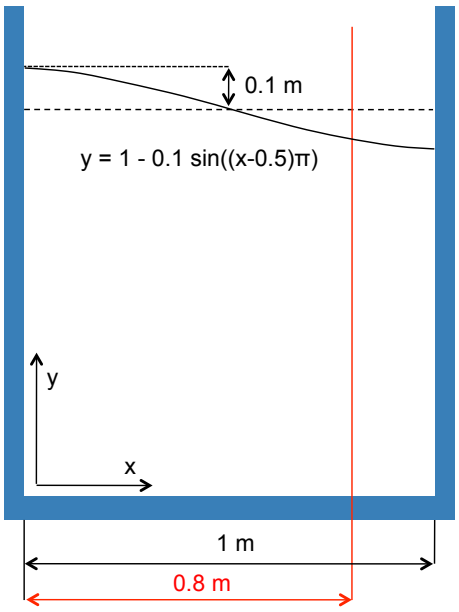

Figure 8.29: Sketch of the basic set-up of the tank-sloshing simulation.

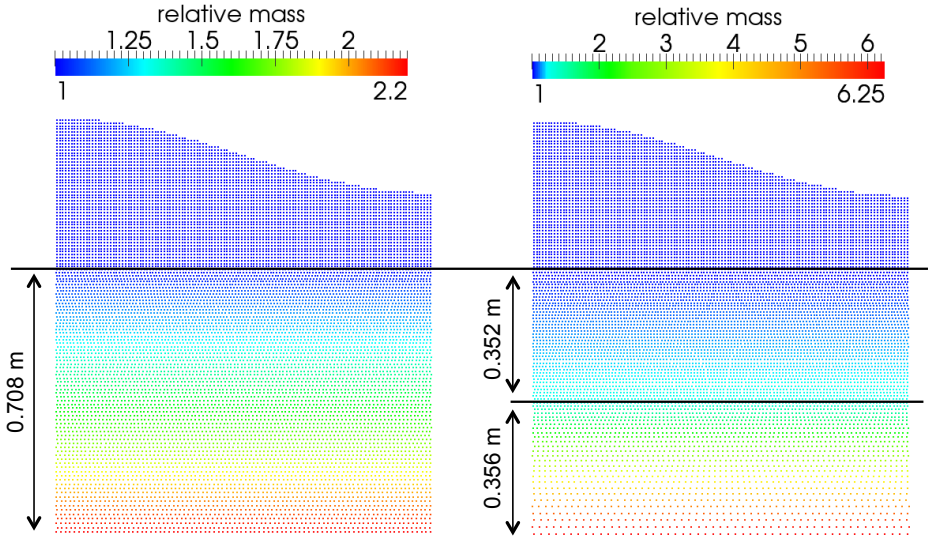

Figure 8.30: Variable resolutions considered for the tank-sloshing case. The left picture illustrates a discretisation with one transition, the right one shows two transitions with different gradients. The particles are coloured according to their relative mass, normalised with respect to the smallest particle mass.

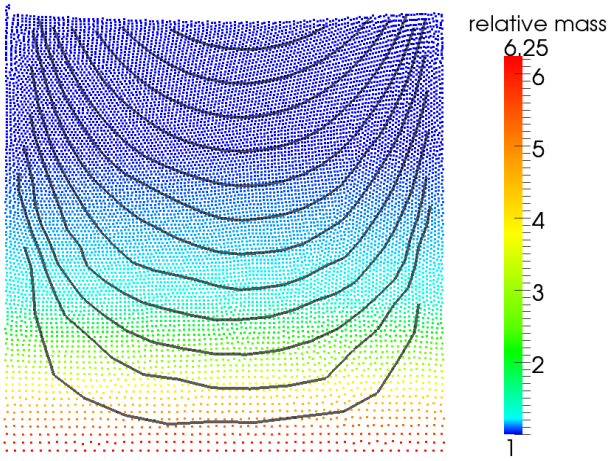

Figure 8.31: Streamlines of the tank sloshing case after a quarter of one wave period. The picture shows the discretisation with two linear transitions. The particles are coloured according to their relative mass, normalised with respect to the smallest particle mass.

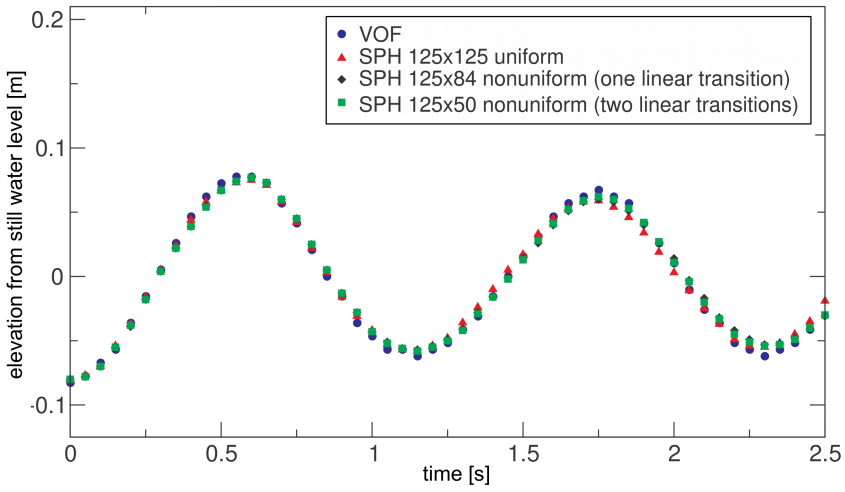

Figure 8.32: Free surface elevation in the sloshing tank at $x = 0.8$ m predicted by three different SPH simulations (one uniform and two nonuniform resolutions) and a VoF simulation.

Table 8.5: Relative computational time for different single-core validation simulations. Times and particle numbers are normalised with respect to the uniform reference case.

validation case	particles	particles (relative)	comp. time (relative)
static, uniform	8152	1	1
static, variable	3456	0.424	0.421
sloshing, uniform	17185	1	1
sloshing, variable 1	13304	0.774	0.789
sloshing, variable 2	12728	0.741	0.771

pulsating orbital motion and the related error accumulation denotes the specific challenge of this case. Results are evaluated by the evolution of the local free-surface elevation at $x = 0.8$ m. As indicated by Fig. 8.32, the result of the uniform SPH discretisation is very close to the VoF solution. The two variable SPH resolutions generally display a satisfactory result. A small shift in the wave's phase can be observed for both variable resolutions compared to the uniform one. This is due to the redistribution of momentum when particles change their mass, which alters the orbital velocity and the phase contrary to the traveling wave direction.

8.5.3 Comparison of CPU effort

The main goal of the variable resolution approach is to save computational time compared to uniform settings. The single-core effort of the two test-cases is listed in Tab. 8.5. It can be seen that the effort scales linearly with the amount of particles and the amount of transition zones is irrelevant.

8.6 Floating body motion

For the evaluation of floating body motion predictions, the 6DOF motion solver in conjunction with the variable-resolution scheme and a uniform discretisation is applied to study the behaviour of a cube impacting into a water tank. The edge length of the cube are $e = 0.15$ m, the dimensions of the tank read 0.25 m depth $\times$ 1 m width $\times$ 1 m length. Notice that the lateral and bottom boundaries of the tank refer to walls in accord with the experiment reported by Kraskowski [40].

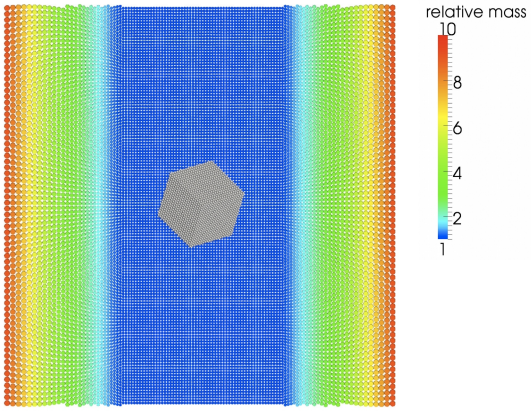

Figure 8.33: Top view of the initial set-up for a cube impacting into a water basin with variable particle resolution.

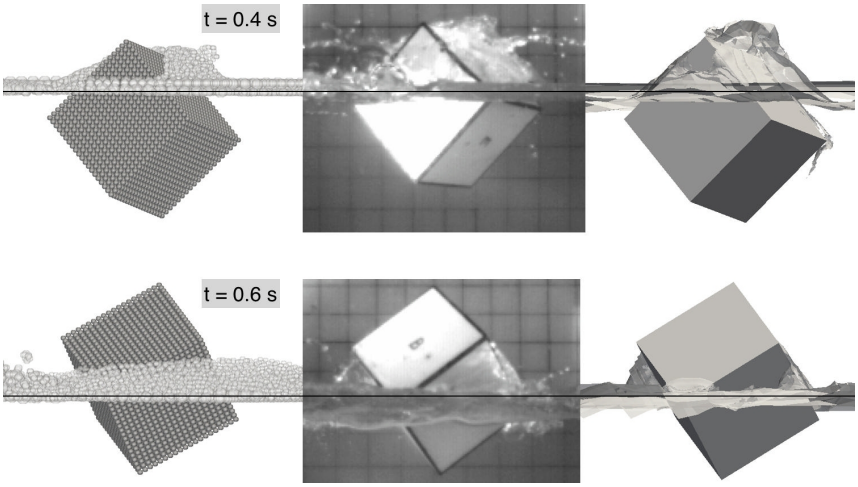

Figure 8.34: Comparison of cube position and orientation for different points in time. The left pictures refer to SPH simulations, the middle ones depict experimental photographs by Kraskowski [40] and the right pictures show snapshots from VoF simulations.

The cube's centre of gravity is deplaced by 7 mm to one side which activates a complex angular (roll-over) motion inside the water. SPH results are compared with images of Kraskowski [40] and VoF-simulations with FRESCO$^+$ on a 650k cells mesh using local-grid refinement. SPH simulations are performed with a homogeneous particle spacing of 0.007 m and a corresponding total number of 860k particles. Additionally a variable-resolution setup using 520k particles is investigated. As depicted by Fig. 8.33, the particles' mass is increased by a factor of 10 over the final 0.3 m in lateral direction. The floating-body

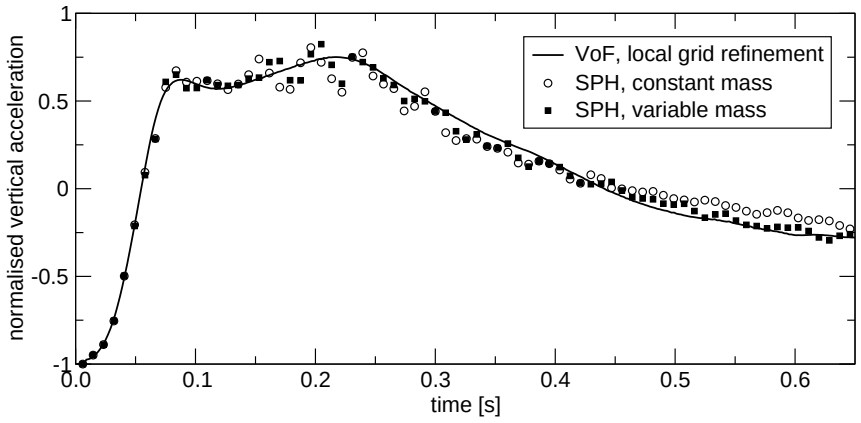

Figure 8.35: Vertical accelerations imposed on the cube obtained from the SPH- and VoF-simulations. Accelerations are normalised by gravitational acceleration.

motion is computed using the quaternion-based motion modeller for both the mesh-based VoF approach and the SPH approach, employing the forces imposed on the cube. The mesh-based simulations used an implicit coupling between the motion modeller and the fluid solver whereas the SPH simulations refer to an explicit coupling. Fig. 8.34 reveals a remarkable agreement between both simulations and experimental observations for two time instants, i.e. $t = 0.4$ s and $t = 0.6$ s after the first contact of the cube with the free surface. Fig. 8.35 compares the predicted vertical accelerations returned by the VoF and the SPH method. Again an encouraging predictive agreement is seen. The slight differences between the variable and uniform SPH simulations after 0.42 s are expected to occur due to a damping of reflected waves by the coarser resolution in line with locally coarsened VoF-simulations.

8.7 Discussion of results

Each of the test-cases presented serve for the validation of essential individual functionalities which are relevant for the simulation of complex harbour hydrodynamic problems. The test-cases should ideally be governed by the scrutinised phenomena whilst still being simple and computationally cheap. This ensures the quality assurance of the procedure when the simulation code's implementation is changed.

An alternative to the described simple cases is given by model- and full-scale experiments of ship induced scouring, as published e.g. by Schmidt [90], Geisenhainer and Aberle [26], and Felkel and Steinweller [24]. Such experiments feature complex three

dimensional flow topologies and long time scales. Both reduce their applicability as benchmark cases to address the performance of individual features and models, especially long time-scales make SPH simulations very challenging. Due to these disadvantages, the present work does not consider respective experiments for validation studies.

Simulation results of all investigated validation and verification cases indicate a very good agreement with reference data, both for single and multi-phase problems. Therefore, the method is considered to deliver reliable answers within its scope of applications.

Observed disadvantages of the applied numerics are related to a noisy pressure field prediction, which could be expected due to the applied WCSPH approach. Still, an improvement in accuracy and a reduction of noise within the pressure field should be the subject to future work. Studies related to discretisation dependencies reveal a minor influence of the particle resolution on the overall quality of results. Nevertheless, such studies could be extended, especially for the suspension treatment where a certain amount of particles is required to resolve the suspension layer.

9 Applications

The chapter presents two full-scale harbour hydrodynamics applications. The first example is concerned with the scouring close to a quay wall induced by a transverse thruster. The respective vessel geometry refers to an analytically described Wigley hull. The scenario is investigated in 2D and a simplified 3D set-up. Predictive differences between the two computational models are outlined. The second application deals with harbour bed erosions induced by a starting ship propeller. For this scenario, a complete 3D discretisation of the KRISO container ship is used.

In addition to the habour hydrodynamics examples, two alternative applications from the field of offshore engineering are briefly presented to demonstrate the code's applicability to complex marine engineering problems.

9.1 Transverse thruster induced scouring

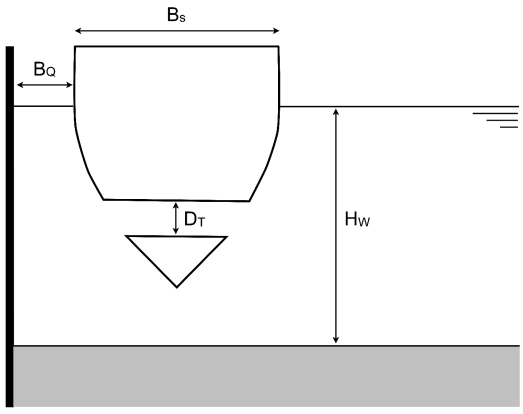

Figure 9.1: Sketch of the Wigley-ship bow section frame.

The first application is devoted to the formation of a scour induced by a transverse thruster. As illustrated in Fig. 9.1, a 2D ship frame that is located at the distance of $B_Q = 5$ m away

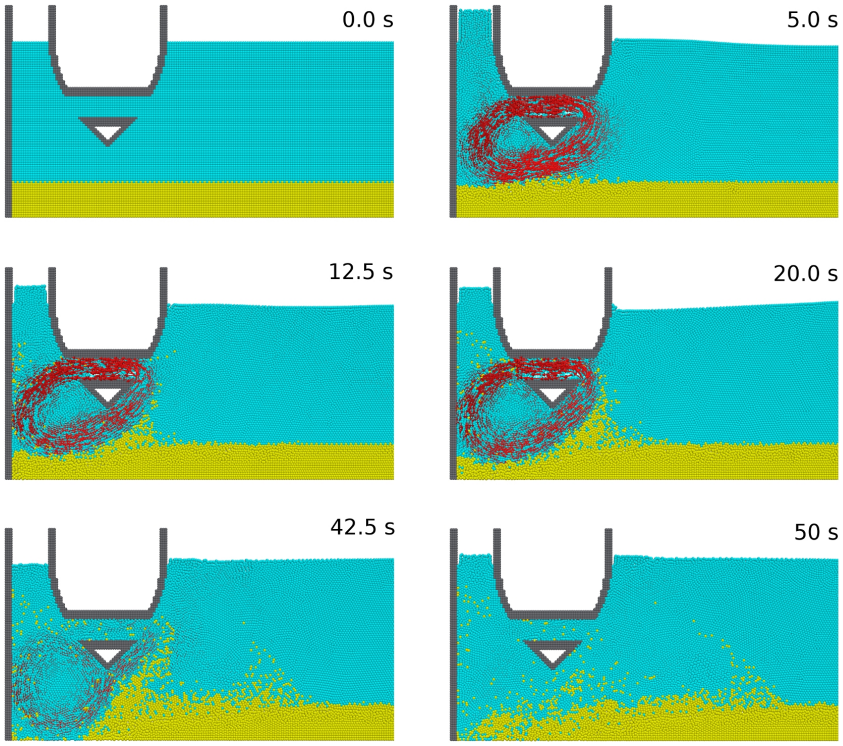

Figure 9.2: 2D simulation of thruster induced soil erosion. The fluid velocity is indicated by red vector arrows.

from a quay wall is considered. The frame is taken from a Wigley hull at its longitudinal coordinate $x = 140$ m. The hull shape is analytically described by

$$\frac{y}{2B_S} = \frac{x}{L_S}\left(1 - \frac{x}{L_S}\right)\left[1 - \left(\frac{z}{T_S}\right)^2\right] , \tag{9.1}$$

with the ship length $L_S = 180$ m, width $B_S = 18$ m and draught $T_S = 11.25$ m. The transverse and vertical coordinates are denoted by y and z, respectively. The water depth of the basin is set to $H_W = 15$ m. The ship hosts a transverse thruster with a diameter of $D_T = 2.5$ m and a power of 1800 kW. The thruster is located with its centre at 7 m below the free surface. A threshold viscosity of $\mu_{max} = 1500$ Pa $\cdot$ s in conjunction with the combined solid/fluid model (cf. section 4.2.4) with $E = 8.5 \cdot 10^5$ Pa, $\nu = 0.3$, $\phi = 30°$, and $C = 0$ Pa are used to represent the harbour soil. The suspension model outlined in section 4.3 is applied to bridge between the fluid and the granular material. In the present example, the ship's motion is neglected. The complete model is discretised by a particle spacing of 0.25 m.

The body force model for transverse thrusters described in section 5.2.2 is applied to

mimic the flow within the thruster tunnel. In the 2D simulation, A_T is adopted from a corresponding 3D setting which yields a jet velocity of 9 m/s for the present case. To avoid initial disturbances, the jet velocity is linearly increased from 0 to 9 m/s in the first two seconds. The thruster is operated for a period of 40 s. Figure 9.2 displays the flow field and the induced soil erosion. It can be observed, that a large scour is formed close to the quay wall. The topography of the harbour bottom is strongly influenced by dynamic flow phenomena, e.g. the large vortex located between the ship frame, quay wall and bottom. Parts of the soil are sliding back into the scour after the thruster stopped. Still, as indicated by the last picture in Fig. 9.2 (50 s), a deep scour remains close to the wall. Furthermore, the backfill is composed of a water/soil mixture that does not provide the same bearing capacity as pure soil.

Main advantages of 2D simulations are related to a significant reduction of computational effort compared to 3D set-ups. 2D scouring simulations – like the present one – can easily be performed within the range of hours on multi-core workstation computers. Corresponding 3D simulations on the other hand consume several weeks of computational time for equivalent real-time periods on the same machine. Accordingly, one might tend towards using 2D set-ups in the industrial praxis. However, this might not generally be reliable.

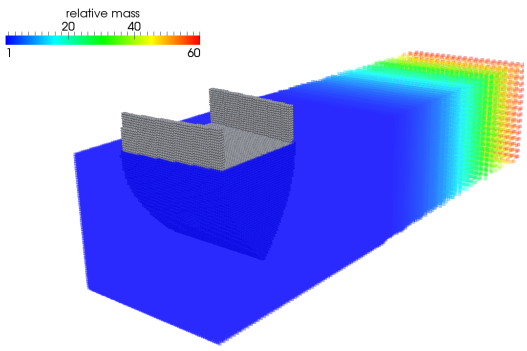

Figure 9.3: Wigley ship bow section embedded into 3D domain with variable particle resolution.

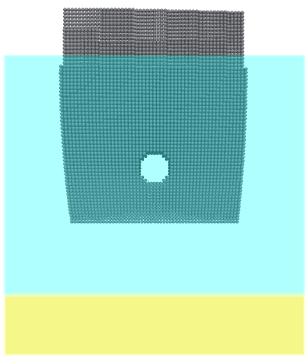

Figure 9.4: Side view of the 3D Wigley ship bow section.

In the following, the two-dimensional bow thruster is extended to a simplified three-dimensional ship section as illustrated in Figs. 9.3 and 9.4. A variable particle resolution with a maximum particle spacing of 0.97 m is used for the far field to keep the overall

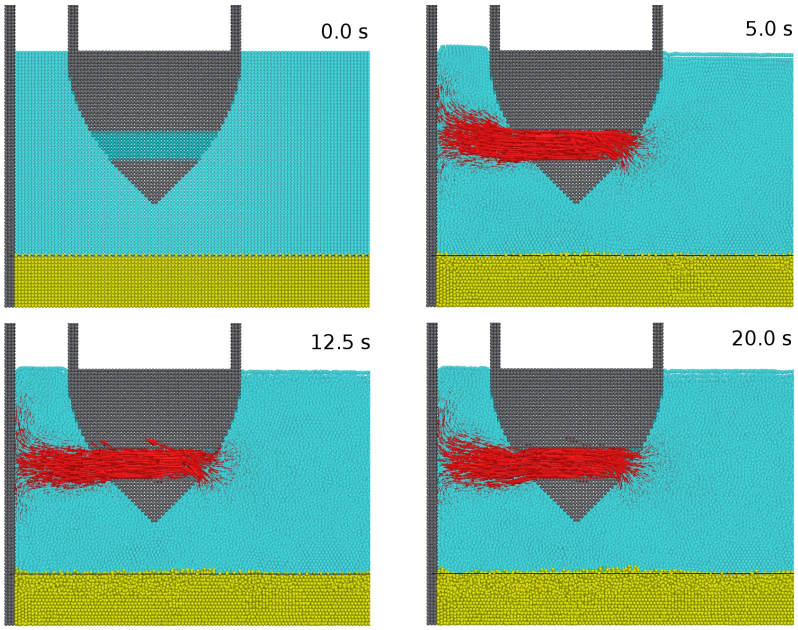

Figure 9.5: 3D simulation of thruster induced soil erosion. The fluid velocity is indicated by red vector arrows. The black line refers to the initial water/soil-interface.

number of particles as low as possible. All other features of the application are unchanged.

Figure 9.5 shows the flow topology and the bottom erosion at different instants. If compared to the 2D results presented in Fig. 9.2 significant differences both in the flow formation and the change of bottom topography can be observed. As soon as the jet impacts on the wall, it gets deflected not only up- and downwards like in the 2D simulation but also sideways. The propulsive power is therefore strongly diffused before the flow hits the basin bottom with fairly moderate speeds. There still is a tendency towards scouring close to the quay wall and some soil accumulation in front of the frame, but this is by far not as significant as it is predicted by the 2D set-up. The example illustrates that for the considered type of applications, 2D simulations lead to a strong over-prediction of erosion phenomena due to blockage effects.

9.2 Ship propeller induced erosion

The second application example studies the harbour bed erosion induced by the starting propeller of a large full-scale container vessel. The considered geometry refers to the well known KRISO container ship (KCS) [105] with a length between perpendiculars of 230 m

Figure 9.6: Particle discretisation of the KCS ship hull.

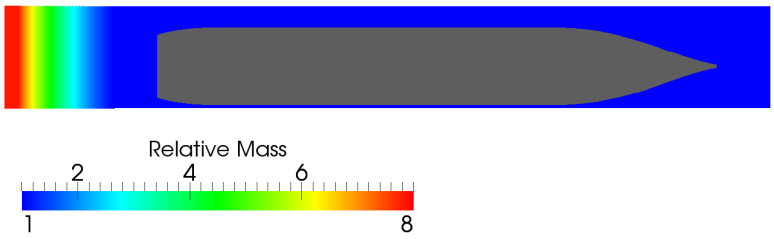

Figure 9.7: Vessel hull (grey) and domain particles. Colouring refers to the relative particle mass.

and 32.2 m width. Figure 9.6 displays the employed particle representation of the hull. Simulations are performed for an extreme loadcase with 12 m draught in a harbour basin providing 13.5 m water depth.

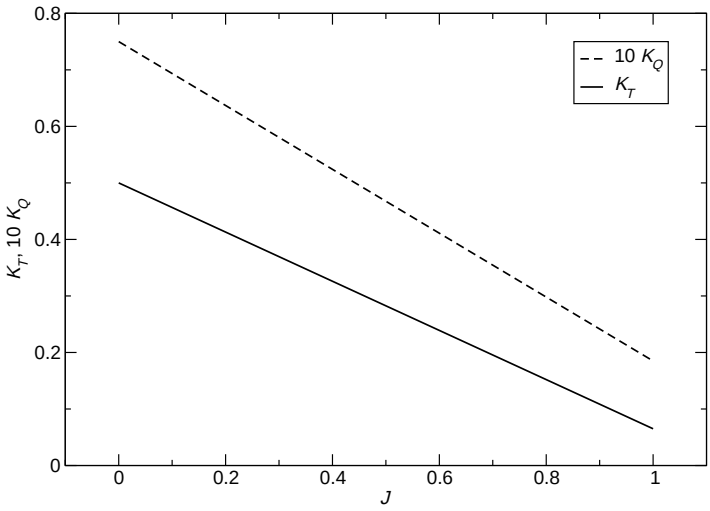

Figure 9.8: Linearized open water diagram for the KCS propeller.

The ship is modelled as a free-floating rigid body under the influence of thrust and hydrodynamic forces. The propeller features a diameter of 8 m and is modeled by an actuator disc according to section 5.2. A thickness of 8 particle rows starting from the end of the shaft bossing is utilized to represent the propeller influence. The propeller's open water characteristics refer to $c_{T1} = 0.5$, $c_{T2} = 0.435$, $c_{Q2} = 0.075$, $c_{Q2} = 0.0565$ (cf. Fig.

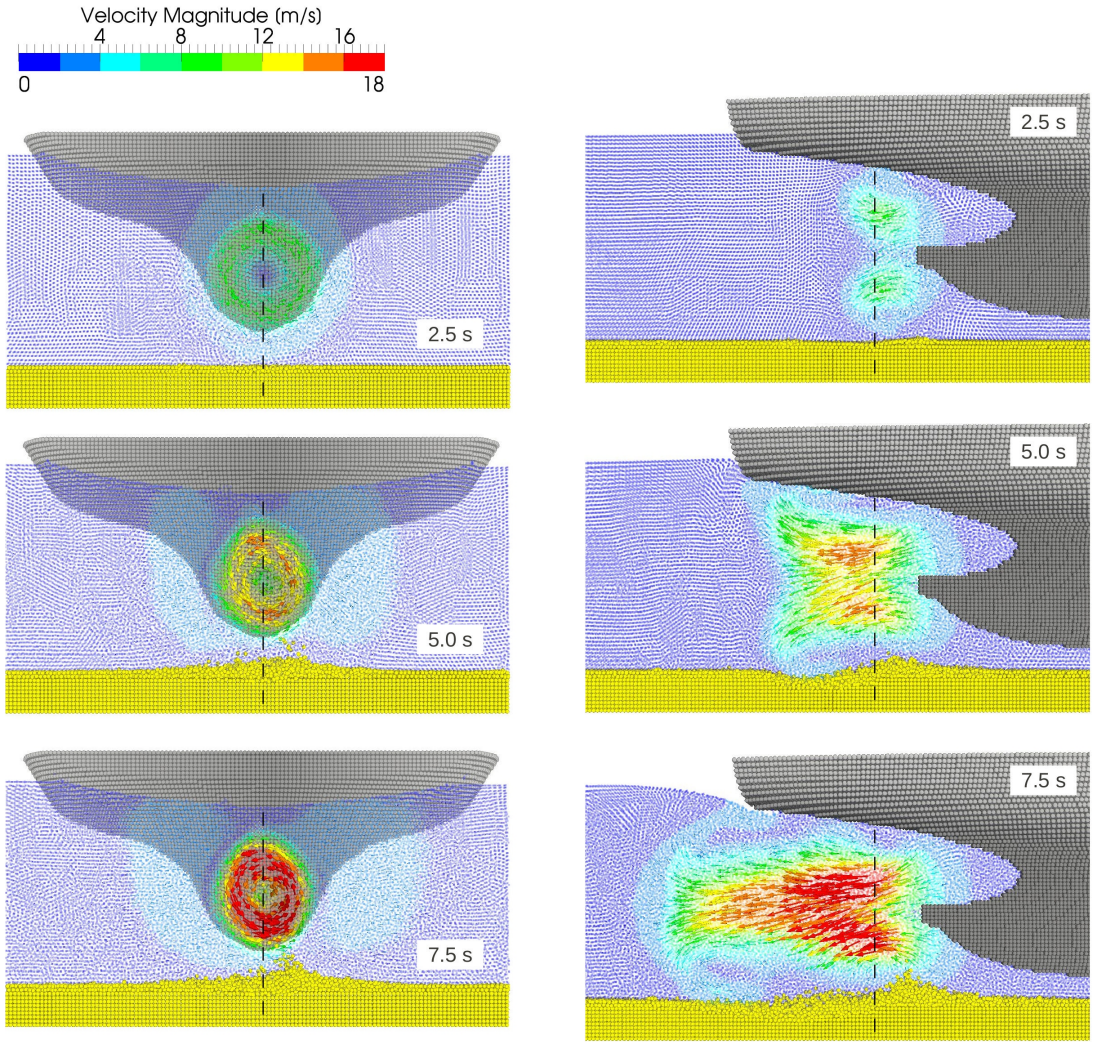

Figure 9.9: Flow topology behind the propeller disc. The pictures show longitudinal and cross-sectional cuts at different points in time. Water particles are coloured according to their velocities. The dashed black lines denote the location of the corresponding cuts in the other sectional plane.

9.8).

The hull and the surrounding water and soil are discretised by a particle spacing of 0.25 m. As displayed in Fig. 9.7, a variable resolution strategy is applied behind the ship.

On the starboard side, the ship is situated close to a fixed boundary representing a quay wall. The overall domain measures 320 x 43 x 18 m (length x width x depth) which leads to 14.3 Mio particles. Cohesionless soil with a density of 1500 kg/m^3, a friction angle of 30° and a threshold soil viscosity of 1000 Pa s is considered for the basin bottom. The soil is modelled as a non-Newtonian fluid according to section 4.2.3 in conjunction with the suspension model outlined in section 4.3. Soil particles exceeding the maximum viscosity

are frozen in space with zero velocity. For the present application, the fluid soil model is expected to deliver comparable results to the combined solid/fluid model as illustrated in the basic soil validation cases (section 8.2).

In order to model the starting phase, the revolution rate of the propeller is linearly increased from 0 to 2 s^{-1} within the first 5 s of the simulation. Due to the shallow water, erosion sets in almost immediately. As illustrated in Fig. 9.9, different erosional phenomena can be observed. In the figure, water particles are coloured according to their velocity magnitude. Vector arrows referring to the velocity indicate the flow topology. The dashed black lines denote the position of the longitudinal and the cross-sectional cuts, respectively.

As indicated by the cross-sectional cuts, the propeller induced circumferential fluid motion leads to an asymmetric soil dislocation. The enhanced erosion in longitudinal direction and elutriated soil particles are caused by vortex driven strong flow reversal in the vicinity of the bottom. Due to the propeller surge, parts of the suspension are transported into (and through) the propeller disc. Additionally, soil accumulates in front of the propeller.

9.3 Alternative applications

This section shows two illustrative examples of GADGET-$^{H}2^{O}$ being applied to complex offshore engineering processes. It clarifies that the procedure is not tailored to port hydrodynamics but can be used in the context of a great variety of marine engineering problems.

Jacket launching

The first alternative application relates to a shallow water jacket structure of 30 m length being launched in 40 m deep water from a 60 m long barge. The barge measures a width of 17 m, a moulded depth of 5 m and displaces 2083 t at 2.25 m initial draught. Completely submerged, the modelled jacket displaces 680 t. To finally receive an equilibrium floating condition with approximately 3/4 of the jacket's volume being submerged, it's weight is set to 500 t with a center of gravity located in its geometric balance point. Thus, an equilibrium floating condition yields an initial weight of the barge of 1583 t. To initialise the launching process, the barge's longitudinal center of gravity is shifted 7 m towards the stern and the weight is increased to 2000 t. Note that this strategy resembles the real

process. Fig. 9.10 depicts a time series of situations from the impact to the jacket's final floating condition. Fig. 9.11 illustrates the flow around the jacket tubes during the impact at 9.2 s.

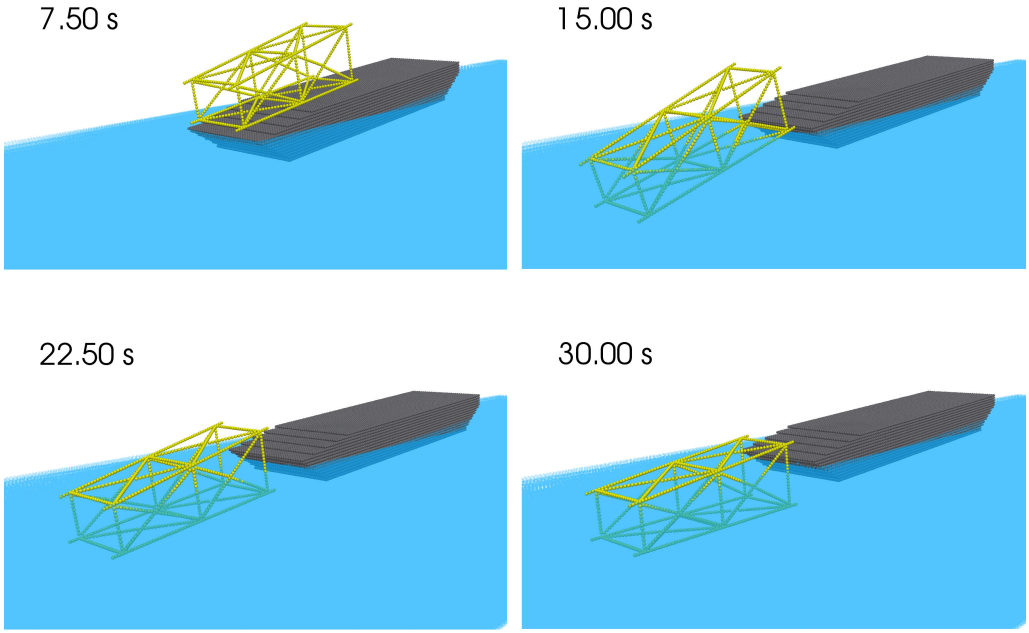

Figure 9.10: Side-view of jacket and barge at different points in time.

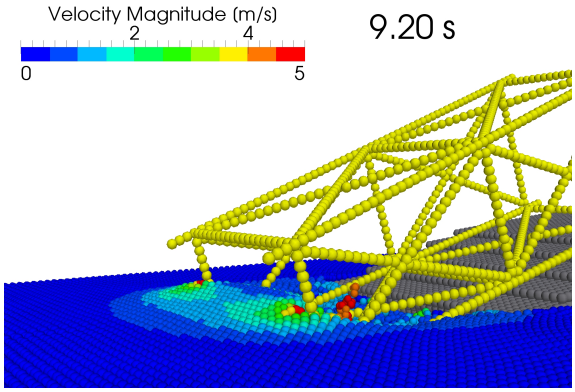

Figure 9.11: Detail of the jacket at t=9.2 s after the initialisation of the launching. Water particles are coloured according to their velocity magnitude.

Foundation installation

The second example displays the simulation of the installation of a foundation for wind turbines. Erosions of the seabed, flooding of the structure and the foundation's rate of decent are analysed. The considered type of gravity foundation is usually applied in water depths of approximately 30-50 m. The structure is thought to be towed to the location and subsequently lowered to the ground by partial flooding. The present example shows a simplified 2D simulation of the installation process of an axisymmetric foundation which measures 30 m in diameter. Fig. 9.12 shows the evolution of the foundation's vertical velocity as well as the flooding process at different points in time. The last picture in Fig. 9.12 illustrates the erosional mechanism just before the structure touches the seabed.

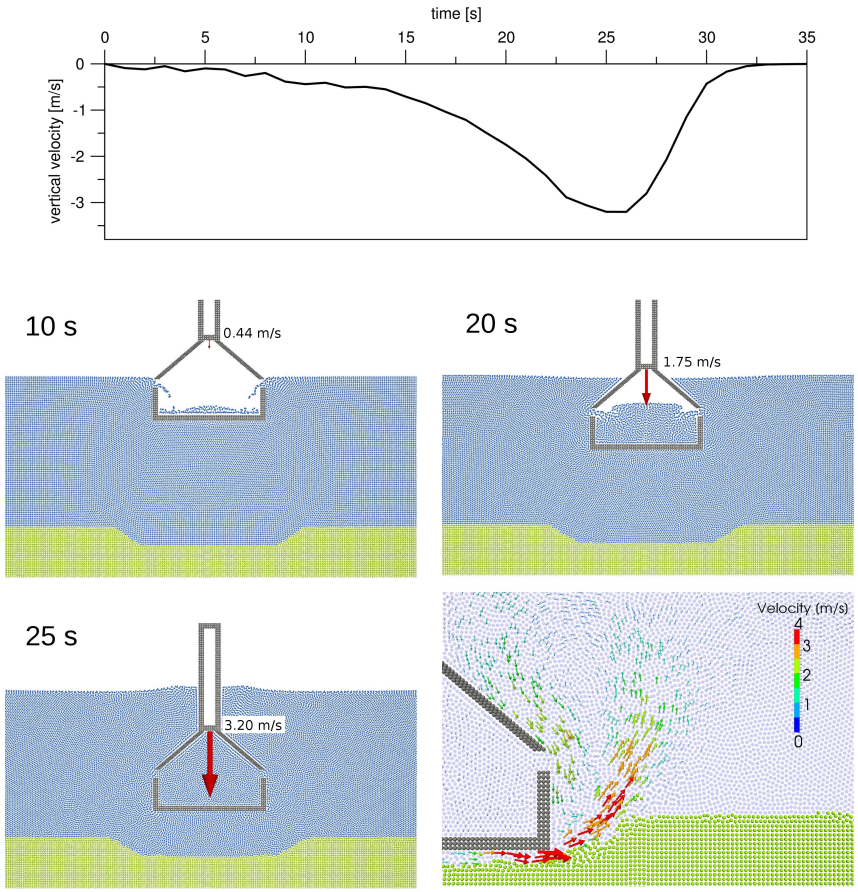

Figure 9.12: Plot of the foundation's vertical velocity and time series of the flooding process. The lower right picture illustrates the erosional mechanism when the foundation approaches the ground.

9.4 Discussion of results

The application examples demonstrate the procedure's applicability to full-scale port hydrodynamic problems. They show that it is possible to run simulations with several millions of particles in conjunction with complex and realistic ship geometries that involve interactions between ship, propulsor, water, soil and quay facilities. The present code is therefore not limited to academic small-scale examples but may be used for the investigation of industrially relevant scenarios. The comparison between a 2D and a corresponding 3D simulation of a thruster induced scouring reveals that this problem should be simulated in 3D, as erosion phenomena are misrepresented due to an unphysical blocking effect in 2D. The alternative applications show that the procedure can successfully be used for the simulation of further marine problems.

Limitations of the method are related to the feasible simulation time together with fine particle resolutions. The latter demands rather small time-step sizes and obviously leads to an increased number of particles. Both results in an increased time to solution for rather short real time periods even if the code is running on cluster machines with an acceptable parallel performance. At the present stage, long term simulations in the range of several minutes or even hours can hardly be performed. Unfortunately, the prediction of ship induced erosion processes often involves such long term simulations. Such limitations reveal the need for an increased computational efficiency which might be achieved by General Purpose Computation on Graphics Processing Unit (GPGPU) implementations.

10 Summary and Perspectives

The thesis reports on the development and application of a Smoothed-Particle-Hydrodynamics procedure to study harbour hydrodynamic problems focusing on ship induced scours. State of the art simulation methods for erosional processes commonly solve the dynamics of the water phase and account for sediment transportation by semi-empirical relationships between the bottom shear stress and soil properties. Contrary to this, an SPH based monolithic approach is pursued in the present work. Accordingly, models for viscous fluids and soil – linked by a water/soil-suspension treatment – have been derived and implemented. Additionally, an 6DOF motion solver in conjunction with a propeller model has been introduced to simulate free floating, self propelled ships. The method has been supplemented by a variable resolution scheme to reduce the overall number of particles when applied to full scale simulations with large computational domains.

Concerning the physical modelling, both, the water and soil phase are treated by a weakly compressible SPH model using Tait's equation for pressure evaluations. Water is modelled as a Newtonian fluid with a constant molecular viscosity. An additional turbulent viscosity obtained from a Smagorinsky LES model accounts for turbulent effects. The soil is modelled by a combined solid/fluid approach which is based on the Mohr-Coulomb yield criterion. Small relative motions within the material are captured by a linear-elastic relationship while the soil is treated as a non-Newtonian fluid if large shear rates occur. A blending function provides a smooth transition between the two model branches. To account for partly saturated porous media, the model features a variable cohesion which is computed in dependency of the local soil saturation. The corresponding pore water flow follows an Eulerian approach based on Darcy's diffusion equation. Phases interfaces and mixtures between water and soil are captured by a concentration based water/soil-suspension model. An apparent variable viscosity is derived from a Chézy-relation between the shear stresses and the local flow velocity. Ships are included into

the SPH framework as free floating rigid bodies that are discretised by body particles with a fixed alignment to the vessel geometry. Their positions and velocities are evaluated by an external 6DOF motion solver based on a quaternion formulation without gimbal lock. Propulsion devices are not geometrically resolved but represented by an actuator disc body force approach. Corresponding propulsion thrusts are added to the body particles which allows for the simulation of self propelled ship motions. Variable particle resolutions follow a changeable mass philosophy, where particle masses and kernel properties are manipulated according to the current position with respect to predefined Eulerian subregions. The classical conservation equations are supplemented by source terms ensuring the conservation of density and momentum in conjunction with a dynamic particle mass. Spatial variations of the kernel length are included into the evaluation of the kernel-function gradient.

Using a weakly compressible SPH framework, major numerical challenges are related to an accurate prediction of pressure fields. In the present work, different strategies have been derived and applied to overcome such drawbacks. Instabilities arising from discontinuous density gradients at the water/soil interface are avoided by a concentration based density blending approach. This treatment provides a smooth transition of particle masses, density and pressure. In order to start the simulation from balanced initial conditions, particle densities and pressures are initialised according to their vertical position and the corresponding hydrostatic pressure. Initial transients can additionally be eliminated by a short-time damping of the particle velocities. Throughout the simulations, an additional XSPH-type smoothing is applied to the velocity and pressure field. An invariant smoothing factor is determined from the kernel length, speed of sound and time step size.

The procedure has been verified and validated against analytical, numerical and experimental reference solutions for various single-phase and multi-phase test-cases. Generally, a satisfactory agreement was obtained for all investigated examples. It was shown that the code is capable of predicting single phase water and soil behaviour, water/soil-suspension flows, partly saturated soils, multi-phase-hydrostatics and floating body motions with encouraging accuracies. Minor weaknesses related to the evaluation of pressure fields became obvious which was expected for weakly compressible SPH. Still, it was demonstrated that the noise within the pressure field can significantly be reduced by applying a smoothing scheme without compromising the overall accuracy. Validation cases related to the

variable resolution approach illustrated its efficiency and advantages over more complex splitting and merging algorithms. Viz., the investigated examples indicated a linear relation between the computational time and the applied number of particles.

Application examples focused on full scale ship manoeuvres. A simple Wigley hull bow geometry in conjunction with the transverse thruster model illustrated the scouring close to a quay wall by a deflected thruster jet. The case has been simulated both with a 2D and a simplified 3D set-up. A comparison between the results has shown that a 2D approach is not suitable for this kind of applications as it strongly over-predicts the erosion compared to 3D. The second example referred to the erosion of the harbour bed induced by a starting ship propeller. A complete 3D discretisation of the KRISO container ship geometry has been used in this case together with the body force propeller model. The two application cases demonstrated that the present code can be applied to full scale multi-physics harbour hydrodynamic problems. Two additional full-scale examples from the field of offshore engineering showed that the procedure's range of applications is not limited to ports. However, the presented cases also revealed the huge computational effort associated to 3D engineering simulations which reduces the method's attractiveness for industrial applications.

Future work should therefore – amongst others – be related to an increase of computational performance. Since the present procedure already provides an efficient parallel CPU performance, the strongest benefits are expected from adequate GPGPU implementations. Furthermore, the variable resolution scheme should be tested in more complex multi-dimensional variable resolutions. The latter requires an automatic particle initialisation, which is a challenge itself [9, 61]. Concerning numerical accuracy, an improvement of boundary conditions especially for partly wetted domains and an advanced pressure correction would be desirable. In the field of physical modelling, the influence of different erosion criteria needs to be investigated. The application of semi-empirical shear stress thresholds at the water/soil interface, obtained e.g. from Shield's curve, might be beneficial in conjunction with the suspension model. As the typical particle resolution for full scale applications is rather coarse, the prediction of turbulent stresses by the current LES model is expected to be inaccurate. This problem could be overcome by implementing an alternative RANS based turbulence model.

The thesis demonstrates that the developed numerical SPH-based procedure is suitable

for the simulation of multi-physic harbour hydrodynamic problems. SPH provides strong advantages over alternative mesh based methods related to large relative motions, multiple phases and continua, free surface flows and (several) floating bodies. Such phenomena are not only relevant to the primarily addressed field of port construction but occur in very similar characteristics in many other offshore and hydraulic engineering disciplines. The present procedure therefore provides the potential of being extensively used and to play an important role in a wide range of applications.

Bibliography

[1] S. Adami, X. Hu, and N. Adams. A generalized wall boundary condition for smoothed particle hydrodynamics. *Journal of Computational Physics*, 231:7057–7075, 2012.

[2] R. A. Bagnold. Experiments on a gravity-free dispersion of large solid spheres in Newtonian fluid under shear. *Proc. Royal Soc. Lond. A*, 255:49–63, 1954.

[3] J. Barnes and P. Hut. A hierarchical O(N log N) force-calculation algorithm. *Nature*, 324:446–449, 1986.

[4] G. K. Batchelor. *An Introduction to Fluid Dynamics*. Cambridge University Press, 1967.

[5] T. Belytschko, Y. Krongauz, D. Organ, M. Fleming, and P. Krysl. Meshless methods: An overview and recent developments. *Computer Methods in Applied Mechanics and Engineering*, 139(1 - 4):3 – 47, 1996.

[6] H. Bergh and N. Magnusson. Propeller Erosion and Protection Methods used in Ferry Terminals in the Port of Stockholm. *PIANC Bulletin No. 58*, pages 112–120, 1987.

[7] H.G. Blaauw and E.J. van de Kaa. Erosion of bottom and sloping banks caused by the screw race of manoeuvring ships. publication no. 202, Delft hydraulics laboratory, 1978.

[8] H. Borchers, H. Hausen, K.-H. Hellwege, Kl. Schäfer, and E. Schmidt, editors. *Landolt-Börnstein Zahlenwerte und Funktionen aus Physik, Chemie, Astronomie, Geophysik und Technik*. Springer, 1971.

[9] B. Bouscasse, M. Antuono, S. Marrone, and A. Colagrossi. Particle initialization through a novel packing algorithm. In *6th Int. Spheric Workshop*, pages 109– 116, 2011.

[10] J. Brix, editor. *Manoeuvring Technical Manual*. Seehafen-Verlag, 1993.

[11] H. H. Bui and R. Fukagawa. An improved method for saturated soils and its application to investigate the mechanisms of embankment failure: Case of hydrostatic pore-water pressure. *Int. J. Numer. Anal. Meth. Geomech.*, 37(1):37, 50 2013.

[12] H. H. Bui, R. Fukagawa, and K. Sako. A Study of the Matter of SPH Application to Saturated Soil Problems. In *Proceedings of the 5th international SPHERIC workshop*, pages 354–361, 2010.

[13] H. H. Bui, R. Fukagawa, K. Sako, and S. Ohno. Lagrangian meshfree particles method (SPH) for large deformation and failure flows of geomaterial using elastic-platic soil constitutive model. *Int. J. Numer. Anal. Meth. Geomech.*, 32:1537–1570, 2008.

[14] H. H. Bui, C. T. Nguyen, K. Sako, and R. Fukagawa. A SPH model for seepage flow through deformable porous media. In *6th Int. SPHERIC workshop*, pages 164–171, 2011.

[15] A. Chaniotis. *Remeshed Smoothed Particle Hydrodynamics for the Simulation of Compressible, Viscous, Heat Conducting, Reacting and Interfacial Flows*. PhD thesis, Swiss Federal Institute of Technology Zurich, 2002.

[16] C. O. Chin, Y. M. Chiew, S. Y. Lim, and F. H. Lim. Jet Scour around Vertical Pile. *Journal of Waterway, Port, Coastal, and Ocean Engineering*, 122(2):59–67, 1996.

[17] P. Chossat and G. Iooss. *The Couette-Taylor Problem*. Springer, 1994.

[18] V. T. Chow. *Open-Channel Hydraulics*. McGraw-Hill, 1959.

[19] A. Colagrossi, M. Antuono, and D. Le Touzé. Theoretical considerations on the free-surface role in the smoothed-particle-hydrodynamics model. *Physical Review E*, 79, 2009.

[20] R. H. Cole. *Underwater Explosions*. Princeton University Press, 1948.

[21] S. Cummins and M. Rudman. An sph projection method. *Journal of Computational Physics*, 152(2):584 – 607, 1999.

[22] J. Dubinski. A Parallel Tree Code. *New Astronomy*, 1:133–147, 1996.

[23] J. Feldman. *Dynamic refinement and boundary contact forces in Smoothed Particle Hydrodynamics with applications in fluid flow problems*. PhD thesis, University of Wales Swansea, 2006.

[24] K. Felkel and H. Steinweller. Natur- und Modellversuche über die Wirkung der Schiffe auf Flußsohlen aus Grobkies. *Wasserwirtschaft*, 62(8):243–249, 1972.

[25] L. Fraccarollo and H. Capart. Riemann wave description of erosional dam-break flows. *Journal of Fluid Mechanics*, 461:183–228, 2002.

[26] P. Geisenhainer and J. Aberle. Scale Model Study of Propeller Induced Scour Development. In *Experimental and Computational Solutions of Hydraulic Problems - 32th International School of Hydraulics*, pages 119–131. Springer, 2013.

[27] R. A. Gingold and J. J. Monaghan. Smoothed particle hydrodynamics: theory and application to non-spherical stars. *Monthly Notices of the Royal Astronomical Society*, 181:375–389, 1977.

[28] H. Goldstein. *Klassische Mechanik*. AULA-Verlag Wiesbaden, 1989.

[29] H. Gotoh, S. Shao, and T. Memita. SPH-LES Model for Wave Dissipation using a Curtain Wall. *Annual Journal of Hydraulic Engineering*, 47:397–402, 2003.

[30] N. Grenier, M. Antuono, A. Colagrossi, D. Le Touzé, and B. Alessandrini. An Hamiltonian interface SPH formulation for multi-fluid and free surface flows. *Journal of Computational Physics*, 228:8380–8393, 2009.

[31] G. Gudehus. *Physical Soil Mechanics*. Springer, 2011.

[32] G. A. Hamill. The Scouring Action of the Propeller Jet Produced by a Slowly Manoeuvring Ship. *PIANC Bulletin No. 62*, 1988.

[33] G. A. Hamill, H. T. Johnston, and D. P. Stewart. Propeller Wash Scour near Quay Walls. *Journal of Waterway, Port, Coastal, and Ocean Engineering*, 125(4):170–175, 1999.

[34] X. Hu and N. Adams. An incompressible multi-phase sph method. *Journal of Computational Physics*, 227(1):264 – 278, 2007.

[35] X. Hu and N. Adams. A SPH model for incompressible turbulence. *eprint arXiv:1204.5097*, 2012.

[36] ISL. Shipping Statistics and Market Review. Statistical Publication, Institute of Shipping Economincs and Logistics (ISL), Bremen, 2011.

[37] J. T. Jenkins and S. B. Savage. A theory for rapid flow of identical, smooth, nearly elastic particles. *J. Fluid Mech.*, 130:187–202, 1983.

[38] P. Jop, Y. Forterre, and O. Pouliquen. A constitutive law for dense granular flows. *Nature*, 441:727–730, 2006.

[39] N. Koliha. *Entwicklung eines 6DOF-Moduls auf der Basis von Quaternionen zur Simulation freier Bewegungen schwimmender Körper*. Bachelor thesis, Technische Universität Hamburg-Harburg, 2011.

[40] M. Kraskowski. Simulating Hull Dynamics in Waves using a RANSE Code. *Ship Technology Research - Schiffstechnik*, 57(2):120–127, 2010.

[41] J. Kröger, A. Stück, and T. Rung. Adjoint Aftship Re-design for Wake Optimization under the Influence of Active Propulsion. In *4th Int. Conference on Comp. Methods in Marine Engineering - MARINE 2011*, 2011.

[42] K. Krüger-Kopiske. *Deutsche Containerschiffe*. Koehlers Verlagsgesellschaft, 2004.

[43] A.C.H. Kruisbrink, F.R. Pearce, T. Yue, K.A. Cliffe, and H.P. Morvan. Sph multi-fluid model with interface stabilization based on a quasi-buoyancy correction. In *Proc. of the 7th International SPHERIC Workshop, Prato*, 2012.

[44] E.-S. Lee, C. Moulinec, R. Xu, D. Violeau, D. Laurence, and P. Stansby. Comparisons of weakly compressible and truly incompressible algorithms for the sph mesh free particle method. *Journal of Computational Physics*, 227(18):8417 – 8436, 2008.

[45] T. Lenaerts. *Unified Particle Simulations and Interactions in Computer Animation*. PhD thesis, Katholieke Universiteit Leuven, 2009.

[46] C. Leppert. *Mehrphasenmodell für granulare Medien zur numerischen Untersuchung des Phasenübergangs bei der Entleerung von Silos*. PhD thesis, Technische Universität Carolo-Wilhelmina zu Braunschweig, 2007.

[47] S. J. Lind, R. Xu, P. K. Stansby, and B. D. Rogers. A Stabilising Diffusion-Based Shifting Algorithm for Incompressible Smoothed Particle Hydrodynamics. In *Proceedings of the 6th international SPHERIC workshop*, pages 14–21, 2011.

[48] G. R. Liu. *Meshfree Methods: Moving Beyond the Finite Element Method*. CRC Press, 2009.

[49] G.R. Liu and M.B. Liu. *Smoothed Particle Hydrodynamics - a meshfree particle method*. World Scientific Publishing Co. Pte. Ltd., Singapore, 2003.

[50] J.-P. Longe, P. Hebert, and R. Byl. Problèmes d' érosion aux ouvrages de quai existants causes par les propulseur d' etrave et les helices principales des navier lors de leurs accostages ou appareillages. *PIANC Bulletin No. 58*, pages 16–44, 1987.

[51] L. B. Lucy. A numerical approach to the testing of the fission hypothesis. *Astronomical Journal*, 82:1013–1024, 1977.

[52] J. R. MacDonald. Some Simple Isothermal Equations of State. *Rev. Mod. Phys.*, 38:669–679, 1966.

[53] F. Macià, A. Souto-Iglesias, M. Antuono, and A. Colagrossi. Benefits of using a Wendland kernel for free-surface flows. In *Proceedings of the 6th international SPHERIC workshop*, pages 30–37, 2011.

[54] S. Manenti, A. Di Monaco, M. Gallati, S. Sibilla, G. Agate, R. Guandalini, and A. Maffio. Simulating rapid sediment scour by water flow with SPH. In *Proc. of the 4th International SPHERIC Workshop, Nantes*, 2009.

[55] S. Manenti, S. Sibilla, M. Gallati, G. Agate, and R. Guandalini. SPH Simulation of Sediment Flushing Induced by a Rapid Water Flow. *Journal of Hydraulic Engineering*, 138(3):272–284, 2012.

[56] M. Manzke, K. Wöckner, J. Schoop-Zipfel, T. Rung, and M. Abdel-Maksoud. Efficient Viscous Simulation Approaches to Manoeuvering in Seaways. In *North Atlantic Treaty Organisation, Research and Technology Organisation, AVT- Specialists' Meeting on Assessment of Stability and Control Prediction Methods for Air and Sea Vehicles, Portsdown, United Kingdom*, 2011.

[57] S. Marrone, M. Antuono, A. Colagrossi, G. Colicchio, D. Le Touzé, and G. Graziani. δ-SPH model for simulating violent impact flows. *Computer Methods in Applied Mechanics and Engineering*, 200:1526–1542, 2011.

[58] S. Marrone, A. Colagrossi, M. Antuono, C. Lugni, and M.P. Tulin. A 2d+t sph model to study the breaking wave pattern generated by fast ships. *Journal of Fluids and Structures*, 27(8):1199–1215, 2011.

[59] A. Marsh, G. Oger, D. Le Touzé, and D. Guibert. Validation of a conservative variable-resolution SPH scheme including ∇h terms. In *Proceedings of the 6th international SPHERIC workshop*, pages 86–92, 2011.

[60] J. C. Martin and W. J. Moyce. Part IV. An Experimental Study of the Collapse of Liquid Columns on a Rigid Horizontal Plane. *Philosophical Transactions of the Royal Society of London. Series A, Mathematical and Physical Sciences*, 244:312–324, 1952.

[61] A. Mayrhofer, M. Gomez-Gesteira, A. Crespo, and B. Rogers. Advanced Pre-Processing for SPHysics. In *5th Int. SPHERIC Workshop*, pages 201–208, 2010.

[62] H. Meier-Peter and F. Bernhardt, editors. *Handbuch Schiffsbetriebstechnik*. Seehafen Verlag, 2006.

[63] C. Miller and H. P. Dücker. Vorlesung: Geotechnik im Strom- und Hafenbau, 7. Kolkbildung an Uferbauwerken. lecture notes, Hamburg University of Technology, Institute for Geotechnical Engineering and Construction Management.

[64] J. J. Monaghan. Smoothed particle hydrodynamics. *Annu. Rev. Astron. Astrophys.*, 30:543–574, 1992.

[65] J. J. Monaghan. Simulating Free Surface Flows with SPH. *Journal of Computational Physics*, 110:399–406, 1994.

[66] J. J. Monaghan. Smoothed Particle Hydrodynamics and Its Diverse Applications. *Annual Review of Fluid Mechanics*, 44:323–346, 2012.

[67] J. J. Monaghan and J. B. Kajtar. SPH Boundary Forces. In *Proceedings of the 4th international SPHERIC workshop*, pages 217–220, 2009.

[68] J. J. Monaghan and J. C Lattanzio. A refined particle method for astrophysical problems. *Astronomy and Astrophysics*, 149(1):135–143, 1985.

[69] J. Morris, P. Fox, and Y. Zhu. Modeling low reynolds number incompressible flows using sph. *Journal of Computational Physics*, 136(1):214 – 226, 1997.

[70] C. Moulinec, R. Issa, J. C. Marongiu, and D. Violeau. Parallel 3-d sph simulations. *Comput. Model. Eng. Sciences*, 25(3):133–148, 2008.

[71] L. Müller and J.-O. Probst. Containerschiffwachstum ohne Ende. In J. Grabe, editor, *Seehäfen für Containerschiffe zukünftiger Generationen*, pages 1–16, 2008.

[72] United Nations. Review of Maritime Transport 2011. Technical report, United Nations Conference on Trade and Development, 2011.

[73] P. E. Nikravesh. *Computer-Aided Analysis of Mechanical Systems*. Prentice-Hall, Englewood Cliffs, New Jersey, 1988.

[74] F. N. Nnadi and K. C. Wilson. Motion of Contact-Load Particles at High Shear Stress. *J. Hydraul. Eng.*, 118:1670–1684, 1992.

[75] G. Oger, M. Doring, B. Alessandrini, and P. Ferrant. Two-dimensional SPH simulations of wedge water entries. *Journal of Computational Physics*, 213:803–822, 2006.

[76] P. Omidvar, P. Stansby, and B. Rogers. Wave body interaction in 2d using smoothed particle hydrodynamics (sph) with variable particle mass. *International Journal for Numerical Methods in Fluids*, 68(6):686–705, 2012.

[77] J. Owen. SPH modelling of Material Damage and Failure. In *5th Int. SPHERIC Workshop*, pages 297–304, 2010.

[78] A. Papanicolaou, M. Elhakeem, G. Krallis, M. Prakash, and J. Edinger. Sediment Transport Modeling Review - Current and Future Developments. *Journal of Hydraulic Engineering*, 134(1):1–14, 2008.

[79] M. Pastor, B. Haddad, G. Sorbino, S. Cuome, and V. Drempetic. A depth-integrated, coupled SPH model for flow-like landslides and related phenomena. *Int. J. Numer. and Anal. Meth. in Geomech.*, 33:143–172, 2009.

[80] S. Perez and W. Caliendo. Calculating Marine Propeller Scour Using SSIIM CFD Software. *Journal of Marine Environmental Engineering*, 9:75–84, 2008.

[81] PIANC. P.I.A.N.C. - A.I.P.C.N. - Bulletin 1987 No. 58.

[82] L.-C. Qiu. Two-Dimensional SPH simulations of landslide-generated water waves. *J. Hydraulic Engineering*, 134:668–671, 2008.

[83] M. Quecedo, M. Pastor, and M. I. Herreros. Numerical modelling of impulse wave generated by fast landslides. *Int. J. Numer. Meth. Engng*, 59:1633–1656, 2004.

[84] R. Qurrain. *Influence of the sea bed geometry and berth geometry on the hydrodynamics of the wash from a ship's propeller*. PhD thesis, Queens University of Belfast, 1994.

[85] N. Rajaratnam. Erosion by Plane Turbulent Jets. *Journal of Hydraulic Research*, 19(4):339–358, 1981.

[86] T. Rung and C. Ulrich, editors. *6th Int. Spheric Workshop*. Schriftenreihe Schiffbau, 2011.

[87] D. Ryan and G. Hamill. Determining propeller erosion at the stern of a berthing ship. *Journal of Waterway, Port, Coastal, and Ocean Engineering, 10.1061/(ASCE)WW.1943-5460.0000151*, 2012.

[88] J. Sauer. *Instationär kavitierende Strömungen : ein neues Modell, basierend auf Front Capturing (VoF) und Blasendynamik*. PhD thesis, Universität Karlsruhe, 2000.

[89] H. Schade and E. Kunz. *Strömungslehre*. de Gruyter, Berlin, New York, 1989.

[90] E. Schmidt. *Ausbreitungsverhalten und Erosionswirkung eines Bugpropellerstrahls vor einer Kaiwand*. PhD thesis, TU Braunschweig, 1998.

[91] S. Shao and E. Lo. Incompressible sph method for simulating newtonian and non-newtonian flows with a free surface. *Advances in Water Resources*, 26(7):787 – 800, 2003.

[92] D. Shepard. A two-dimensional interpolation function for irregularly spaced data. In *Proc. of 23rd A.C.M. Nat. Conf.*, 1968.

[93] J. Smagorinsky. General circulation experiments with the primitive equations. I. The basic experiment. *Monthly Weather Review*, 91(3):99–164, 1963.

[94] A. Souto-Iglesias, L. M. Gonzáles, A. Colagrossi, and M. Antuono. SPH no-slip BC implementation analysis at the continuous level. In *Proceedings of the 5th international SPHERIC workshop*, pages 29–36, 2010.

[95] V. Springel. The cosmological simulation code GADGET-2. *MNRAS*, 364:1105–1134, 2005.

[96] V. Springel, N. Yoshida, and S. D. M. White. Gadget: a code for collisionless and gasdynamical cosmological simulations. *New Astronomy*, 6(2):79 – 117, 2001.

[97] F. Stern, H. Kim, V. Patel, and H. Chen. A viscous-flow approach to the computation of propeller-hull interaction. *Journal of Ship Research*, 32(4):246–262, 1988.

[98] B. Sumer and J. Fredsøe. *The Mechnics of Scour in the Marine Environment*. World Scientific Publishing Co. Pte. Ltd., 2002.

[99] T. S. Ting and M. Prakash. Simulation of high Reynolds number flow over a backward facing step using SPH. Technical report, CSIRO Australia, Mathematical and Information Sciences, 2005.

[100] C. Ulrich. Weiterentwicklung und Anwendung eines massiv parallelen Smoothed-Particle-Hydrodynamics Simulationsverfahrens. Diploma Thesis, Institute for Fluid Dynamics and Ship Theory, Hamburg University of Technology, 2009.

[101] C. Ulrich and T. Rung. Massively-Parallel SPH-Simulations of Viscous Flows. In *Proceedings of the 4th SPHERIC Workshop, Nantes, France*, pages 399–406, 2009.

[102] C. Ulrich and T. Rung. SPH Modelling of Water/Soil-Suspension Flows. In *5th Int. SPHERIC Workshop*, pages 61–68, 2010.

[103] R. Vacondio, B. D. Rogers, P. K. Stansby, and P. Mignosa. SPH modeling of shallow flow with open boundaries for practical flood simulation. *J. Hydraulic Engineering*, 138:530–541, 2012.

[104] R. Vacondio, B. D. Rogers, P. K. Stansby, P. Mignosa, and J. Feldman. A dynamic particle coalescing and splitting scheme for SHP. In *Proceedings of the 6th international SPHERIC workshop*, pages 93–100, 2011.

[105] S.H. Van, W.J. Kim, G.T. Yim, D.H. Kim, , and C.J Lee. Experimental Investigation of the Flow Characteristics Around Practical Hull Forms. In *Proceedings 3rd Osaka Colloquium on Advanced CFD Applications to Ship Flow and Hull Form Design, Osaka, Japan*, 1998.

[106] L. Verlet. Computer "Experiments" on Classical Fluids. I. Thermodynamical Properties of Lennard-Jones Molecules. *Physical Review*, 159(1):98–103, 1967.

[107] R. Vignjevic, J. Campbell, J. Jaric, and S. Powell. Derivation of SPH equations in a moving referential coordinate system. *Computer Methods in Applied Mechanics and Engineering*, 198(30–32):2403 – 2411, 2009.

[108] D. Violeau. *Fluid Mechanics and the Sph Method: Theory and Applications*. Oxford Univ Press, 2012.

[109] D. Violeau and R. Issa. Numerical modelling of complex turbulent free-surface flows with the sph method: an overview. *International Journal for Numerical Methods in Fluids*, 53(2):277–304, 2007.

[110] R. von Mises. Mechanik der festen Körper im plastisch- deformablen Zustand. *Nachrichten von der Gesellschaft der Wissenschaften zu Göttingen, Mathematisch-Physikalische Klasse*, 1913:582–592, 1913.

[111] M. S. Warren and J. K. Salmon. A Parallel Hashed Oct-Tree N-Body Algorithm. *Proceedings of Supercomputing '93*, 1993.

[112] Y. Xing-Kaeding. *Unified Approach to Ship Seakeeping and Maneuvering by a RANSE Method*. PhD thesis, Technische Universität Hamburg-Harburg, 2006.

[113] R. Xu, P. Stansby, and D. Laurence. Accuracy and stability in incompressible SPH (ISPH) based on the projection method and a new approach. *Journal of Computational Physics*, 228:6703–6725, 2009.

[114] A. Yüksel, Y. Çelikoğlu, E. Çevik, and Y. Yüksel. Jet scour around vertical piles and pile groups. *Ocean Engineering*, 32:349–362, 2005.

[115] R. Zhao and O. Faltinsen. Water entry of two-dimensional bodies. *J. Fluid Mech.*, 246:593–612, 1993.